ABSTRACT

Title of Dissertation: NONLINEAR OPTICAL SEMICONDUCTOR MICRO-RING RESONATORS

Tarek A. Ibrahim, Doctor of Philosophy, 2003

Dissertation directed by: Professor Julius Goldhar
Department of Electrical and
Computer Engineering

In the last few years, there has been a great interest in all-optical switching devices due to the high demand on optical communication systems and networks. Unlike conventional electronic switches, photonic switching devices are ideal candidates for ultrafast data stream processing, approaching the THz regime. It is the goal of this thesis to propose, study, and demonstrate a new class of compact optical switches based on semiconductor microring resonators.

A detailed theoretical analysis of the nonlinear behavior of the microring resonator shows that, due to the resonance effect, there is an enhancement of the overall switching efficiency by up to the third power of the cavity finesse.

Two different semiconductor materials are used in fabricating these devices, GaAs

and InP. Both materials are analyzed and compared in terms of switching energy requirement, nonlinear coefficients, speed limitation and ease of fabrication. In addition, two different fabrications techniques are used to realize the ring structure layout, laterally and vertically coupled.

The round trip phase of the microring resonator can be controlled by changing its refractive index. This can be accomplished by free carrier injection induced by two-photon absorption or single-photon absorption. As a result, a temporal blue shift in the resonator resonance wavelength is observed. When these carriers diffuse to the waveguide walls, the effect diminishes. A probe beam, tuned to one of the resonator resonant wavelengths, is used to capture the dynamic change in the transmission function of the resonator.

All-optical switching is demonstrated using a single microring resonator, with few tens of picojoules switching energy and a switching window approaching 30 GHz, limited by the carrier lifetime of the guiding material. Moreover, such a device is used in time division demultiplexing a stream of data channels as well as spatial pulse routing with approximately 8 dB cross-talk noise, limited by fabrication tolerances. More complicated structures of these resonators are proposed and used to achieve a set of functionally complete photonic logic gates.

NONLINEAR OPTICAL SEMICONDUCTOR

MICRO-RING RESONATORS

by

Tarek A. Ibrahim

Dissertation submitted to the Faculty of the Graduate School of the
University of Maryland, College Park in partial fulfillment
of the requirements for the degree of
Doctor of Philosophy
2003

Advisory Committee:

Professor Julius Goldhar, Chair/Advisor
Professor Ping-Tong Ho, Co-advisor
Professor Chi H. Lee
Professor Wendell T. Hill, III
Dr. Kenneth J. Ritter

© Copyright by

Tarek A. Ibrahim

2003

DEDICATION

To my wife, Dalia, with love.

ACKNOWLEDGEMENTS

First of all, I would like to express my greatest appreciation and my gratitude to my advisor, Professor Julius Goldhar, for his generous support and guidance. His profound insight into physics and inspiring suggestions helped me not only to understand but also to solve and move forward through many challenging problems.

Equally, sincere appreciation also goes to Professor Ping-Tong Ho for leading me into the world of micro photonics and guiding me through the course of this project. I have benefited from his knowledge, experience, and nice personality.

I am very grateful to Professor Chi H. Lee for his support, encouragement, and suggestions. The collaboration with his group was very fruitful. In particular, I would like to thank Dr. WeiLou Cao, J. Li and, Y. Kim.

I sincerely appreciate Dr. Ken Ritter for his fruitful discussions and positive feedback. I would also like to thank Professor Wendell T. Hill III for reading, discussing, and commenting on my thesis.

I would also like to gratefully acknowledge some of my current and former colleagues, Dr. Phillipe Absil, Dr. Sai Chu, Dr. Yongzhang Leng, Dr. Victor Yun, Li-Chiang Kuo, and Kuldeep Amarnath, for all the precious time that they have dedicated to teach and help me either inside the clean room or inside the lab. In particular, I would like to thank Dr. Vien Van and Dr. Rohit Grover for supervising and training me inside the clean room. I am very thankful to Dr. Marshall Saylors, Dr. Christopher J. K. Richardson, Dr. Paul Petruzzi, Dr. P. Cho, E. Awad, Russell Frizzell, Lisa Lucas, Toby Olver, Dan Hinkel and Scott Horst for their instructions and advices in the different stages of my graduate study. I have learned so much from them as I gradually gained experience in the field of photonics.

The electron beam lithography for the InP microresonators was performed at the Cornell Nanofabrication Facility (a member of the National Nanofabrication Users Network) which is supported by the National Science Foundation under Grant ECS-9731293, its users, Cornell University and Industrial Affiliates.

This work was supported by the University of Maryland Graduate Fellowship, and the Distinguished LPS-ECE Graduate Research Assistantship.

TABLE OF CONTENTS

LIST OF TABLES

LIST OF FIGURES

CHAPTER 1

INTRODUCTION

The use of light for communication purposes dates back to the use of smoke and fire to convey a piece of information, such as a victory in a war. There are many reasons that made photons more popular to use in information processing. Photons are able to accomplish certain functions better than electrons by virtue of their special properties. The very large bandwidth, $\sim 10^{15}$ Hz, gives optics a potential speed for signal processing which is well beyond any electronics. Indeed, the shortest optical pulses of < 10 fs give light three order of magnitude advantage over the shortest electrical pulse [1]. When it comes to interconnects on a chip, the wiring capacitance will set the speed limits of integrated circuits. Besides, photons can pass through each others unperturbed in the absence of a nonlinear interaction, whereas electrons interact with each other even at a distance. In Table 1.1, we summarize the potential advantages and disadvantages of using optics in signal processing.

The turn of the new millennium witnessed an explosion in data-traffic volume, due to the ongoing increasing demand on the Internet. Therefore, all-optical switching devices have been looked at as key components for future high-speed optical communication systems. Such devices would enable highly parallel logic operations as well as ultrafast

Table 1.1: Advantages and disadvantages of optics in signal processing.

Advantages of optics	Disadvantages of optics
Large bandwidth $\sim 10^{15}$ Hz	High power requirement $\sim$ 1 W peak power
Low propagation loss	Interfacing with electronics
Low cross talk	Wavefront distortions
High degree of parallelism	
Small dimensions	
Ultrashort pulses $\leq$ 10 fs	
Coherence properties	

switching because of the instantaneous nature of virtual optical transitions [2]. With the recent advances in semiconductor fabrication, there has been a noticeable effort to bring those devices on semiconductor platforms to the real world.

An ideal all-optical switch is the one that poses the following characteristics. It would only require as little as sub picojoule of energy to switch with at least 20 dB switching contrast. Beside compactness, it is desirable to integrate such a device with already established optoelectronics devices on a planar integrated photonic circuit. One category of devices that has a great potential to meet those requirements is microring resonators.

1.1 Goal of this Work

In the last few years microring resonators have been proposed and fabricated on glass [3, 4], SiO_2 [5], GaAs [6–9], InP [10–13], and polymer [14–16] platforms. The foci of the previous work have been the realization, fabrication and optimization of these devices for linear applications such as Wavelength Division Multiplexing (WDM) and add/drop filters. It is the goal and novelty of this work to investigate the nonlinear characteristics of GaAs and InP based semiconductor microring resonators and demonstrate the use of such passive devices for optical switching applications and photonic logic gates.

1.2 What is a Ring Resonator?

A ring resonator is simply a waveguide shaped into a ring structure as shown in Fig. 1.1. When an input electric field, E_i, is coupled to the ring waveguide through an external bus waveguide, a positive feedback is induced and the field inside the ring resonator, E_r, starts to build up. Coupling between the straight and the ring waveguide is achieved through the evanescent wave. Therefore, the gap and coupling length between them determine how much power is coupled from the straight waveguide to the ring waveguide and vise versa. The feedback mechanism is simply induced by the ring waveguide and therefore there is no need for any Bragg gratings, mirrors, or distributed feedback waveguides which are more difficult to fabricate. In such configuration, only certain wavelengths will be allowed to resonate inside the ring waveguide, thus frequency se-

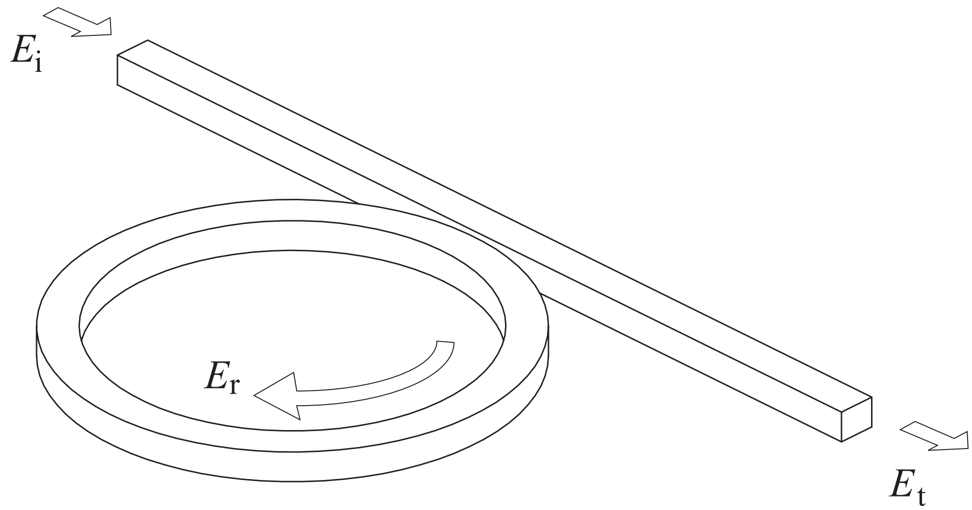

Figure 1.1: Schematic diagram for a ring resonator coupled to a single waveguide.

lectivity is obtained. A resonant mode will have a wavelength that satisfies

$$m\lambda_m = nL, \qquad m = \text{integer}. \tag{1.1}$$

Here, m is the longitudinal mode number, λ_m is the resonant mode wavelength, n is the refractive index of the guiding material, and L is the circumference of the ring resonator. The electric field circulating inside the resonator is given by

$$E_{\mathrm{r}}(t) = -j\kappa E_{\mathrm{i}}(t) + ra\,e^{j\phi}E_{\mathrm{r}}(t-\tau), \tag{1.2}$$

where κ and r are the field coupling and transmission coefficients between the straight and ring waveguides such that $\kappa^2 + r^2 = 1$, $a = e^{-\alpha_0 L/2}$ is the round trip field transmission, α_0 is the propagation loss inside the microring in cm^{-1}, and τ is the round trip time of the ring resonator. The resonator round trip phase, ϕ, is given by

$$\phi = \frac{2\pi}{\lambda} nL. \tag{1.3}$$

The transmitted or throughput field at the output of the straight waveguide, E_{t}, is given by

$$E_{\mathrm{t}}(t) = rE_{\mathrm{i}}(t) - j\kappa a e^{j\phi} E_{\mathrm{r}}(t-\tau), \tag{1.4}$$

At steady state, the transmission-transfer function of the resonator can be written as

$$\frac{E_{\mathrm{t}}}{E_{\mathrm{i}}} = \frac{r - ae^{j\phi}}{1 - rae^{j\phi}}. \tag{1.5}$$

A close examination of Eq. 1.5 indicates that a ring resonator is very similar to a Fabry-Perot cavity. In the particular case shown in Fig. 1.1, the corresponding Fabry-Perot cavity would have an input mirror with a field reflectivity r, and a fully reflecting output mirror. However, the field propagating inside the ring cavity is a traveling wave in contrast to the Fabry-Perot cavity which resonates a standing wave.

1.2.1 Field Enhancement

At steady state, the field circulating inside the resonator can be also written as

$$E_{\mathrm{r}} = -j\kappa E_{\mathrm{i}} + rae^{j\phi} E_{\mathrm{r}}. \tag{1.6}$$

Therefore the ratio of the circulating field to the input field is given by

$$\frac{E_{\mathrm{r}}}{E_{\mathrm{i}}} = \frac{-j\kappa}{1 - rae^{j\phi}}. \tag{1.7}$$

We define the Field Enhancement Factor, FE, as the magnitude of the ratio of the circulating field inside the resonator, E_{r}, to the input field, E_{i}, at resonance, i.e., $\phi = 0$. The FE is thus given by

$$\mathrm{FE} = \left|\frac{E_{\mathrm{r}}}{E_{\mathrm{i}}}\right|_{\phi=0} = \frac{\kappa}{1-ar}. \tag{1.8}$$

The higher the FE, the higher the built up intensity inside the resonator and thus the lower the amount of input power required to induce nonlinear effects. Therefore, it is very important to understand what factors limit the FE for a given microring resonator. In Fig. 1.2, we plot Eq. 1.8, for different values of the round trip field transmission, a, and field coupling coefficient, κ. As can be seen, the higher the value of a and therefore the lower thr round trip loss, the higher the FE obtained by the resonator. Also, for a given value of a, the FE peaks at a maximum then decreases as a function of κ, as we will discuss in the following subsection.

1.2.2 Critical Coupling

The maximum FE that is feasible by a ring resonator can be obtained mathematically by differentiating Eq.1.8 with respect to κ, and equating the result to 0. Doing the math, we find that this happens when $a = r$, and it yields a maximum FE equal to $1/\kappa$. Moreover, at resonance, the transmission-transfer function, given by Eq. 1.5, has a magnitude of 0, when the above condition is met. That is all the power coupled to the resonator is equal to the power consumed by or lost inside the resonator. This criterion is known as critical coupling and is desirable in some applications where high switching contrast is required. In Fig. 1.3, we plot the throughput transmission and the normalized resonating intensity

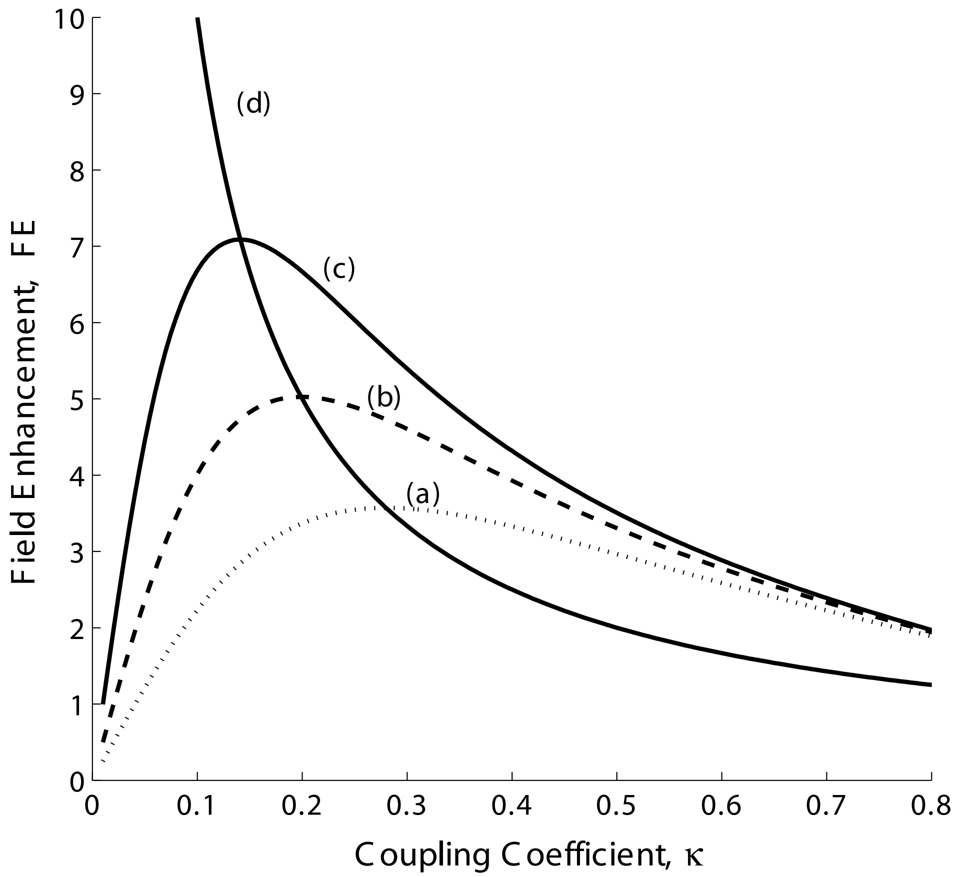

Figure 1.2: Field Enhancement, FE, versus the coupling coefficient κ, for: (a) $a = 0.96$, (b) $a = 0.98$, (c) $a = 0.99$, and (d) $a = (1-\kappa^2)^{1/2}$

for a critically coupled microring resonator. At resonance, a complete extinction is achieved for the throughput transmitted intensity. On the other hand, the circulating intensity inside the ring is much higher than the input intensity due to the FE effect.

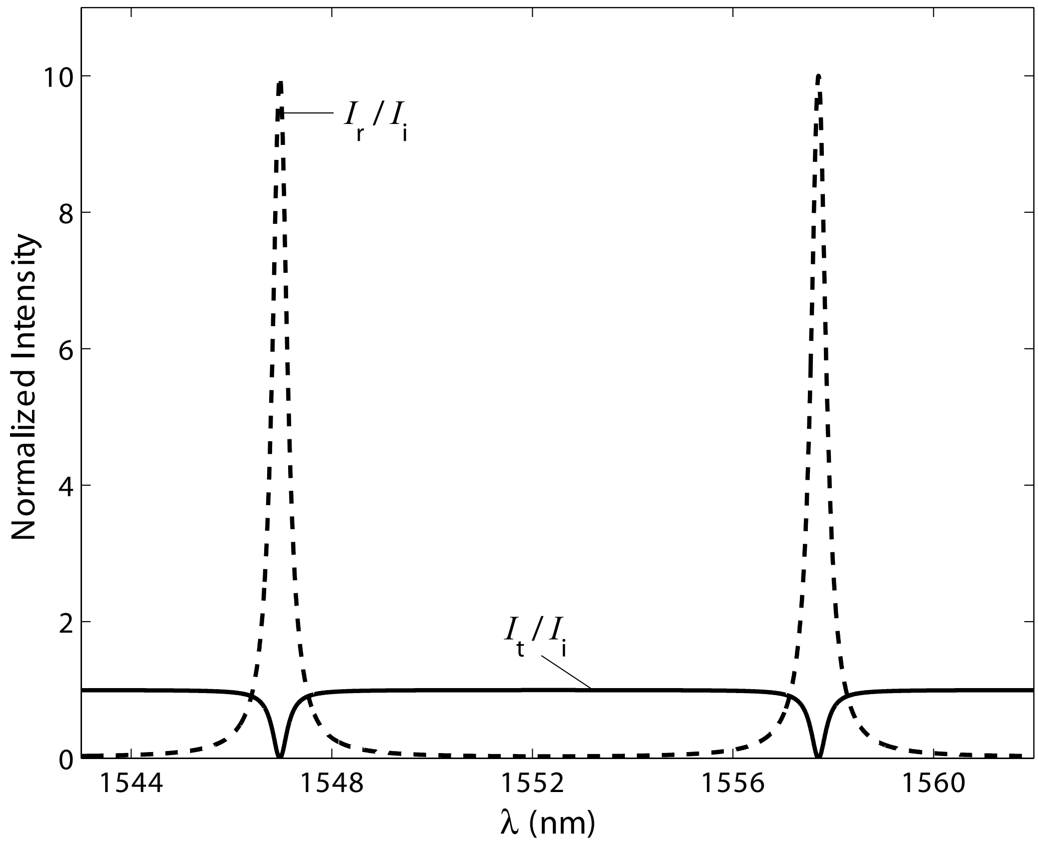

Figure 1.3: Throughput intensity transmission (solid line) and normalized resonating intensity (dashed line) for a critically coupled microring resonator that has a refractive index of 3.4, diameter of 20 μm, and a power coupling coefficient $\kappa^2 = 10\%$.

1.2.3 Resonator Bandwidth

The resonance bandwidth determines how fast optical data can be processed by a microring resonator. The resonator bandwidth is given by the full width at half maximum (FWHM) of the microring intensity resonance or its 3-dB bandwidth. From Eq. 1.7, the intensity inside the resonator can be written as

$$\frac{I_{\mathrm{r}}}{I_{\mathrm{i}}} = \left|\frac{E_{\mathrm{r}}}{E_{\mathrm{i}}}\right|^2 = \frac{\kappa^2}{1 + a^2r^2 - 2ar\cos^2\phi}. \tag{1.9}$$

At FWHM, this yields

$$\cos\phi_{\pm} = \frac{4ar - a^2r^2 - 1}{2ar}, \tag{1.10}$$

where $\phi_{\pm} = \phi_0 \pm \delta\phi$. Using Taylor expansion,

$$\cos(\phi_0 + \delta\phi) = \cos\phi_0 - \delta\phi\sin\phi_0 - \frac{(\delta\phi)^2}{2}\cos\phi_0 + \ldots, \tag{1.11}$$

where $\delta\phi \ll 2\pi$, and $\phi_0 = 2m\pi$ is the phase at resonance. From Eq. 1.10 and Eq. 1.11, we obtain

$$\delta\phi \approx \frac{1 - ar}{\sqrt{ar}}. \tag{1.12}$$

Using Eq. 1.3 and Eq. 1.12, the FWHM bandwidth is given by

$$\begin{aligned} \delta\lambda_{\mathrm{FWHM}} &= 2\delta\lambda \\ &= 2\left(\frac{\lambda_0^2}{2\pi nL}\delta\phi\right) \\ &\approx \frac{\lambda_0^2}{\pi nL}\frac{1 - ar}{\sqrt{ar}}. \end{aligned} \tag{1.13}$$

To understand how the bandwidth of the resonator is affected by the coupling coefficient, κ, we will consider a critically coupled microring resonator. In such a case, Eq. 1.13 results in

$$\delta\lambda_{\mathrm{FWHM}} \approx \frac{\lambda_0^2}{\pi nL}\frac{\kappa^2}{\sqrt{1 - \kappa^2}}. \tag{1.14}$$

Therefore, the lower the coupling coefficient,κ, the smaller the resonance bandwidth. On the other hand, Eq. 1.8 shows that the lower the coupling coefficient, κ, the higher the FE of the resonator.

1.2.4 Resonator Finesse

The finesse of the resonator is given by

$$\mathrm{F} = \frac{\Delta\lambda_{\mathrm{FSR}}}{\delta\lambda_{\mathrm{FWHM}}}, \tag{1.15}$$

where $\Delta\lambda_{\mathrm{FSR}} = \lambda_0^2/nL$ is the free spectral range or axial mode spacing between resonances. By substituting from Eq. 1.13 into Eq. 1.15, we obtain

$$\mathrm{F} = \frac{\pi\sqrt{ar}}{1-ar}. \tag{1.16}$$

The finesse gives the resoling power of the resonator when used as a transmission filter. An interesting fact is that a resonator finesse is independent on its dimension or circulating light wavelength. It is only a function of coupling coefficient and internal loss. The finesse of a critically coupled microring resonator can be approximated by π/κ^2, for $\kappa \ll 1$.

1.2.5 Cavity Lifetime

A parameter that is inversely proportional to the resonator bandwidth is the cavity or photon lifetime. It can be defined as the average time that a photon coupled to the resonator will stay inside the cavity before it is absorbed or transmitted. The photon lifetime is thus given by

$$\begin{aligned} \tau_{\mathrm{ph}} &= \frac{1}{\delta f_{\mathrm{FWHM}}} = \frac{c}{\pi nL}\frac{\sqrt{ar}}{1-ar} \\ &= \frac{nL}{c}\mathrm{F}, \end{aligned} \tag{1.17}$$

where c is the speed of light in free space. Eq. 1.17 states that a photon will circulates inside the resonator for a number of round trip times equal to the cavity finesse, before it is transmitted to the throughput port or absorbed inside the resonator. This will be the ultimate time limit of optical signal processing by ultrafast nonlinear processes inside the microring cavity. Therefore, cavity size and finesse have to be considered in designing the device for a particular application.

1.2.6 Cavity Q Factor

In analogy with electrical circuits, the quality factor of an optical cavity due its internal losses and external coupling can be defined as

$$\frac{1}{\mathrm{Q}} \equiv \frac{\text{energy dissipated}}{\omega \times \text{energy stored}}, \tag{1.18}$$

where ω is the frequency of light coupled to the resonator. The quality factor of the resonator can be calculated from [17]

$$\begin{aligned} \mathrm{Q} &\equiv \frac{\lambda_0}{\delta\lambda_{\mathrm{FWHM}}} \\ &\equiv \frac{\pi n L}{\lambda_0} \frac{\sqrt{ar}}{1 - ar}. \end{aligned} \tag{1.19}$$

As can be seen in Eq. 1.19, the quality factor of the resonator is a function of its dimension as well as the resonance wavelength. Therefore, from now on we will always use the finesse, F, and the field enhancement factor, FE, of the resonator in measuring nonlinear enhancements.

1.3 All-Pass or Phase Filter

For a lossless microring resonator, i.e. $a = 1$, the magnitude of the transmission-transfer function, given by Eq. 1.5, is 1 regardless of ϕ. However an examination of its phase reveals a phase enhancement similar to the field enhancement discusses earlier. The phase function of the ring resonator, ϕ_{eff}, can be obtained by considering the phase of the right hand side of Eq. 1.5. This is given by [18]

$$\phi_{\text{eff}} = \pi + \phi + \tan^{-1}\frac{r\sin\phi}{a - r\cos\phi} + \tan^{-1}\frac{ar\sin\phi}{1 - ar\cos\phi}. \tag{1.20}$$

In Fig. 1.4, we plot Eq. 1.20 for different values of the field coupling coefficient, κ, for a lossless resonator $(a = 1)$. Near resonance, i.e. $\phi = 0$, the slope of the effective phase becomes very steep, and hence the device output phase is very sensitive to change in the single-pass phase shift of the microring. This phase enhancement can be observed by introducing the microring resonator into one arm of a Mach-Zehnder interferometer (MZI), for example.

1.4 Optical Add/Drop Filter

Unlike Fabry-Perot cavities, Bragg gratings, and distributed feedback waveguide devices, the ring geometry permits more than one waveguide to be coupled to the ring resonator. This in return allows multiple input/output accessibility and no need for external circulators to manipulate the input, reflected and throughput data streams. For instance, if one more waveguide is coupled to the phase filter described earlier, an optical add/drop

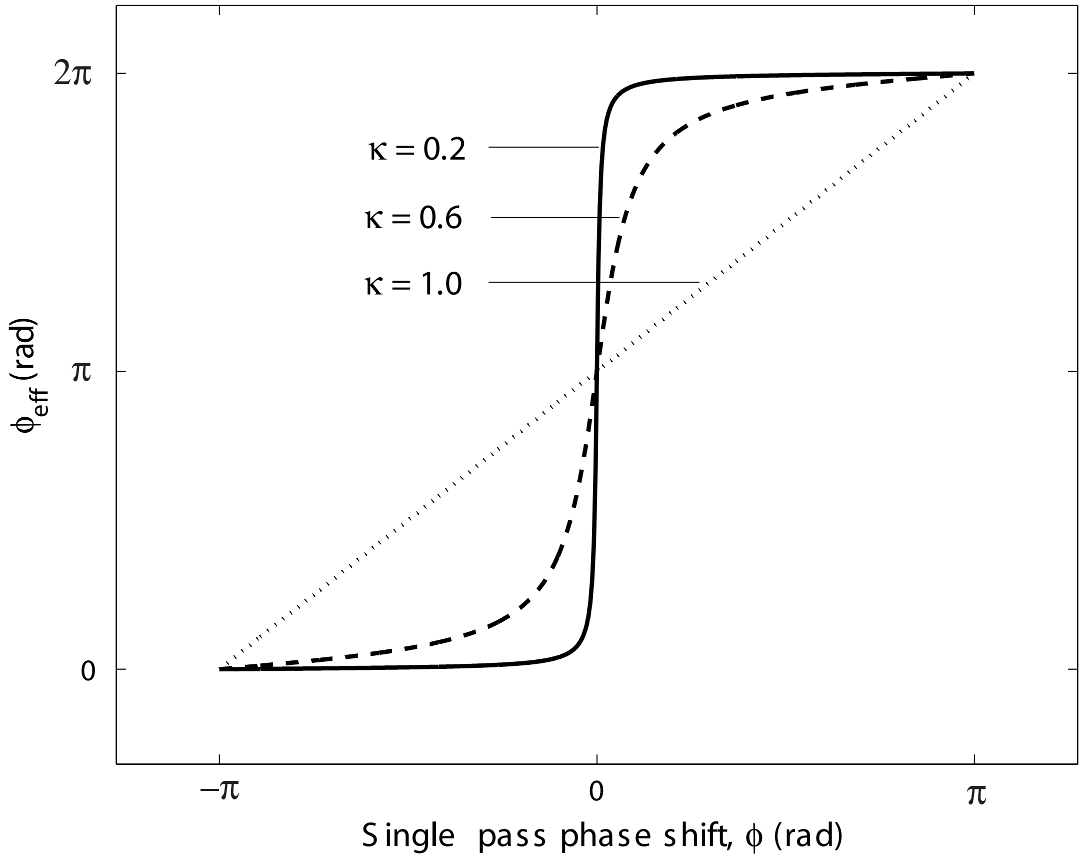

Figure 1.4: Phase enhancement of a lossless microring resonator and different values of the field coupling coefficient, κ.

filter is obtained, as shown in Fig. 1.5. At steady state, the transmission-transfer function at the drop and throughput ports are given by

$$\frac{E_\mathrm{d}}{E_\mathrm{i}} = \frac{-\kappa_1\kappa_2 a^{1/2} e^{j\phi/2}}{1 - ar_1r_2e^{j\phi}}, \tag{1.21a}$$

$$\frac{E_\mathrm{t}}{E_\mathrm{i}} = \frac{r_1 - ar_2e^{j\phi}}{1 - ar_1r_2e^{j\phi}}, \tag{1.21b}$$

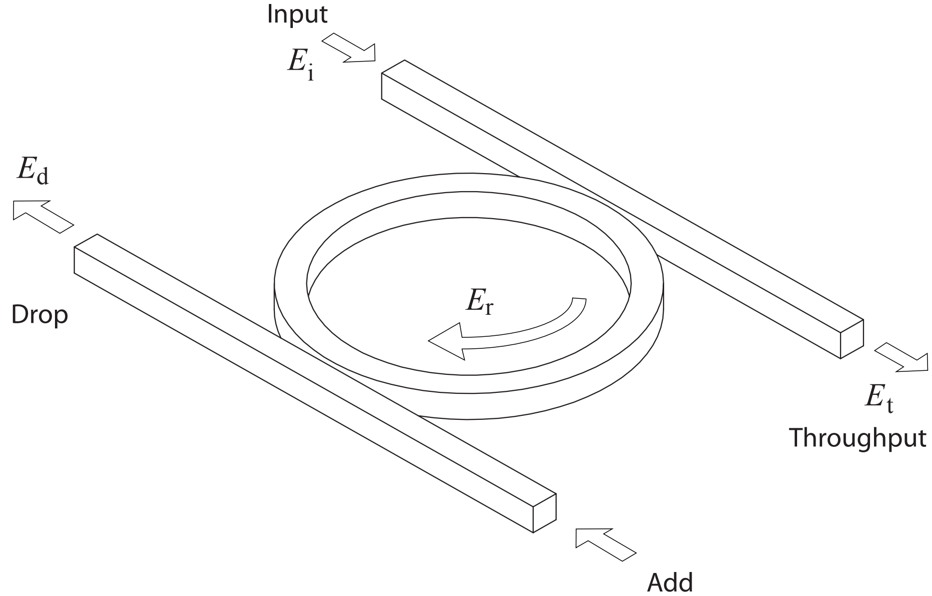

Figure 1.5: Schematic diagram for a ring resonator coupled to two waveguides, in an add/drop filter configuration.

where κ_1, and r_1 are the field coupling and transmission coefficients between the ring and the input waveguide while κ_2, and r_2 are the field coupling and transmission coefficients at the output waveguide. An interesting criterion of this device can be observed in Eq. 1.21. That is, a complete power transfer between the input port and the drop port can be obtained at resonance ($\phi = 0$), for a lossless microring resonator that has a symmetric coupling, i.e. $\kappa_1 = \kappa_2$. At the same time, the throughput port will have a complete extinction, thus this condition is referred to as critical coupling in analogy with what have been discussed earlier in subsection 1.1.2.

1.5 Why Microring Resonators?

Now we can summarize the advantages attained by microring resonators over other conventional optical cavities:

- Geometry:

  The ring geometry by itself is unique. The ring waveguide supports a traveling wave rather than a standing wave. Hence, coupling can be at any point on the ring circumference. Furthermore, it allows more than one waveguide to be coupled to the ring. Therefore, multiplexing, demultiplexing, and routing can be achieved with no need for external circulators.

- Simplicity:

  Fabrication of microring resonators is straightforward. There is no need for any mirrors, Bragg gratings, or distributed feedback waveguides to achieve the positive feedback.

- Materials:

  There is no need for any exotic materials to fabricate microring resonators. Semiconductors fabrications are well developed and their high refractive indices allow smaller radii bends to be feasible. Bending losses decrease exponentially with increasing core-cladding refractive index contrast. This made high index contrast a fundamental requirement for very large scale integration (VLSI) photonics [19]. A 2 μm microring resonator with a finesse of 100 will have a cavity lifetime of

10 ps. Therefore, 100 GHz data can be processed by such a device. Semiconductors also allow microrings to be integrated with other optoelectronics devices such as micro lasers, amplifiers, and detectors.

CHAPTER 2

NONLINEAR CHARACTERISTICS OF SEMICONDUCTORS

The use of semiconductor materials as nonlinear optical elements bridges the gap between optics and electronics. It opens the possibility for integrating the laser sources, signal processing elements, and detectors on the same platform. In this regard, the III-V binary semiconductors, such as GaAs and InP, have acquired great attention in the last few decades because they are direct bandgap materials and possess higher nonlinear coefficients than their competing materials. Another attractive feature of binary semiconductors is that they can be combined or alloyed to form ternary or quaternary compounds. Doing so, makes it possible to vary the bandgap of the material continuously together with its band structure, electronic, and optical properties. As an example, the bandgap energy of the ternary compound $Al_xGa_{1-x}As$ depends on the mole fraction x. Another important quaternary compound that we will consider is $In_{1-x}Ga_xAs_yP_{1-y}$. Therefore, one can design ternary and quaternary compounds to be transparent for optical channel waveguides or active for lasers and amplifiers at the 1550 nm communication window.

In this chapter we will discuss different nonlinear processes that affect the performance of semiconductor microring resonators as all-optical signal processing tools.

2.1 Thermal Nonlinearities

Semiconductors band gap energies decrease with increasing temperature due to the change in the Fermi-Dirac distribution. The bandgap change in most semiconductors is -0.5 meV/K [20]. In addition, as temperature changes the thermal expansion of a semiconductor cavity and the change in the refractive index alters the position of the resonant modes. As we showed in chapter 1, the resonant modes of a microring resonator are given by

$$m\lambda_m = nL. \tag{2.1}$$

By differentiating Eq. 2.1 with respect to temperature, T, we obtain

$$m\frac{d\lambda_m}{d\mathrm{T}} = \frac{dn}{d\mathrm{T}}L + n\frac{dL}{d\mathrm{T}}. \tag{2.2}$$

By dividing Eq. 2.2 by Eq. 2.1, we obtain

$$\frac{1}{\lambda_m}\frac{d\lambda_m}{d\mathrm{T}} = \frac{1}{n}\frac{dn}{d\mathrm{T}} + \frac{1}{L}\frac{dL}{d\mathrm{T}}. \tag{2.3}$$

Eq. 2.3 shows the temperature dependence of the microring resonant wavelength as a function of the material thermo-optic coefficient, $dn/d\mathrm{T}$, and the thermal expansion coefficient, $L^{-1}dL/d\mathrm{T}$.

2.1.1 Temperature Tuning

Using GaAs and InP microring notch filters devices, we measured the thermo-optic effect in both materials as follows. We mounted the devices on a temperature controlled base which has a thermo-electric (TE) cooler and a thermometer. We used the output spontaneous emission of an erbium doped fiber amplifier (EDFA) as the input light to the device. This allows us to monitor the change in the spectrum of the microring resonances. By changing the substrate temperature and monitoring one of the resonant modes wavelength, we measured the left hand side of Eq. 2.3. In Fig. 2.1, we plot the wavelength detuning of one of the microring resonant modes for both GaAs and InP around 1550 nm. As expected, a linear line is obtained with a slope of 0.109 and 0.113 nm/^{o}C, respectively. The thermal expansion coefficient for GaAs is $6 \times 10^{-6}/^{o}$C, and for InP is $4.56 \times 10^{-6}/^{o}$C at room temperature [21,22]. From Eq. 2.3, we calculate the the thermo-optic coefficient, dn/dT, for GaAs to be $2.17 \times 10^{-4}/^{o}$C, and for InP to be $2.19 \times 10^{-4}/^{o}$C.

The above experiment suggests that tuning of microring filters can be accomplished by locally heating the microring devices, which is a useful feature for applications such as widely tunable wavelength filters for reconfigurable Wavelength Division Multiplexing (WDM) systems [23].

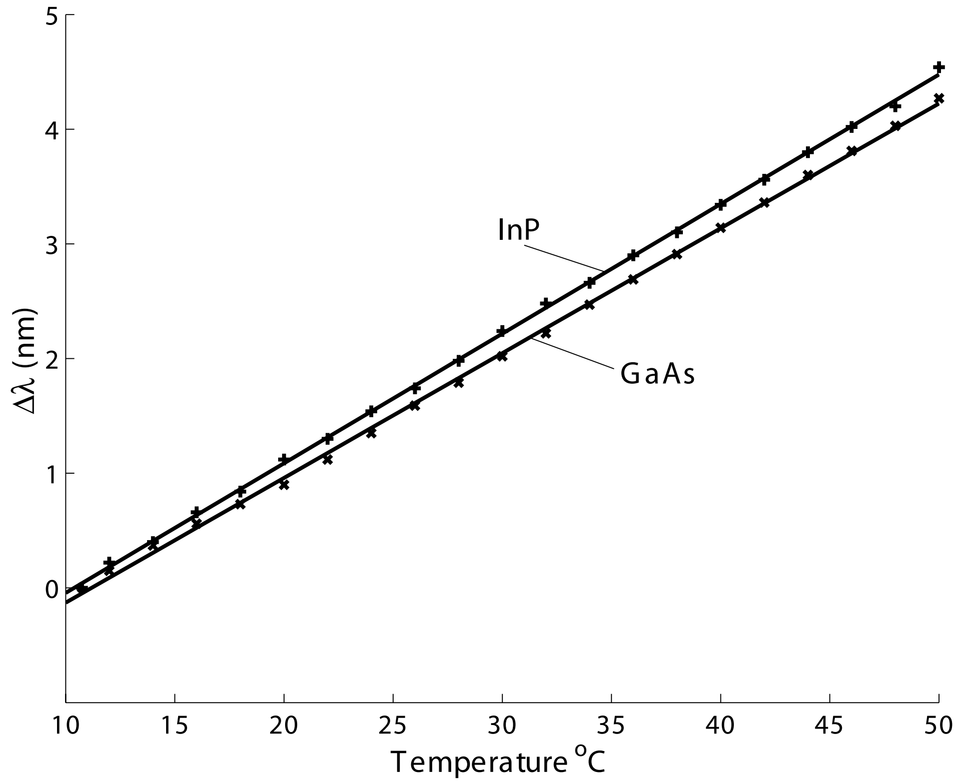

Figure 2.1: Measured temperature dependence of a resonant mode wavelength of GaAs and InP microring resonators around 1550 nm.

2.1.2 Optical Bistability

The phenomenon of Optical Bistability (OB) arises from a combination of the nonlinearity in the radiation-matter interaction and of a feedback mechanism [24, 25]. Generally, there are two classes of OB: absorptive and dispersive OB. Absorptive OB occurs whenever the input wavelength is close to the atomic resonance of the material. An increase in the input power produces an increase in saturation, i.e., in the degree of transparency of the medium. This allows the internal field of the cavity to increase, which in return increases the saturation. Such positive feedback loop causes the switch-up process. When the input power is decreased, the internal field is intense enough to maintain the saturation. As a consequence, the transmitted power is held “ON” and one obtains a hysteresis curve. InGaAsP can be designed to have the band edge around 1.45 μm and thus can show absorptive OB when pumped at 1.55 μm. On the other hand, dispersive OB occurs whenever the input wavelength is tuned far away from the atomic resonance and hence the material is transparent. The frequency of the incident field is kept near one of the cavity frequencies, but detuned enough so that the transmission is low. An increase in the input intensity produces an increase in the intensity of the internal field. Because the refractive index is a function of intensity, this changes the optical length of the medium in such a way that the cavity resonance is driven closer to the input frequency. In return, it increases the internal field intensity. Thus, again, we have a positive feedback loop which produces up-switching. When the incident power is decreased, the internal field is intense enough to maintain resonance between the cavity and the input frequency, and therefore one again obtains a hysteresis. This will be the case for GaAs, whose band edge is around 0.8 μm and the input wavelength is at 1.55 μm.

Experimentally, we have demonstrated OB in GaAs/AlGaAs microring resonators using an add/drop filter [26]. Even though, the bistability was due to the thermal effect, it follows the theory and proves the concept. The output power of a tunable external-cavity laser diode was modulated at a low frequency (10 Hz) using a mechanical chopper. Its wavelength was tuned to one of the microring resonant modes. The polarization of the input beam was controlled using a fiber polarization controller (FPC) to match that of the microring mode. The input beam was optically amplified using an EDFA. The amplified beam was then split into a reference beam and a probe beam. The reference beam was attenuated and monitored by a photodetector, D1. The probe beam was coupled into the input waveguide of the microring resonator using a conically tipped fiber, and the output was measured at the drop-port of the device using a second conically tipped fiber and then fed to a photodetector, D2. In the add/drop configuration used here, when the source is tuned to one of the microring resonances, the field circulating in the ring builds up to a much higher value than the input field, thus effectively lowering the switching threshold. In the switching measurement the source wavelength was tuned to 1561.3 nm, which is 0.3 nm red-detuned from the microring resonance wavelength of 1561 nm. The laser power was modulated at a 10 Hz frequency to give a 0 to 60 mW power variation at the input of the device. The time traces for the input and output signals are shown in Fig. 2.2(a). The switching time is in the microseconds range, indicating that switching was mainly due to the thermal effect. In Fig. 2.2(b), the dropped intensity is plotted versus the input intensity. Switching thresholds and hysteresis are clearly observed. This bistable behavior of the microring can be explained by a thermal increase in the effective ring index with increasing intensity.

Such device can be used as an optical buffer where a data of “1” can be latched on the “ON” state. Resetting the buffer to “0” can be achieved by cooling the microring resonator so that the effective refractive index of the resonator is reset to its original value. It can be used as a thermo-optical switch for packet routing and similar low

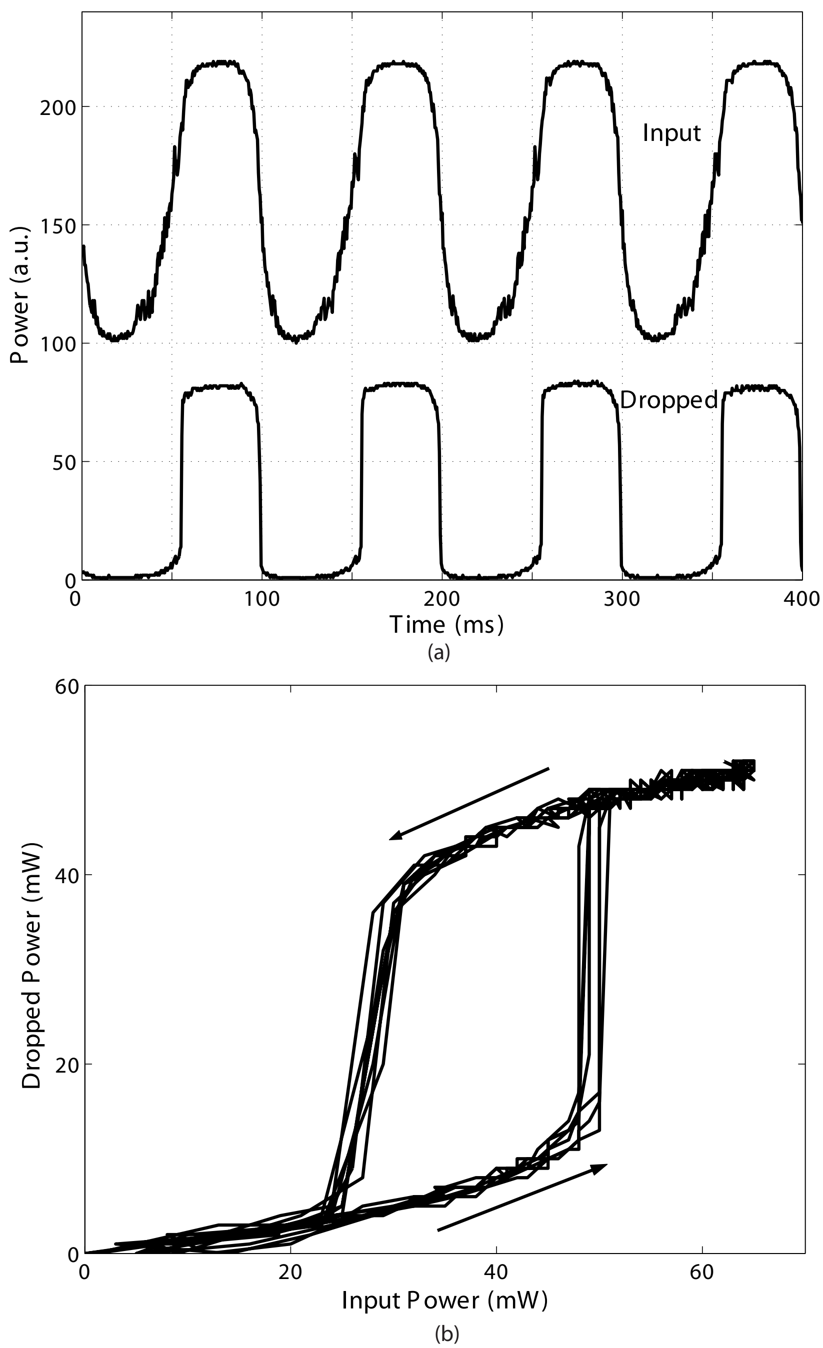

Figure 2.2: (a) Time traces for the input and dropped power of the bistable GaAs microring resonator. (b) The dropped power versus the input power showing the bistability hysteresis.

frequency optical switching applications.

2.2 Nonresonant Nonlinearity

The instantaneous nonlinear optical response of a material can be described by writing the material polarization, P, as a power series of the electric field strength, E, as [27]

$$P(t) = \varepsilon_0[\chi^{(1)}E(t) + \chi^{(2)}E^2(t) + \chi^{(3)}E^3(t) + \ldots], \tag{2.4}$$

where ε_0 is the free space permittivity, and $\chi^{(N)}$ refers to the N^{th} order nonlinear optical susceptibilities. The first order susceptibility, $\chi^{(1)}$, gives rise to the linear refractive index,

$$n_0 = \text{Re}\left\{\sqrt{1+\chi^{(1)}}\right\}, \tag{2.5}$$

and the linear absorption coefficient,

$$\alpha_0 = \frac{4\pi}{\lambda}\text{Im}\left\{\sqrt{1+\chi^{(1)}}\right\}. \tag{2.6}$$

The second order of the nonlinear susceptibility, $\chi^{(2)}$, is responsible for describing second harmonic generation, sum and difference frequency generation, and optical parametric oscillation. The second order nonlinear optical interactions can occur only in noncentrosymmetric crystals, that is in crystals that do not display inversion symmetry. The third order nonlinear susceptibility, $\chi^{(3)}$, describes third harmonic generation, and intensity-dependent refractive index processes such as self- focusing, four-wave mixing, saturable absorption, and two-photon absorption. These third order nonlinear optical interactions can take place both in centrosymmetric and noncentrosymmetric media. The third order contribution to the nonlinear polarization is given by

$$P^{(3)}(t) = \varepsilon_0 \chi^{(3)} E^3(t). \tag{2.7}$$

Let us consider the case in which the applied field is monochromatic and is given by

$$E(t) = E \cos \omega t. \tag{2.8}$$

Then, since $\cos^3 \omega t = \frac{1}{4}\cos 3\omega t + \frac{3}{4}\cos \omega t$, the nonlinear polarization can be expressed as

$$P^{(3)}(t) = \frac{1}{4}\varepsilon_0 \chi^{(3)} E^3 \cos 3\omega t + \frac{3}{4}\varepsilon_0 \chi^{(3)} E^3 \cos \omega t. \tag{2.9}$$

The first term in Eq. 2.9 describes a third harmonic generated term at 3ω due to an applied field at frequency ω. The second term in Eq. 2.9 describes a nonlinear contribution to the polarization at the frequency of the incident field. Therefore, this term leads to a nonlinear contribution to the refractive index experienced by a wave at frequency ω. The refractive index can be represented as

$$n = n_0 + n_2 I, \tag{2.10}$$

where

$$n_2 = \frac{3}{n_0^2 \varepsilon_0 c} \mathrm{Re}[\chi^{(3)}] \tag{2.11}$$

is an optical constant that characterizes the strength of the optical nonlinearity, and I is the intensity of the incident field. On the other hand, the imaginary part of $\chi^{(3)}$ gives rise to a nonlinear absorption coefficient given by

$$\alpha = \alpha_0 + \alpha_2 I, \tag{2.12}$$

where α_2 is the two-photon absorption coefficient and is given by

$$\alpha_2 = \frac{12\pi}{n_0^2 \varepsilon_0 c \lambda} \mathrm{Im}[\chi^{(3)}]. \tag{2.13}$$

2.3 Two-Photon Absorption

Multi-photon absorption is a nonlinear process through which more than one photon of energy lower than the bandgap energy of the material are absorbed simultaneously. This, in result, excites an electron-hole pair or a free electron in the conduction band and a free hole in the valence band. These free carriers therefore alter the electronic and optical properties of the material and result in nonlinear refraction as well as nonlinear absorption. When two photons having the same energy are involved, the process is always referred to as degenerate two-photon absorption (TPA), as shown in Fig. 2.3. TPA in direct bandgap semiconductors has been extensively analyzed and measured at different wavelengths [28–32]. It has been considered to be a limiting factor for ultrafast nonlinear switching in semiconductors because it degrades the signal as it propagates through the waveguide. On the other hand, various applications based on TPA have been demonstrated such as autocorrelation, optical thresholding, and all-optical switching [33–35]. In this section we will measure the TPA coefficient, α_2, for both GaAs and InP straight waveguides. This will help us to characterize its effects and limitations on our semiconductor microring resonators.

The attenuation of light as it propagates through an optical waveguide can be de-

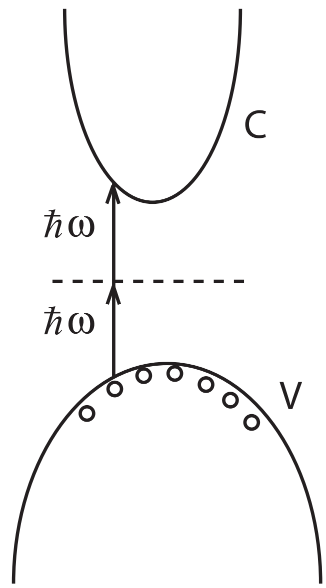

Figure 2.3: Schematic representation for the two-photon absorption process in a two-band model. The small circles denote electrons, C is the Conduction band, and V is the Valence band.

scribed by

$$\frac{dI}{dz} = -\alpha_0 I - \alpha_2 I^2 - (\sigma \Delta N) I, \tag{2.14}$$

where α_0 is the linear absorption coefficient including both intrinsic loss and scattering loss, I is the intensity across the waveguide, and σ is the free carrier absorption cross section in cm^2. The generated free carrier density, ΔN, by TPA is governed by

$$\frac{d\Delta N}{dt} = \frac{\alpha_2 I^2}{2\hbar\omega} - \frac{\Delta N}{\tau_c}, \tag{2.15}$$

where ω is the incident photons frequency, τ_c is the free carrier recombination or life time. Neglecting the carrier induced nonlinear loss, i.e., $\sigma = 0$, the intensity at the end of a waveguide of length L can be obtained by integrating Eq. 2.14 with respect to z. This leads to

$$I(L) = \frac{I(0)e^{-\alpha_0 L}}{1 + \alpha_2 I(0)\,\frac{\left(1 - e^{-\alpha_0 L}\right)}{\alpha_0}}, \tag{2.16}$$

where $I(0)$ is the intensity at $z = 0$. The total throughput of the waveguide, T, is defined as the ratio of the peak transmitted intensity after the waveguide to the peak incident intensity before the waveguide and is given by

$$\begin{aligned} T &= \frac{I_{\text{trans}}}{I_{\text{inc}}} \\ &= (1-R)^2\Gamma^2 \frac{I(L)}{I(0)} \\ &= (1-R)^2\Gamma^2 \frac{e^{-\alpha_0 L}}{1 + \alpha_2 (1-R)\Gamma I_{\text{inc}}\,\frac{\left(1 - e^{-\alpha_0 L}\right)}{\alpha_0}}, \end{aligned} \tag{2.17}$$

where Γ is the coupling efficiency into the waveguide, and R is the Fresnel reflectivity of the front and end facets. It is clear from Eq. 2.17 that a plot of the inverse transmittance, T^{-1}, versus the input incident light, I_{inc}, should consist of a straight line having a slope that is proportional to the TPA coefficient, α_2.

Experimentally, we used a mode-locked external cavity laser diode as the pump source tuned to 1550 nm. The typical pulse width was 35 ps. An external modulator was used to reduce the repetition rate from 5 GHz to 140 MHz. The pulses were then amplified using pre and post erbium doped fiber amplifiers (EDFA). A band-pass filter was used to suppress any amplified spontaneous noise before coupling light to the waveguide. The pump pulses were coupled to the waveguide using a conically tipped fiber. The output light was collected in the same manner, and then fed to a power me-

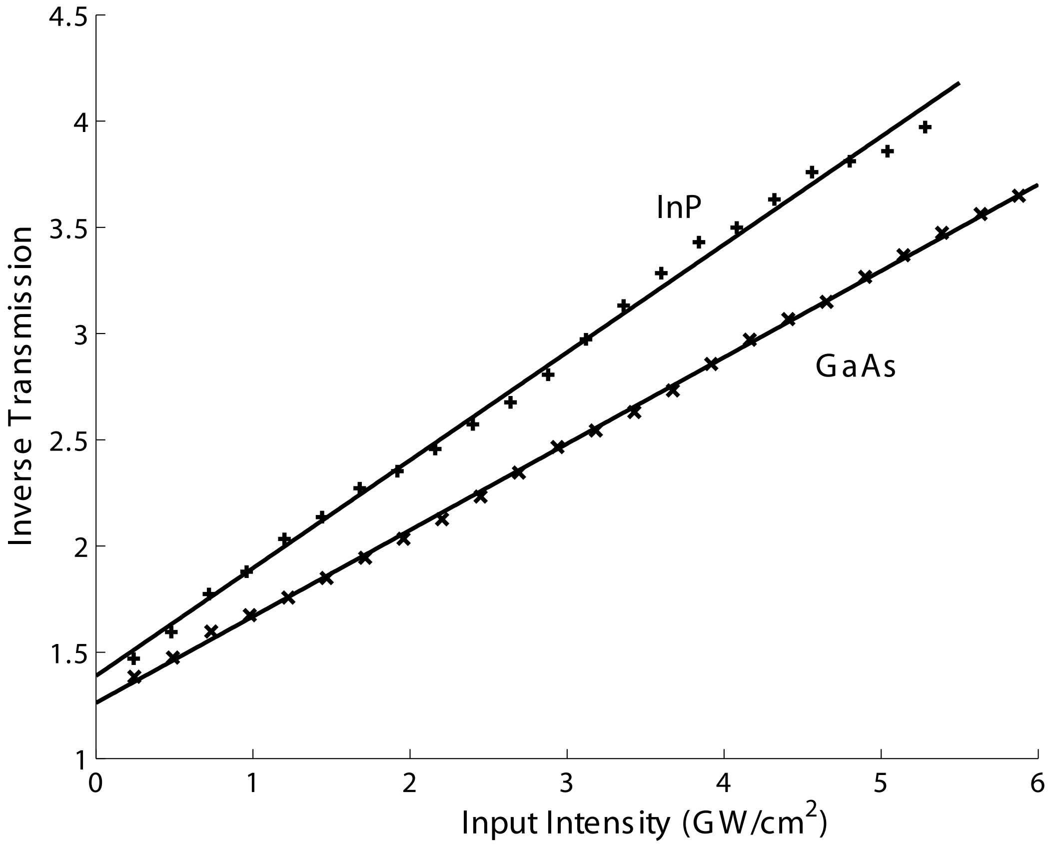

Figure 2.4: Inverse transmittance as a function of irradiance of 1550 nm 35 ps pulse for InP and GaAs straight waveguides.

ter. The input power at the waveguide was controlled by controlling the current of the post EDFA amplifier and measured by detecting a tapped portion of the input light. In Fig. 2.4, we plot the inverse transmittance as a function of the input pump intensity for both GaAs and InP straight waveguides. As predicted by Eq. 2.17, a straight line is obtained. With the value of α_0 known from linear measurements using the Fabry-Perot technique [36] , one can estimate $(1-R)\Gamma$ from the intersection with the y-axis. Moreover, from the slope of the line, α_2 can be obtained. From the lines slopes, we estimate a value of 18 and 43 cm/GW for the TPA coefficient, α_2, for the GaAs and InP straight waveguides, respectively.

CHAPTER 3

ENHANCED NONLINEAR RESPONSE IN MICRORING RESONATORS

Steady-state and dynamic transmission properties of resonators with intensity dependent nonlinearity have been extensively studied for Fabry-Perot resonators and fiber rings [37–40]. In chapter 1, we showed that at resonance the intensity inside a ring resonator is much higher than that at the input waveguide due to the positive feedback. In this chapter, we will carefully study such enhancement and its projection on the dynamic performance of the microring resonator for all-optical switching applications. We will concentrate on the reduction achievable in the switching power of a microring due to the resonant condition.

3.1 Small Signal Analysis

For a small range of detuning, i.e., much smaller than the 3-dB bandwidth of the microring resonance, a small signal analysis approach is enough to understand the dynamic behavior of the resonator and to determine its switching enhancement. In such analysis, we will assume that the linear parameters of the microring resonator are constants with

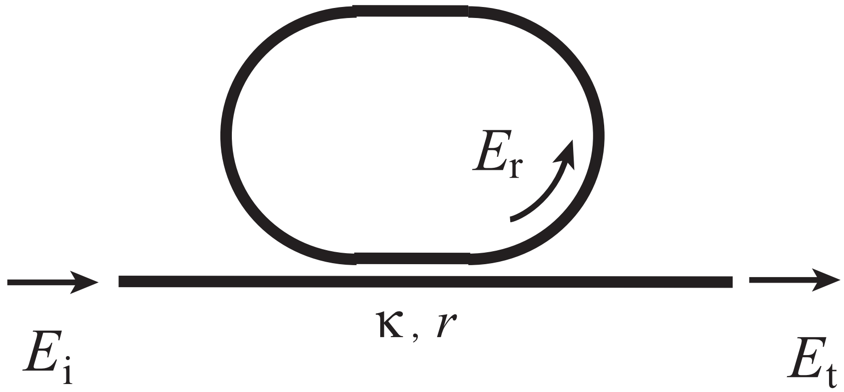

Figure 3.1: A schematic diagram of a ring resonator coupled to a straight waveguide.

respect to time. Without loss of generality, we will consider the notch filter case that we have introduced in chapter 1. As shown in Fig 3.1, it consists of a ring waveguide coupled to a single straight waveguide. At steady state, the field transmittance of the filter is given by

$$\frac{E_t}{E_i} = \frac{r - ae^{j\phi}}{1 - rae^{j\phi}}, \tag{3.1}$$

where a is the round trip field attenuation of the microring, r is the field transmittance coefficient, and ϕ is the round trip phase. At critical coupling, where the round-trip power loss is equal to the bus-to-ring coupling, the power transmittance of the filter can be written as

$$T = \left|\frac{E_t}{E_i}\right|^2 = \frac{2r^2(1-\cos\phi)}{1+r^4-2r^2\cos\phi}. \tag{3.2}$$

As can be seen in Fig. 3.2, a complete power extinction is obtained at the resonance frequency. At the same time, the optical intensity inside the ring is enhanced at resonance and results in a reduction in the effective switching threshold of the device. Such switching threshold can be calculated by taking the derivative of Eq. 3.2 with respect to the input power, P_{i}. This can be expressed as

$$\frac{dT}{dP_{\mathrm{i}}} = \frac{dT}{d\phi}\frac{d\phi}{dP_{\mathrm{r}}}\frac{dP_{\mathrm{r}}}{dP_{\mathrm{i}}}, \tag{3.3}$$

where, P_{r} is the power circulating inside the microring. The first term on the right-hand side of Eq. 3.3 represents the change in the device transmission due to resonance. This term is computed from Eq. 3.2 to give

$$\frac{dT}{d\phi} = \frac{2r^2\kappa^4 \sin\phi}{(1+r^4-2r^2\cos\phi)^2}. \tag{3.4}$$

To maximize the switching enhancement, we choose to operate the device where the transmittance has a maximum slope. It can be shown that this point occurs at ϕ_{max} just off the resonance phase, as shown in Fig. 3.2, with

$$\cos\phi_{\mathrm{max}} \approx 1 - \frac{\kappa^4}{6}, \qquad \text{for } \kappa \ll 1. \tag{3.5}$$

Substituting from Eq. 3.5 into Eq. 3.4 gives

$$\left.\frac{dT}{d\phi}\right|_{\phi_{\mathrm{max}}} \approx \frac{3\sqrt{3}}{8\kappa^2}. \tag{3.6}$$

The last term on the right-hand side of Eq. 3.3 represents the power enhancement factor in the microring resonator. Since the ratio of the circulating intensity in the microring to the input intensity is given by

$$\left|\frac{E_{\mathrm{r}}}{E_{\mathrm{i}}}\right|^2 = \frac{\kappa^2}{1+r^4-2r^2\cos\phi}, \tag{3.7}$$

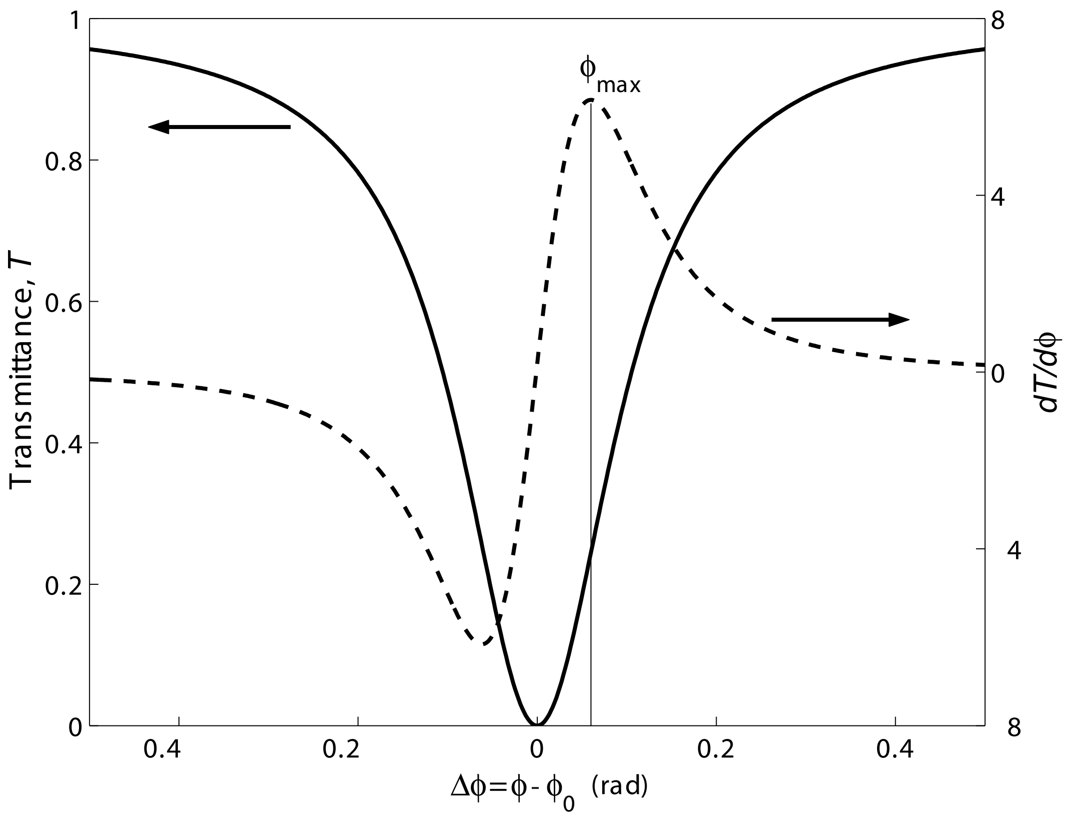

Figure 3.2: Throughput transmittance (solid line) versus phase detuning near resonance, for a microring notch filter with critical coupling and $\kappa^2 = 10\%$. The slop of the transmittance, $dT/d\phi$ (dashed line), shows that maximum switching enhancement is obtained at ϕ_{max} located just off resonance.

therefore at ϕ_{max} we obtain

$$\frac{dP_{\mathrm{r}}}{dP_{\mathrm{i}}} \approx \frac{3}{4\kappa^2}. \tag{3.8}$$

3.1.1 Nonlinear Kerr Effect

If the microring resonator guiding material posses a third order nonlinearity manifested as an intensity-dependent refractive index, then the material refractive index can be written as

$$n = n_0 + n_2 I_{\mathrm{r}}, \tag{3.9}$$

where n_0 is the linear refractive index, n_2 is the nonlinear refractive index coefficient, and I_{r} is the resonant field intensity. As a result, the round trip phase shift can be written as

$$\phi = \phi_0 + \frac{2\pi L n_2}{\lambda A_{\mathrm{eff}}} P_{\mathrm{r}}, \tag{3.10}$$

where ϕ_0 is the linear phase term, L is the circumference of the microring, λ is the wavelength of the input light, and A_{eff} is the effective mode area of the microring waveguide. Thus

$$\frac{d\phi}{dP_{\mathrm{r}}} = \frac{2\pi L n_2}{\lambda A_{\mathrm{eff}}}. \tag{3.11}$$

Substituting from Eqs. 3.6, 3.8 and 3.11 into Eq. 3.3, we obtain the switching threshold of the microring resonator

$$\left.\frac{dT}{dP_{\mathrm{i}}}\right|_{\phi_{\mathrm{max}}} \approx \frac{9\sqrt{3}}{16} \frac{\pi n_2 L}{\lambda A_{\mathrm{eff}}} \frac{1}{\kappa^4}. \tag{3.12}$$

Since the field enhancement, FE, of the resonator is inversely proportional to the coupling coefficient κ, then

$$\left.\frac{dT}{dP_{\mathrm{i}}}\right|_{\phi_{\mathrm{max}}} \propto (\mathrm{FE})^4. \tag{3.13}$$

Therefore, the effect of the resonator is to introduce two separate enhancements. One is due to operating near resonance where the slope of the transmittance is maximum. The other is due to the field enhancement inside the microring. The combined effect is to enhance the nonlinear response by the fourth power of the FE.

3.1.2 Two-Photon Absorption

When pumping the microring with photons that have energy above half the bandgap energy of the materials, TPA takes place and can dominate over the nonlinear ultrafast Kerr effect. The free carrier generation inside the resonator by such process is given by

$$\frac{dN_{\mathrm{c}}(t)}{dt} = \frac{\alpha_2}{2\hbar\omega} I_{\mathrm{r}}^2 - \frac{N_{\mathrm{c}}}{\tau_{\mathrm{c}}}, \tag{3.14}$$

where N_{c} is the generated free carrier density, α_2 is the TPA coefficient, ω is the input light frequency, I_{r} is light intensity, and τ_{c} is the free carrier life time. For a pump pulse of pulse width Δt that is shorter than the carrier lifetime τ_{c}, Eq. 3.14 can be approximated as

$$\Delta N_{\mathrm{c}} \approx \frac{\alpha_2 \Delta t}{2\hbar\omega} I_{\mathrm{r}}^2. \tag{3.15}$$

These free carriers generated by TPA change the refractive index of the microring resonator according to

$$\Delta n = -\sigma_{\mathrm{r}} \Delta N_{\mathrm{c}}, \tag{3.16}$$

where σ_r is the refractive volume of the material. Substituting from Eq. 3.15 into Eq. 3.16, we obtain

$$\Delta n \approx -\frac{\sigma_r \alpha_2 \Delta t}{2\hbar\omega} I_r^2. \tag{3.17}$$

Unlike the linear intensity dependence of the Kerr effect, Eq. 3.17 shows that the nonlinear refractive index change due to TPA has a quadratic dependence on the pump intensity. Therefore, TPA dominates over Kerr effect for pump intensities higher than the crossing point between the linear and the quadratic dependence. In such a case, TPA has to be taken into consideration. The phase change inside a microring resonator due to the contribution of the free carriers generated by TPA is thus given by

$$\Delta\phi \approx -\frac{\pi L}{\lambda} \frac{\sigma_r \alpha_2 \Delta t}{\hbar\omega} I_r^2, \tag{3.18}$$

and hence

$$\frac{d\phi}{dP_r} \approx -\frac{2\pi L}{\lambda A_{\text{eff}}^2} \frac{\sigma_r \alpha_2 \Delta t}{\hbar\omega} P_r. \tag{3.19}$$

By substituting from Eqs. 3.19, 3.6, and 3.8 into Eq. 3.3, we obtain the magnitude of the switching threshold to be

$$\left|\frac{dT}{dP_i}\right|_{\phi_{\max}} \approx K \frac{1}{\kappa^6}, \tag{3.20}$$

where

$$K = \frac{27\sqrt{3}}{64} \frac{\pi L \sigma_r \alpha_2 \Delta t}{\lambda A_{\text{eff}}^2 \hbar\omega} P_i. \tag{3.21}$$

Rewriting Eq. 3.20 as a function of the resonator FE, we obtain

$$\left|\frac{dT}{dP_i}\right|_{\phi_{\max}} \propto (\text{FE})^6. \tag{3.22}$$

Therefore, an enhancement of the sixth power of the cavity FE is obtained when TPA is the nonlinear process involved. In doing the above analysis, we have ignored any contribution of the Kerr effect. Also, we have assumed that the resonator round trip loss is constant and ignored any nonlinear loss contribution. If the nonlinear loss is significant, then the round trip loss will change dynamically and the critical coupling condition will be broken, degrading the switching enhancement.

3.2 Discussion

After we have considered and studied the nonlinear enhancement offered by the microring resonator using small-signal analysis, here we discuss the limitations of such analysis. We assumed that a small range of detuning is considered which is not practical for all-optical switching purposes where at least 10 dB switching contrast is required. Such contrast is only achievable by detuning the microring resonance by at least the resonance 3-dB bandwidth. Therefore, the assumption that we are operating at the transmission maximum slop point, ϕ_{max} shown earlier in Fig. 3.2, is not always valid. In addition, the field resonating inside the resonator is dynamically changing as the microring resonance is detuning across a certain input signal wavelength. The same is valid for the resonator FE. In Fig. 3.3, we plot the dynamic FE (solid line) versus the input power, for a critically coupled microring resonator notch filter that has a radius of 10 μm, $\kappa^2 = 10\%$, and a nonlinear Kerr index $n_2 = 10^{-17}$ m^2/W. As the input power increases, the nonlinear refractive index change detunes the microring resonance away

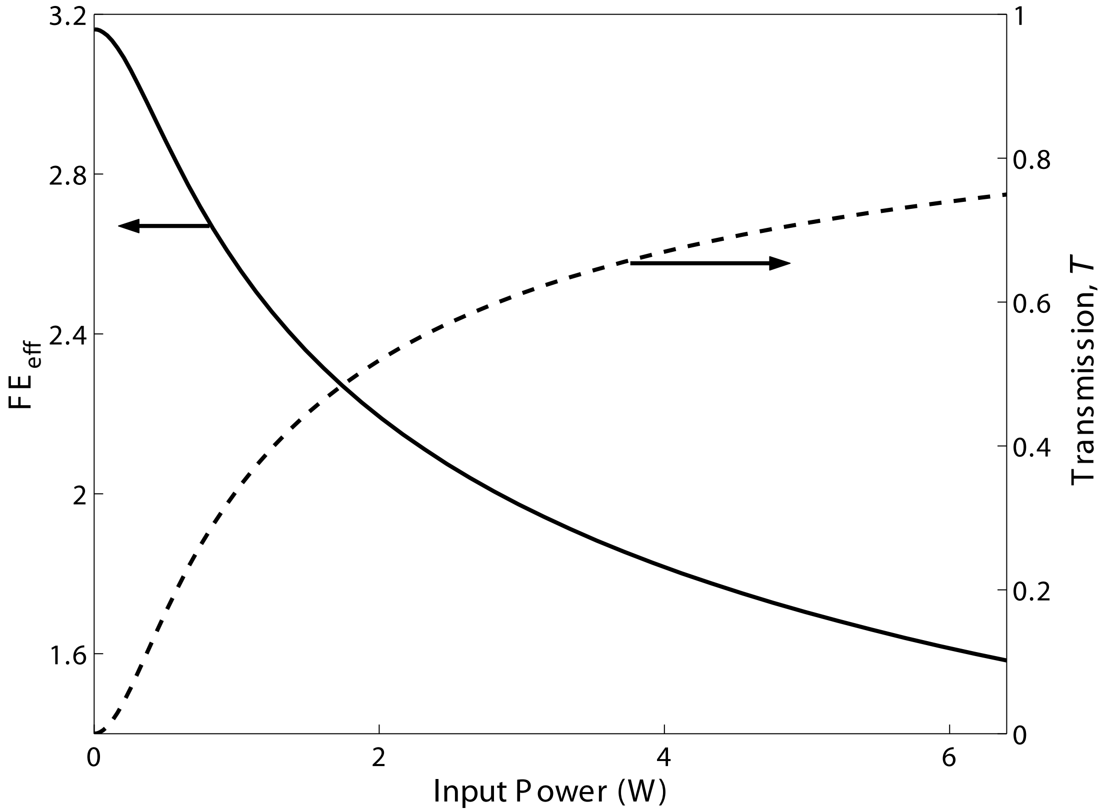

Figure 3.3: Dynamic FE and transmission of a microring resonator when a pump beam is tuned to its resonance.

from the input signal, and hence the FE decreases. On the other side, the resonator transmission (dotted line) increases. This situation resembles shooting a moving target. There are two possible solutions to overcome the moving resonance problem. The first one is to detune the input pump wavelength to track the moving resonance dynamically in the same way a moving target can be shot. In a real system, this is not practical. The other solution is to make the target wider in spectrum so that it can be hit more easily. For instance, the resonance can be designed to have a box shape where it has a flat top and higher roll off sides on the drop output and flat notch bottom on the throughput output. Even so the resonance can be detuned by the input pump signal, the pump signal is still in resonance because of the box like shape of the resonance. Such box like resonance shape has been proposed and demonstrated using higher order microring resonator filters, in which more than one microring are cascaded either in parallel or in series [41–46]. In [47], a notch was added inside the resonator to have a clockwise and counter clockwise propagation in the resonator and therefore a second order filter was proposed.

CHAPTER 4

FABRICATION OF SEMICONDUCTOR MICRORING RESONATORS

In this chapter I will review the fabrication processes and steps that have been used to fabricate the optical semiconductor microring resonators. These devices have been fabricated in GaAs and InP material systems and have been used in the experimental work demonstrated in this thesis. The fabrication process of the laterally coupled InP devices has been developed by R. Grover and the fabrication process for the vertically coupled GaAs devices has been developed by P. Absil and J. Hryniewicz. V. Van, R. Grover, K. Amarnath and L.-C. Kuo have assisted me through the various stages of fabricating my own devices.

4.1 Laterally Coupled InP-based Microring Resonators

In a laterally coupled scheme both the ring and the bus waveguides are in the same plane and therefore have the same guiding material. The epitaxial layer structure for the laterally coupled InP devices is shown in Fig. 4.1. The epilayer is grown by solid-source Molecular Beam Epitaxy (MBE) on an InP substrate. The core layer is made of

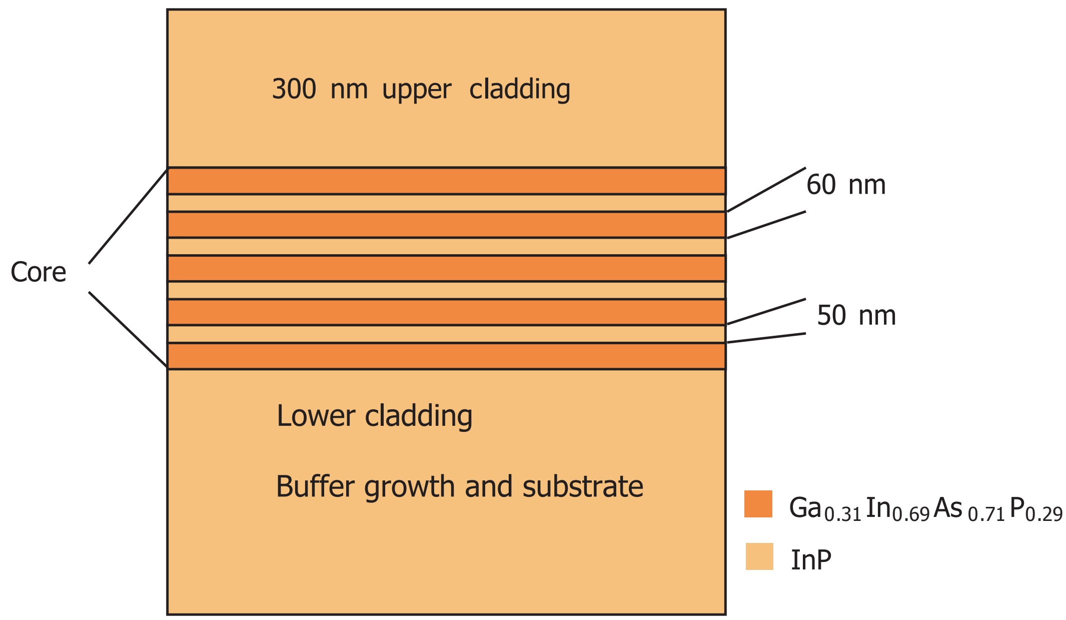

Figure 4.1: Schematic of the InP wafer layout showing the different layers thicknesses.

interlaced layers of InP and GaInAsP because we had difficulty growing thick layers of GaInAsP using the MBE. The fabrication steps are shown schematically in Fig. 4.2 and are summarized below [13].

4.1.1 Sample Preparation

The wafer is cleaved into 15×15 mm pieces. Each piece, called a "sample" hereafter, is processed one at a time. The sample is cleaned by solvent rinse in acetone, methanol, and isopropanol, successively. The sample is then dried using an N_2 air brush.

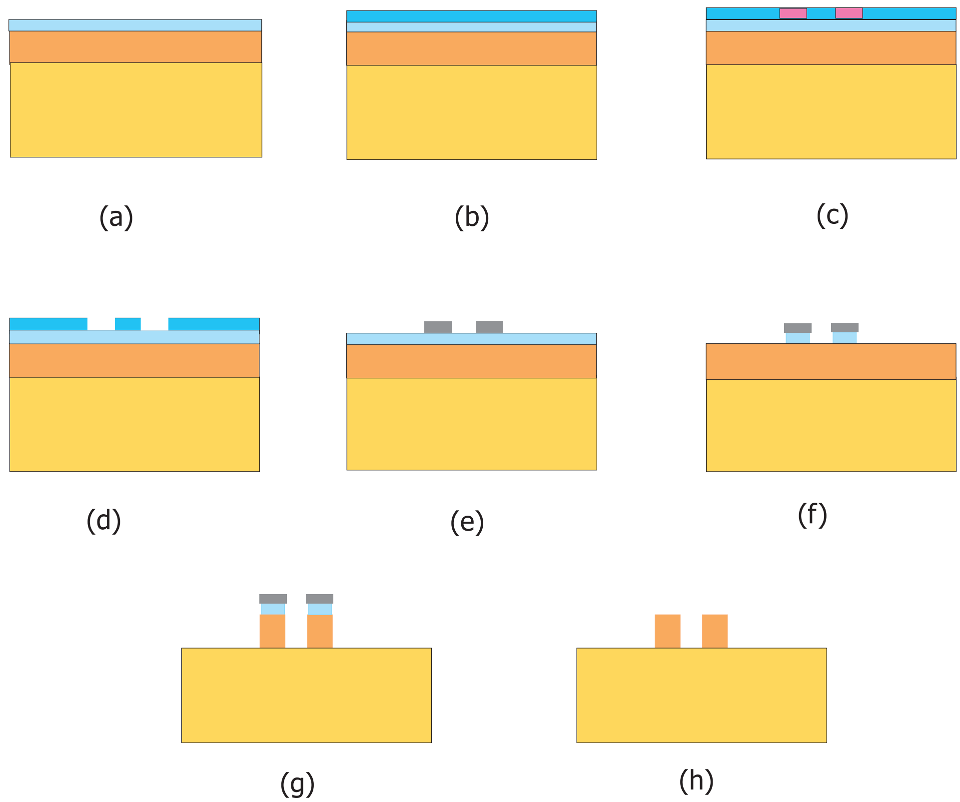

Figure 4.2: Schematic diagrams showing the fabrication steps for a laterally coupled InP microring resonator: (a) deposition of SiO_2, (b) spin of PMMA photoresist, (c) electron-beam lithography, (d) photoresist developing, (e) chromium deposition and lift off, (f) pattern is transferred to the SiO_2 layer, (g) pattern is transferred to the epilayer, and (h) the Cr-SiO_2 mask is removed by soaking in hydrofloric acid, which dissolves the SiO_2.

4.1.2 SiO_2 Deposition in PECVD Chamber

The sample is coated with 800 nm of SiO_2 using the Plasma Enhanced Chemical Vapor Deposition (PECVD) to serve as a hard mask to etch the epilayer (Fig. 4.2(a)).

4.1.3 PMMA Deposition

A PMMA bi-layer of total thickness of 300 nm is spun-on the sample, and pre baked at 170 ^{o}C for 15 minutes (Fig. 4.2(b)).

4.1.4 Electron-Beam Lithography

For lateral coupling, the gap between the ring waveguide and the bus waveguide has to be within 0.1 μm for proper coupling. Such high-resolution can be achieved by electron-beam lithography. This step was done at the Cornell Nano-Scale Facility, Ithaca, NY. The bus and microring waveguides pattern are exposed by direct write of the electron beam on the PMMA (Fig. 4.2(c)). After exposure, the photoresist is developed by soaking the sample into the developer solution. The microring and bus waveguides are the developed area of the photoresist (Fig. 4.2(d)).

4.1.5 Chromium Deposition and Lift off

Using the electron-beam evaporator, a 100 nm of Cr is deposited on the sample. Then, the sample is soaked in acetone for 30 minutes to lift off the unexposed PMMA with any Cr on top of it and leaving behind the developed PMMA pattern covered with Cr. The Cr pattern is used as a hard mask to etch the SiO_2 layer (Fig. 4.2(e)).

4.1.6 Mask Transfer to SiO_2

The Cr features are transferred to the SiO_2 layer by feature etch in the Reactive Ion Etching (RIE) chamber (Fig. 4.2(f)).

4.1.7 Mask Transfer to InP

Both Cr and SiO_2 are used to dry etch the InP epilayer in the RIE chamber (Fig. 4.2(g)).

4.1.8 Mask Removal

The sample is soaked in hydrofloric acid for 3 minutes to remove the SiO_2 mask together with the Cr mask on top of it (Fig. 4.2(h)).

A scanning electron micrograph (SEM) picture of a fabricated GaInAsP-InP add/drop microring resonator is shown in Fig. 4.3.

4.2 Vertically Coupled GaAs-based Microring Resonators

In the vertical coupling scheme, the coupling between the microring waveguide and the bus waveguide is in the vertical direction through an epitaxially-grown mid layer in contrast to the lateral scheme in which coupling is through an etched low refractive index gap [4, 11, 48]. Therefore, the vertically coupled microring guiding material can be different from that of the bus waveguide. As a result, active-passive integration is now feasible. For instance, the microring guiding material can be designed to have a bandgap close to the input light wavelength for higher nonlinearity or can be made of a

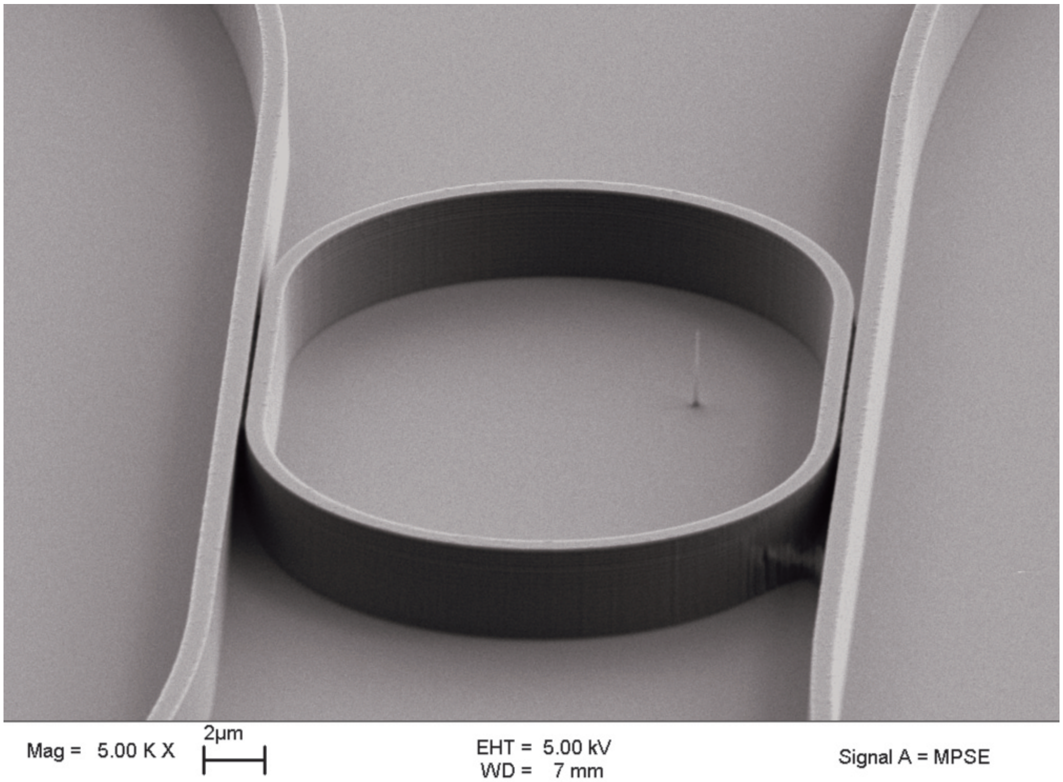

Figure 4.3: SEM picture of a GaInAsP-InP micro-racetrack resonator. The racetrack has a straight section length of 20 μm and a radius of 10 μm. The etch depth is 3.5 μm and the coupling gap is 100 nm. The microring and bus waveguides widths are 0.5 μm.

quantum well structure for active and tuning purposes while the bus guiding material can be designed to have a bandgap larger than the photon energy and therefore transparent to the input light. Moreover, the coupling gap no more has to be precisely controlled through the electron beam lithography since coupling is through a pre-grown mid layer. This allows the use of photolithography for exposing both the microring and the bus waveguide. Photolithography has the advantage of higher throughput yield in contrast

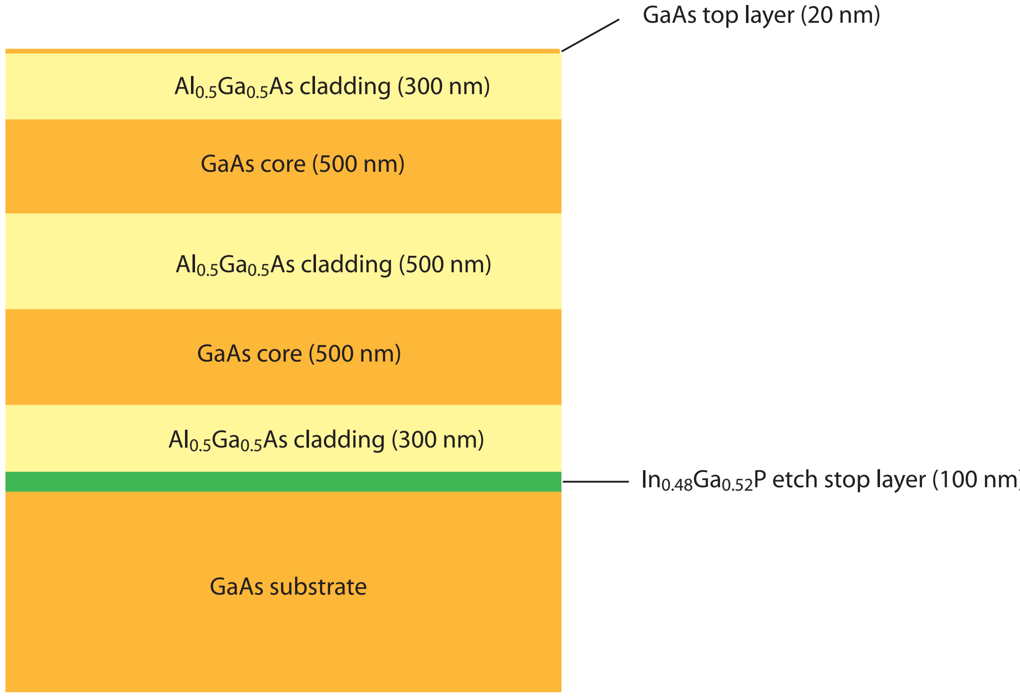

Figure 4.4: Schematic layout of the vertical coupling GaAs wafer showing the different layers thicknesses. The 20 nm top layer of GaAs prevents the AlGaAs cladding layer from being exposed to air and therefore not to be oxidized.

to the low throughput yield of the electron beam lithography. In addition, more complex structures, where two or more symmetric microrings are involved, can be fabricated. The layer structure for the vertically coupled GaAs-AlGaAs microring resonators is shown in Fig 4.4. The fabrication steps for this scheme are shown in Fig. 4.5 and are summarized as follows [49].

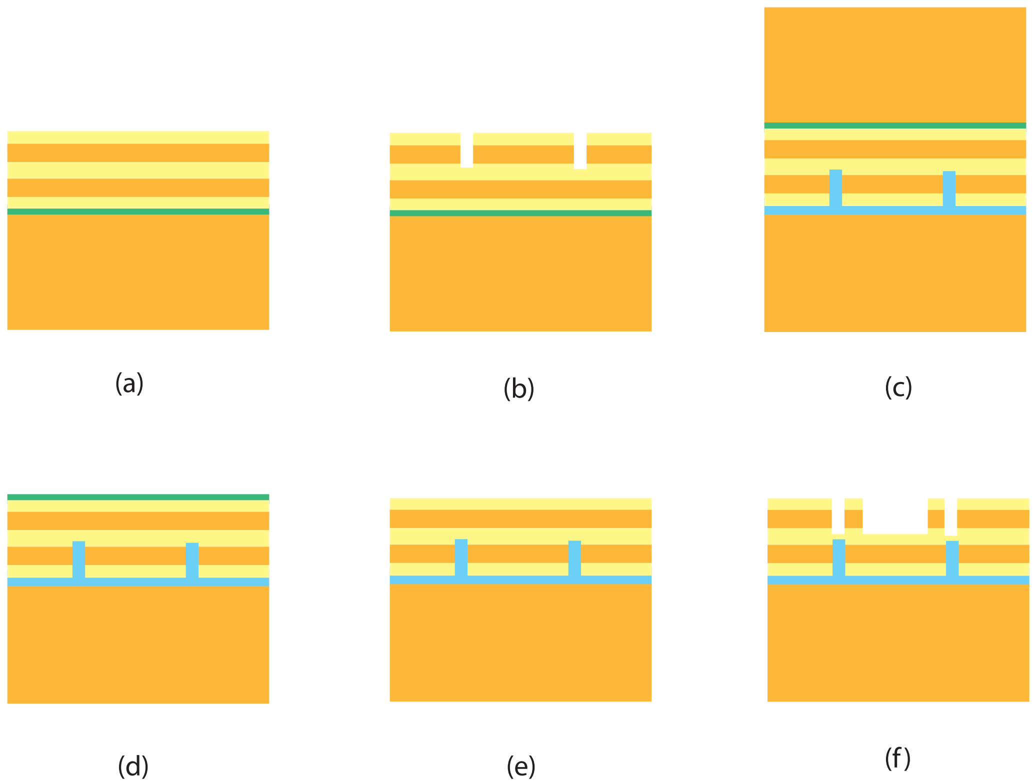

(a) (b) (c)

(d) (e) (f)

Figure 4.5: Schematic diagrams for the fabrication process steps of vertically coupled microring resonators: (a) sample cleaning, (b) microring level exposure and etch, (c) chip flip bonding using BCB, (d) substrate removal, (e) etch stop removal, and (f) bus waveguides exposure and etch.

4.2.1 Photolithography

Since there is no small gap needed, a 10 $\times$ i-line stepper is used to pattern the devices on photoresist. For each exposure level, an OIR 906-10 photoresist is spun on the sample for 1 minute at 3500 rpm (for a thickness of 1.1 μm) and pre baked at 90 ^{o}C for 1 minute. After exposure, the photoresist is post-baked at 120 ^{o}C, then soaked for 1 minute in the developer solution, OPD 4262, followed by rinsing in deionized water, and blow-dried with nitrogen.

4.2.2 Multilevel Alignment

To align the microring waveguide precisely with the bus waveguides, both the ring waveguide mask and the bus waveguide mask have alignment keys and Vernier marks. The alignment keys help in aligning the bus waveguide with respect to the microring waveguide. The Vernier marks help in measuring the misalignment error.

4.2.3 GaAs Feature Etch

First we expose the microring waveguide level using the appropriate mask together with the alignment keys and Vernier marks. Then the exposed photoresist is used as a soft mask to etch down the microring waveguide using the Inductively Coupled Plasma chamber (ICP) to achieve an etch depth of 950 nm. After that, the sample is soaked in acetone for 30 minutes to remove the soft mask. The sample is examined in the SEM to determine the etching quality and the side wall verticality.

4.2.4 Chip Flip-Bonding

A 15×15 mm^2 GaAs piece, back-side polished, is used as a transfer substrate or carrier. The carrier is cleaned and coated with adhesion promoter, AP 3000. The same promoter is used to coat the sample. The promoter helps the benzocyclobutene (BCB) that is used as a bonding material to stick well to both the carrier and the sample surfaces. A drop of BCB is placed on the new carrier and the sample is flipped with the epilayer facing downward and is placed on top of the carrier with rough alignment of the crystal axes of both pieces. The sample is pressed down gently on the carrier to remove any air bubbles that might have been trapped during the bonding step. After that, the sample is placed under an Infra Red (IR) transmission microscope with an IR lamp underneath the whole sample to examine for any air bubbles trapped in between the two samples before curing the BCB. If any bubbles are found, the BCB is dissolved and the bonding step is repeated. After that, the sample is placed in the furnace to cure the BCB, which bonds the sample to the transfer substrate.

4.2.5 GaAs Substrate Removal

The growth substrate is removed in 3 steps. The first step is a fast nonselective etch in which the 650 μm GaAs substrate is thinned chemically down to 150 μm. The second step is a slow but selective etch (GaAs over InGaP) that removes the remaining 150 μm GaAs substrate and is stopped by the 100 nm InGaP etch stop layer. The final step is a selective etch (InGaP over GaAs) that removes the etch stop layer. Once the etch stop layer has been removed, the epilayer transfer is complete, and the epilayer is ready for the next exposure level.

4.2.6 Clearing the Alignment Keys and the Vernier Marks

At this point, the total epilayer thickness is 2.1 μm and the alignment marks have only been etched down to 0.95 μm from top side. Before we proceed with the next level, we first clear the alignment marks from the bottom or flipped side of the epilayer. The sample is coated with a fresh photoresist and is exposed using a special mask with windows only on the alignments marks. After that, these exposed windows are etched down using the ICP until the Alignment and Vernier marks are clear and can be seen on the sample in the optical microscope. The unexposed photoresist is removed and the sample is coated with photoresist to expose the bus waveguide level. We then pattern the bus waveguides down to 950 nm. This leaves a mid layer of 200 nm between the ring and the bus waveguide that provides mechanical strength and enhances the coupling between the bus waveguide and the microring waveguide cores.

4.2.7 Sample Thinning and Cleaving

To obtain optical quality waveguide facets, the sample has to be cleaved properly. Therefore, the carrier substrate is chemically thinned down to 150 μm. The remaining thin substrate is easy to cleave while strong enough to be handled and mounted later. The cleaving process is initiated using a diamond tip scriber to scribe along the crystal axis of the substrate. The scribe marks are equally spaced by 500 μm to produce 500 μm bars.

The sample is cleaved by placing it on a razor blade aligned along the scribe marks. By pushing the sample down on the blade, the scribe mark propagates along the crystal axis. The cleaved bars are then mounted on 600 μm wide brass mounts using silver epoxy, and are ready for testing and handling.

4.3 Light Coupling

We use a special optical fiber to couple light to and from the device. The fiber we used has a conically shaped tip that acts as a lens to focus the single mode guided by the fiber core (typically 8 μm diameter) to a narrow beam waist at the waveguide input. The input and output fiber tips are aligned to the device input and output facets using two micro controlled stages. Each stage has a 3 axes of freedom (X, Y and Z) and 2 angular tilting knobs (Θ and Φ). An imaging system, consisting of a video camera, a light source and a magnifier, is used to roughly align the fiber tip to the center of the waveguide. A fine alignment is obtained by executing an automated 3-dimensional scan of the optical mode at the input and output facets and aligning the fiber tips to the peak of the Gaussian mode. This is very critical to aligning the input power to the device input waveguide. The use of the conically tipped fibers in combination with the micro controlled stages helped us to obtain a reasonable coupling efficiency and therefore succeed in investigating the nonlinear characteristics of microring resonators. In Fig. 4.6, we plot the X-Y scanned mode profile at the output of a single mode GaAs waveguide vertically coupled to a single microring resonator. The input light wavelength

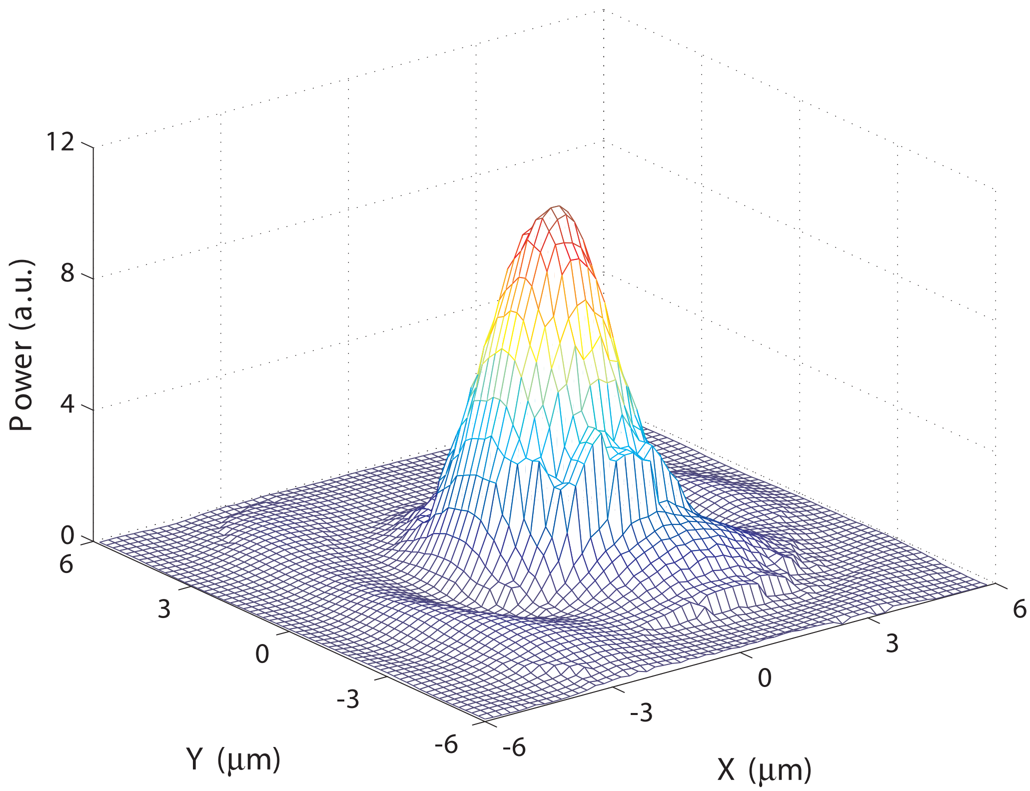

Figure 4.6: 3-dimensional plot of the measured Gaussian mode at the output of a single mode waveguide vertically coupled to a microring resonator. The input light wavelength is tuned away from the microring resonance. The waveguide width is parallel to the X-axis and the waveguide height is parallel to the Y-axis.

was tuned away from the microring resonance to obtain reasonable output power and to isolate the bus waveguide from the microring resonator. As can be seen in Fig. 4.6, the measured Gaussian mode of the waveguide is asymmetric towards the negative Y-axis. This asymmetry in the output mode can be explained by the asymmetry in the waveguide structure caused by the presence of the high refractive index 0.5 μm AlGaAs mid layer. This asymmetry also allows the electric field to be coupled between the bus waveguide and the microring waveguide.

4.4 Anti-Reflection Coating

A final step that enhances the performance and the coupling of light to the bus waveguide is the application of an anti-reflection (AR) coating on the bus waveguide facets. Semiconductors have refractive indices close to 3 and hence reflect light efficiently. This in return degrades the coupling efficiency of light to a semiconductor waveguide. Moreover, the cleaved facets of a straight waveguide act as a Fabry-Perot resonator and will have resonances with free spectral range determined by the length of the waveguide. Using the Fabry-Perot technique, the linear loss of the waveguide can be estimated from the spectrum of the uncoated bus waveguide [36].

In analogy with transmission line theory, the reflectance of the waveguide facet can be brought to zero by impedance matching [50]. This requires coating the waveguide facet with a material that has a refractive index, n, equal to the square root of the product of the refractive indices on both sides of the facet. Additionally, the thickness of the material has to be equal to odd multiple of $\lambda/(4n)$, where λ is the wavelength of the incident light. Therefore, for a GaAs waveguide, the coating material should have a refractive index of $\sqrt{1\times 3} = 1.73$. A 240 nm layer of aluminum oxide, Al_2O_3, is deposited on the facets of the devices using the electron-beam evaporator. The optical constants of the deposited Al_2O_3 layer are accurately measured using an ellipsometer. The refractive index of Al_2O_3 is measured to be 1.62.

In Fig. 4.7, we plot the spectrum of a vertically-coupled notch filter microring resonator before and after AR coating. From the uncoated device spectrum (Fig. 4.7(a)), we estimate the straight waveguide linear loss coefficient, α_0, to be 2 cm^{-1} and a power reflectivity of the uncoated facet of 25%. To determine the reflectivity of the AR coated facet, the spectrum of the device single-side AR coated is measured (Fig. 4.7(b)). The power reflectivity of the AR coated facet is estimated to be 2%. In Fig 4.7(c), we plot the throughput transmission of the device with both facets coated. As can be seen, the Fabry-Perot resonances have been almost eliminated and therefore the microring resonances are clear and linear parameters of the microring can be determined precisely.

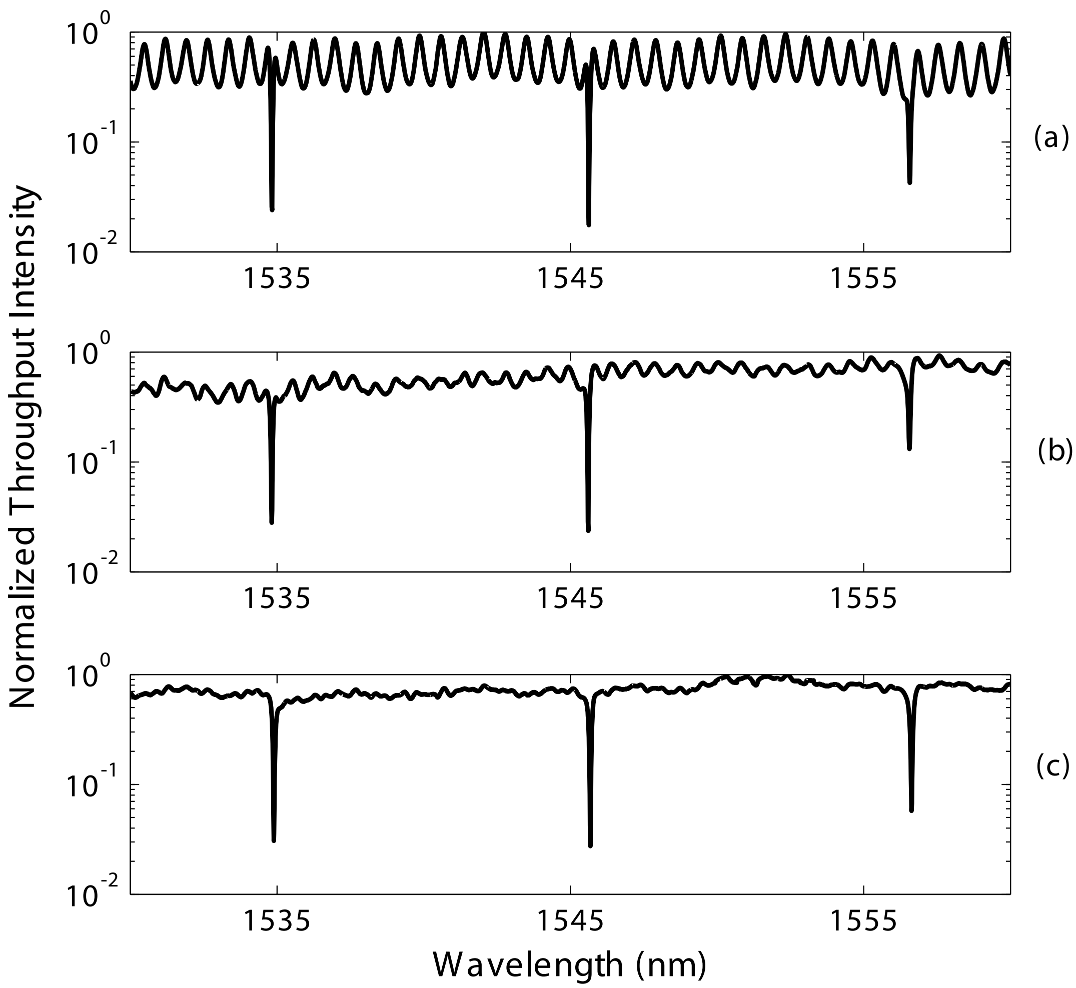

Figure 4.7: Normalized throughput transmission of a vertically coupled GaAs microring resonator notch-filter with the bus waveguide facets: (a) uncoated, (b) single-side AR coated, and (c) both sides AR coated.

CHAPTER 5

ALL-OPTICAL SIGNAL PROCESSING USING SEMICONDUCTOR MICRORING RESONATORS

In this chapter I will demonstrate all-optical switching, pulse reshaping, time division multiplexing/demultiplexing, and spatial pulse routing using GaAs-AlGaAs microring resonators. As we discussed earlier, the transmittance of a microring coupled to a single optical bus waveguide (Fig. 5.1) is determined by the interference between the bypass wave and the wave extracted from the ring. This transmittance can be altered by changing either the absorption or the refractive index of the ring, or both. For the GaAs-AlGaAs microrings operated at the 1.55 μm wavelength, the absorption and index changes can be accomplished via two-photon absorption (TPA) of a high-intensity pump beam tuned to one of the microring resonance modes. The subsequently induced change in the transmittance is then used to switch a low-intensity probe beam tuned to the vicinity of a different resonance mode.

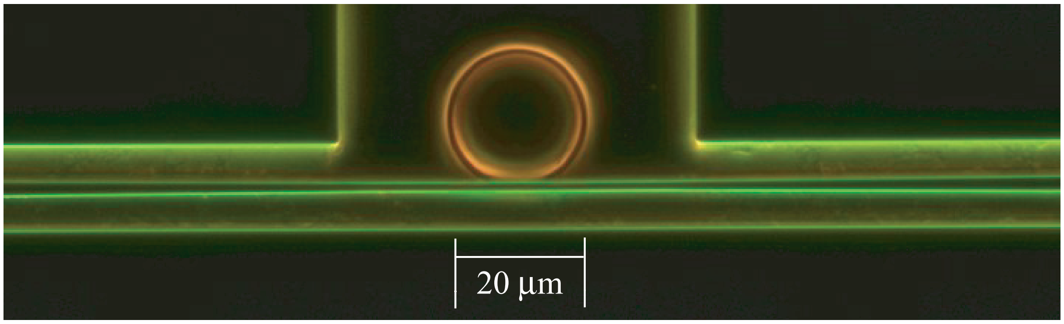

Figure 5.1: Optical micrograph of a vertically-coupled GaAs-AlGaAs microring resonator. The microring resonator appears with a different color than that of the bus waveguide because the picture is taken in the dark field and the microring is below the bus waveguide.

5.1 All-Optical Switching

5.1.1 Theory

The interaction between the pump and probe beams as they circulate in the ring can be described by a set of coupled nonlinear propagation equations using the slow envelope approximation. Let $A_{\mathrm{r}}(z,t)$ and $B_{\mathrm{r}}(z,t)$ represent the field envelope of the pump and probe signals, respectively, in the ring and designate z as the linear coordinate along the ring path. Assuming $|B_{\mathrm{r}}| \ll |A_{\mathrm{r}}|$, the propagation of the pump and probe beams in the presence of TPA-induced nonlinearity is given by

$$\begin{aligned} \frac{dA_{\mathrm{r}}}{dz} + \frac{n_0}{c}\frac{dA_{\mathrm{r}}}{dt} &= -\alpha_0 A_{\mathrm{r}} - (\alpha_2 + jn_2k_0)I_{\mathrm{p}}A_{\mathrm{r}} - (\Delta\alpha_{\mathrm{fc}} + j\Delta n_{\mathrm{fc}}k_0)A_{\mathrm{r}}, \\ \frac{dB_{\mathrm{r}}}{dz} + \frac{n_0}{c}\frac{dB_{\mathrm{r}}}{dt} &= -\alpha_0 B_{\mathrm{r}} - (\alpha_2 + jn_2k_0)I_{\mathrm{p}}B_{\mathrm{r}} - (\Delta\alpha_{\mathrm{fc}} + j\Delta n_{\mathrm{fc}}k_0)A_{\mathrm{r}}. \end{aligned} \tag{5.1}$$

In the above, $I_{\mathrm{p}} \propto |A_{\mathrm{r}}|^2$ is the pump beam intensity, n_0 is the waveguide effective index, α_0 is the linear absorption coefficient, α_2 and n_2 are the nonlinear TPA loss and refraction coefficients, respectively, and $\Delta\alpha_{\mathrm{fc}}$ and Δn_{fc} are the changes in the absorption and refractive index induced by free carriers generated from the TPA process. The contributions $\Delta\alpha_{\mathrm{fc}}$ and Δn_{fc} are proportional to the free-carrier density, N_{fc}, via $\Delta\alpha_{\mathrm{fc}} = \sigma_{\mathrm{a}} N_{\mathrm{fc}}$ and $\Delta n_{\mathrm{fc}} = \sigma_{\mathrm{r}} N_{\mathrm{fc}}$, with σ_{a} and σ_{r} being the absorption cross section and refraction volume, respectively. The free-carrier density generated by TPA evolves according to

$$\frac{dN_{\mathrm{fc}}}{dt} = \frac{\alpha_2}{2\hbar\omega} I_{\mathrm{p}}^2 - \frac{N_{\mathrm{fc}}}{\tau_{\mathrm{fc}}}, \tag{5.2}$$

where τ_{fc} is the carrier relaxation time. Coupling between the input pump, $A_{\mathrm{i}}(t)$, the output pump, $A_{\mathrm{o}}(t)$, and circulating pump beam $A_{\mathrm{r}}(z,t)$ in the ring is described by the set of equations,

$$\begin{aligned} A_{\mathrm{o}}(t) &= r A_{\mathrm{i}}(t) - j\kappa A_{\mathrm{r}}(t-\tau) e^{j\phi}, \\ A_{\mathrm{r}}(t) &= r A_{\mathrm{r}}(t-\tau) e^{j\phi} - j\kappa A_{\mathrm{i}}(t), \end{aligned} \tag{5.3}$$

where κ^2 is the coupling coefficient, $r^2 = 1 - \kappa^2$, τ is the round-trip time, and ϕ is the round-trip phase. A similar relationship exists for the probe signals $B_{\mathrm{i}}(t)$, $B_{\mathrm{o}}(t)$, and $B_{\mathrm{r}}(t)$. Eqns. 5.1, 5.2, and 5.3 are time-difference equations which are numerically integrated to simulate the passage of the pump and probe beams through the microring resonator. In chapter 3, steady-state analysis for the case where the pump pulse is much longer than the cavity lifetime revealed a reduction in the switching threshold proportional to the sixth power of the field enhancement, FE.

5.1.2 Device Characteristics

The microrings used in our experiment consisted of a 10 μm-radius GaAs/AlGaAs ring vertically coupled to a straight waveguide bus, as shown in Fig. 5.1. The wave-guiding structure has high lateral index contrast (3.37:1.5) to minimize the bending loss. A high-index, epitaxially-grown AlGaAs mid-layer allows for efficient coupling between the ring and bus waveguides. Fig. 5.2 shows the measured spectral response of the micro-resonator at the 1562 nm resonance and the theoretical fit. At resonance, near critical coupling causes a deep extinction of 8.5 dB in the signal. Assuming negligible propagation loss in the bus waveguide, a coupling coefficient of 3% and a round-trip power loss of 6% were obtained for the microring, giving a 3-dB bandwidth of 0.16 nm and a quality factor of 9800. The finesse of the device as determined from the measured 3-dB bandwidth and free spectral range was 68. The device has a computed field enhancement factor of 3.7 and a cavity lifetime of 42 ps.

5.1.3 Simulation Results

We first simulated the nonlinear propagation of a 300 ps pump pulse through the microring. The wavelength of the pulse was set at 1561.97 nm, which is 0.1 nm blue detuned with respect to the cavity resonance mode at 1562.07 nm. The parameters used in the simulation are $\alpha_0 = 10.2$ cm^{-1}, $\alpha_2 = 24$ cm/GW, $n_2 = 1.5 \times 10^{-13}$ cm^2/W, $\sigma_a = 1.5 \times 10^{-16}$ cm^2, $\sigma_r = 10^{-20}$ cm^3 and $\tau_{fc} = 50$ ps. The free carrier life time, τ_{fc}, was an adjusted parameter in our simulations to fit measured transient responses.

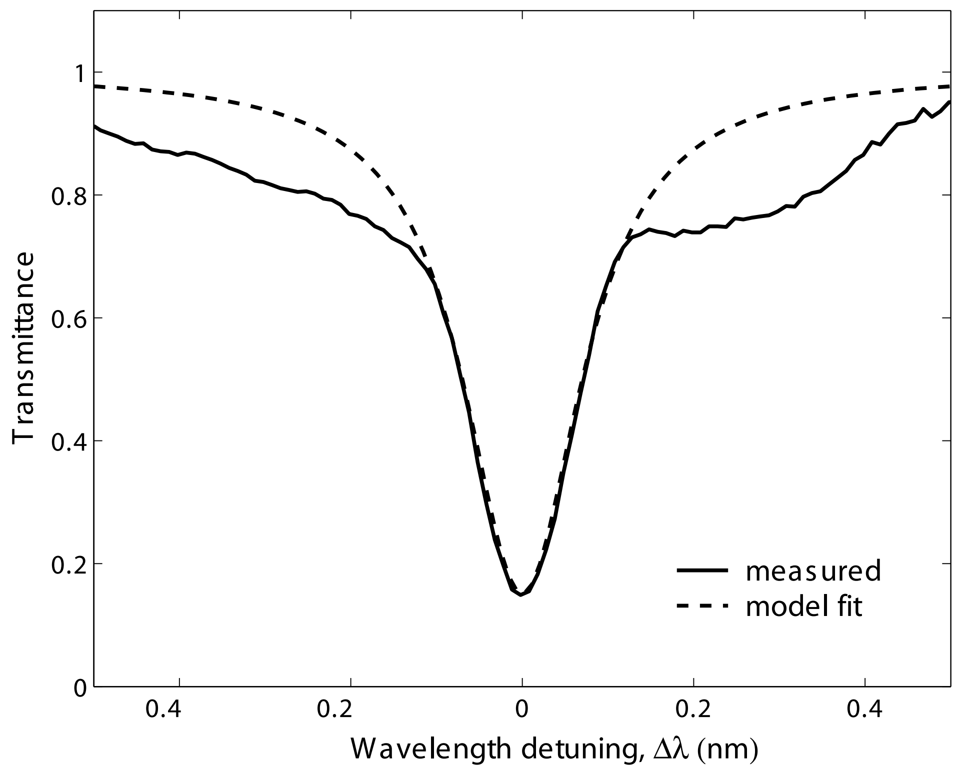

Figure 5.2: Measured spectral response and its theoretical fit for a 10 μm-radius GaAs-AlGaAs microring resonator at the 1562 nm resonance. The discrepancy between measurement and model on both sides of the resonance peak is due to the Fabry-Perot modulations in the bus waveguide.

Fig. 5.3 shows the evolution of the normalized pump intensity, I_p, inside the microring and the output pump intensity. The circulating pump intensity in the ring is normalized to its peak value, and is actually 12 times higher than the peak input intensity, due to field enhancement effect in the resonator. As can be seen in Fig. 5.3, the circulating pump intensity is lagging the input pump intensity by approximately the cavity charging time. It is also observed that as the field in the ring charges up, carriers generated from TPA cause a net decrease in the refractive index of about 2×10^{-4}, which has the effect of shifting the resonance mode toward shorter wavelengths by nearly 0.1 nm. Consequently, the output pump is observed to initially rise with the field in the ring, but then dip to a minimum as the microring resonance is pulled closer to the pulse wavelength. We note that this dip exactly coincides with the peak of the pump intensity in the ring. At the falling edge of the input pulse, the field in the ring begins to discharge, and the output pump intensity is seen to rise again as the cavity resonance mode returns to its initial position.

Next, we launched into the microring a low-intensity CW probe signal tuned to the resonance mode at 1550.92 nm. By tuning the probe beam with respect to the resonance and looking at the transmitted probe, one can determine how much refractive index change is obtained and which direction the resonance wavelength is shifted. This is demonstrated in the 3-dimensional plot shown in Fig. 5.4. When the probe beam is tuned to 1550.6 nm, far from resonance, it is totally transmitted to the throughput port or in the “ON” state. As the probe beam is tuned closer to resonance, the probe experience an increased attenuation as the pump pulse causes the resonance modes of the microring

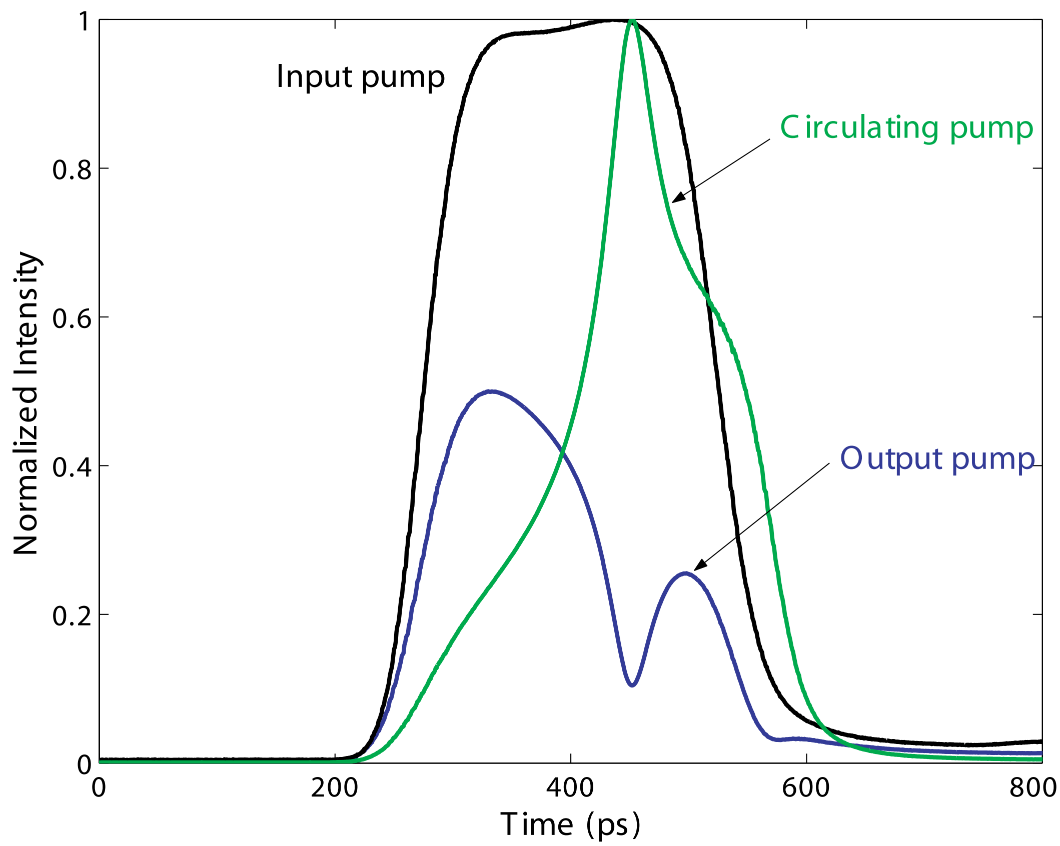

Figure 5.3: Simulated nonlinear propagation of a 300-ps pump pulse through a 10 μm-radius GaAs-AlGaAs microring resonator. The output intensity is normalized with respect to the peak input intensity. The pump intensity circulating inside the resonator is normalized with respect to its peak value, which is 12 times higher than the peak intensity of the input pump. The input pump is a real experimental pulse captured by the oscilloscope to be used in the simulation.

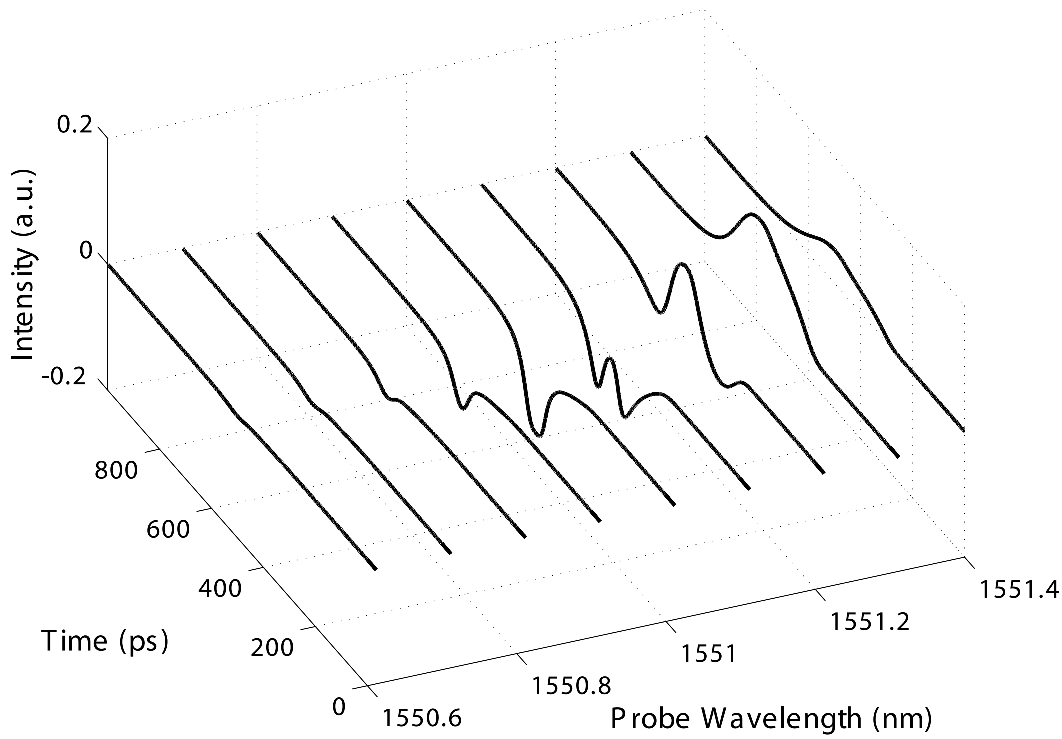

Figure 5.4: 3-dimensional plot of the simulation results for the throughput probe intensity versus wavelength and time. The DC level has been removed for clarity.

to shift to shorter wavelengths, thus effectively pulling the probe beam into resonance. When the probe wavelength is tuned to resonance at 1550.92 nm and prior to the arrival of the pump pulse, the transmitted probe signal is strongly attenuated. When the pump pulse arrives, it shifts the resonance away from the probe beam and as a result we see a rapid increase in the transmission of the probe signal as it switches on. We have removed the DC level from all time traces for clarity. In Fig. 5.5, we plot the input pump intensity and the switched probe for the two cases when the probe beam is initially

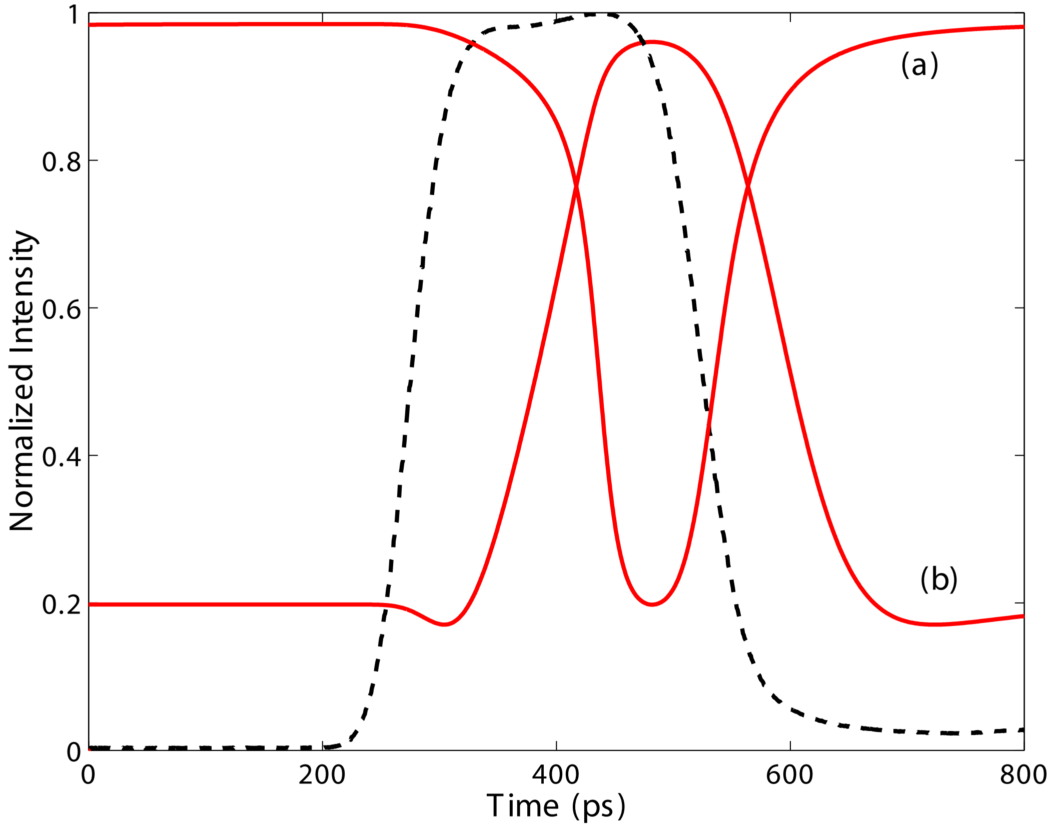

Figure 5.5: Simulated pump-probe interactions. (a) Probe beam initially off resonance. (b) Probe beam initially on resonance. The probe beam intensities are normalized with respect to the maximum transmittance at resonance.

blue-detuned off resonance at 1550.75 nm, and when it is initially tuned to resonance at 1550.92 nm. These represents the ideal scenarios for the “ON-OFF” and “OFF-ON” switching, respectively.

5.1.4 Experiment and Results

The experimental setup for the pump and probe experiment is shown in Fig. 5.6. An externally modulated laser diode is used to produce a 300 ps pump pulse signal with a 20 MHz repetition rate. The pump beam is then amplified using an Erbium Doped Fiber Amplifier (EDFA) to compensate for the external modulator and fiber to waveguide coupling losses. The average input power is 8 mW at the device input waveguide, giving an estimated peak intensity of 4.8 GW/cm^2 in the microring at resonance. The pump wavelength is set at 1562.0 nm, which is slightly blue-detuned from the resonance. A 3 mW CW probe signal tuned to the next higher resonance at 1550.9 nm is coupled to the pump beam via a 50/50 fiber coupler and fed to the device input using a conically tipped fiber to minimize the mode mismatch between the fiber and the waveguide. At the output the pump and probe signals are collected using another conically tipped fiber, optically amplified, then separated by a band-pass filter and detected using a 40 GHz detector and a 50 Ghz oscilloscope. In Fig 5.7, we plot a 3-dimensional graph for the measured throughput probe intensity as function of time and probe wavelength. It can be seen to be in very good agreement with the simulated 3-dimensional graph shown earlier in Fig. 5.4. Fig. 5.8 shows the time traces of the input pump, the output pump and the transmitted probe power for the switch-off and switch-on cases. The measured responses of both the pump and probe signals are seen to match with the simulated responses shown in earlier in Fig. 5.5. The pump pulse is strongly distorted and partially absorbed due to near critical coupling and TPA inside the microring resonator. The on

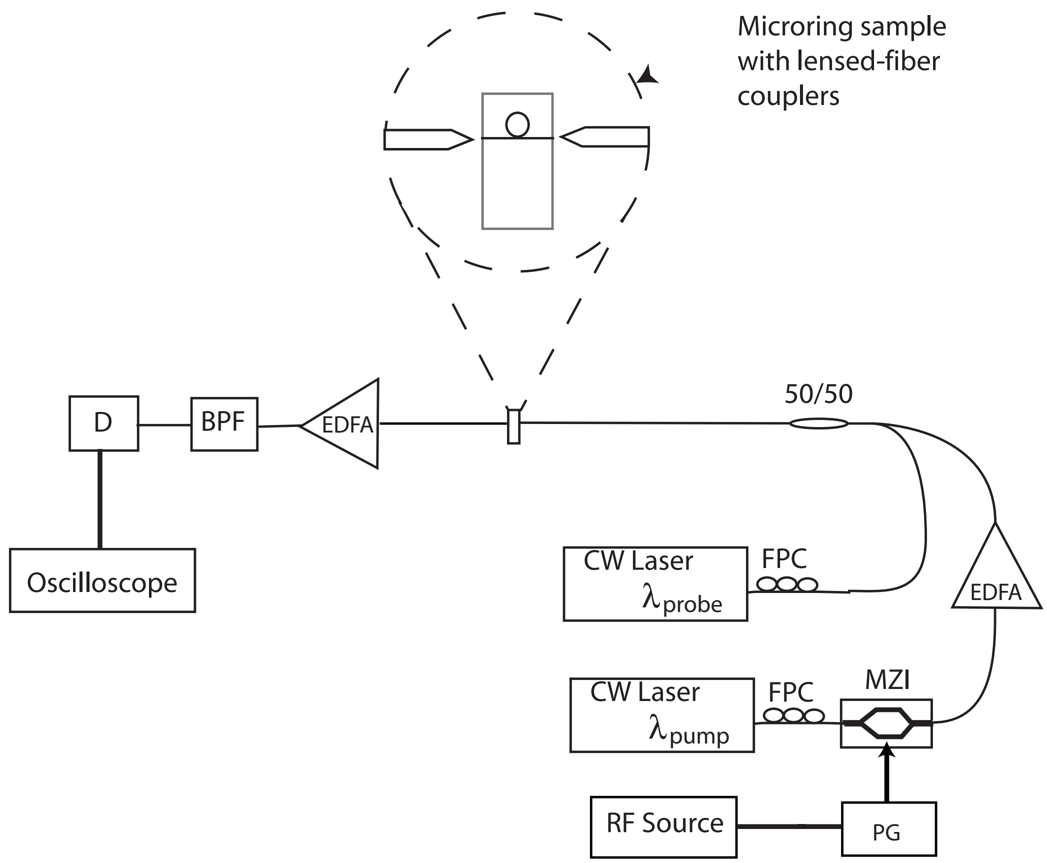

Figure 5.6: Experimental setup for the pump-probe technique to demonstrate all-optical switching using a 10 μm-radius GaAs-AlGaAs microring resonator. PG: pulse generator. FPC: fiber polarization controller. MZI: Mach-Zehnder interferometer. EDFA: Erbium doped fiber amplifier. D: detector. BPF: band pass filter.

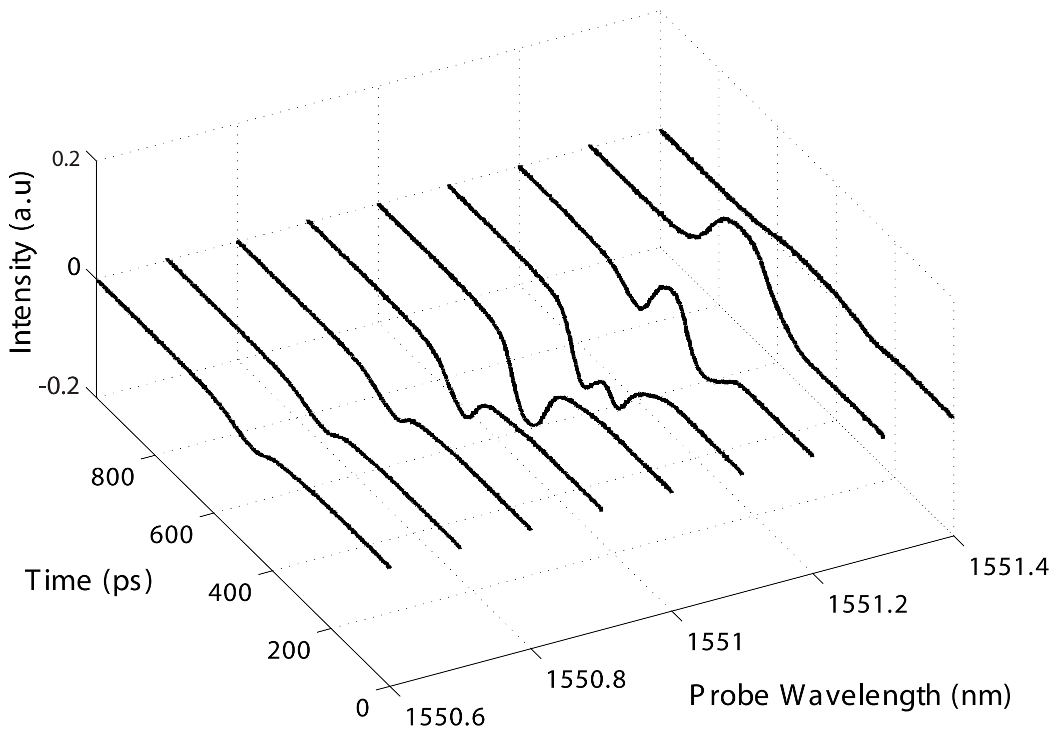

Figure 5.7: 3-dimensional plot of the measured throughput probe intensity versus wavelength and time. The DC level has been removed for clarity.

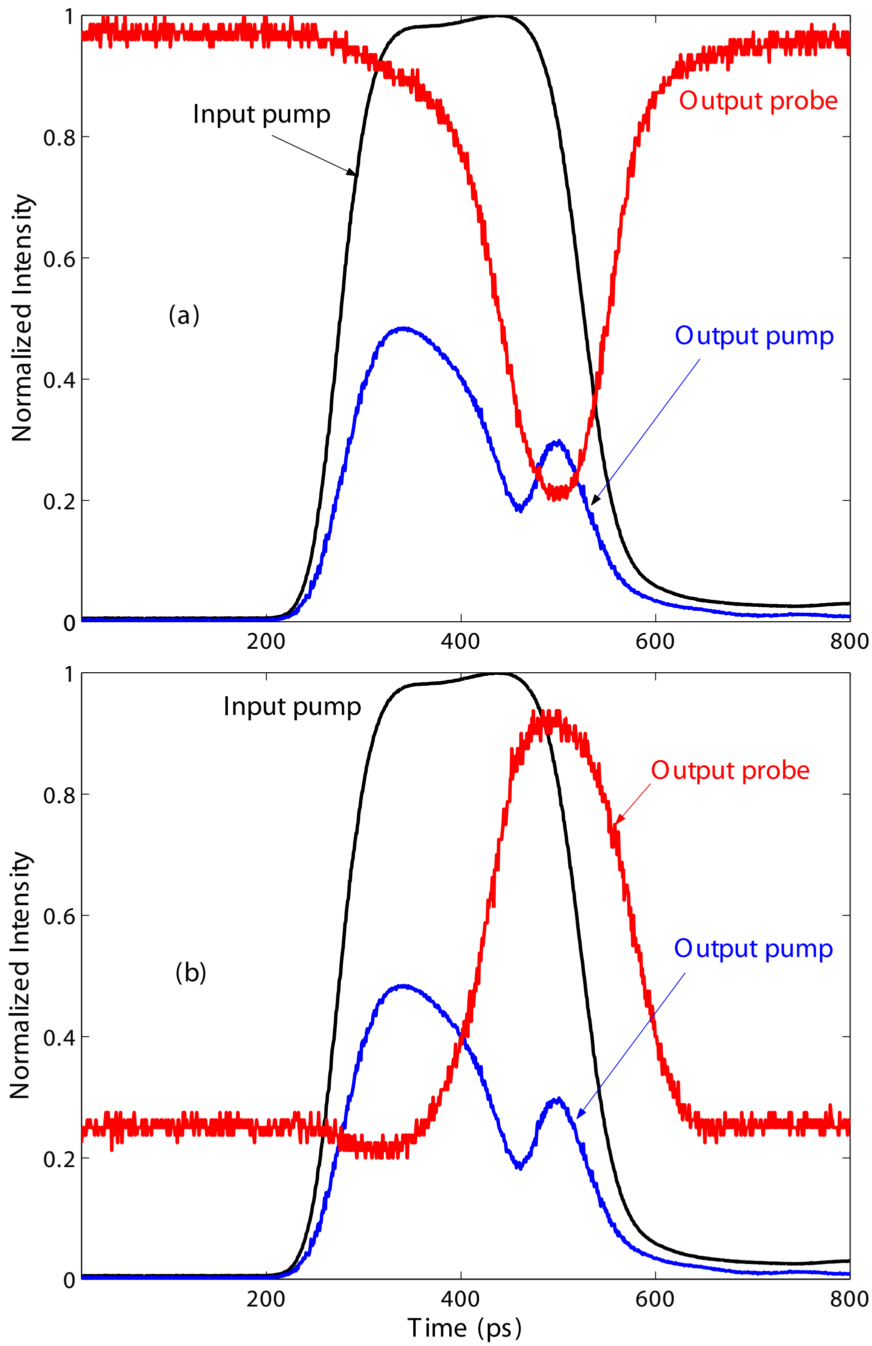

Figure 5.8: Measured time traces of the pump and probe beams intensities with (a) probe beam initially tuned off resonance (high transmission), and (b) probe beam initially tuned in resonance (low transmission).

and off switching times of the probe beam are slightly less than 100 ps. Also, it is observed that the probe beam quickly returns to the original state after the pump beam has passed. This fast recovery time, which is predicted by our simulation model to be in the order of 50 ps, is due to a large contribution from surface-state recombination at the microring waveguide sidewalls as we will discuss later.

5.2 Thresholding and Pulse Reshaping

The nonlinear transmission transfer function of a notch filter-based microring resonator can be used for thresholding. If an input signal is tuned exactly to a critically coupled microring resonance, it is initially absorbed by the resonator and there is no output signal transmitted. When the input signal intensity goes up, the self induced phase shift in the resonator results in a detuning in the microring resonance wavelength. If the detuning is large enough, the signal will be out of resonance and no longer absorbed by the microresonator. In return, the input signal is temporary out of resonance and totally transmitted to the output port. Such intensity-dependent nonlinear transmission function can be used for thresholding and pulse reshaping.

Fig 5.9 shows the output time trace of a GaAs-AlGaAs microring notch filter when excited by a 35 ps input pulse carrying approximately 50 pJ of energy and tuned exactly to the resonator resonance wavelength around 1550 nm. The input signal has a rise time of 40 ps, while the rise time of the output pulse was measured to be 20 ps. The output pulse is found to be delayed with respect to the input pulse by 25 ps which corresponds

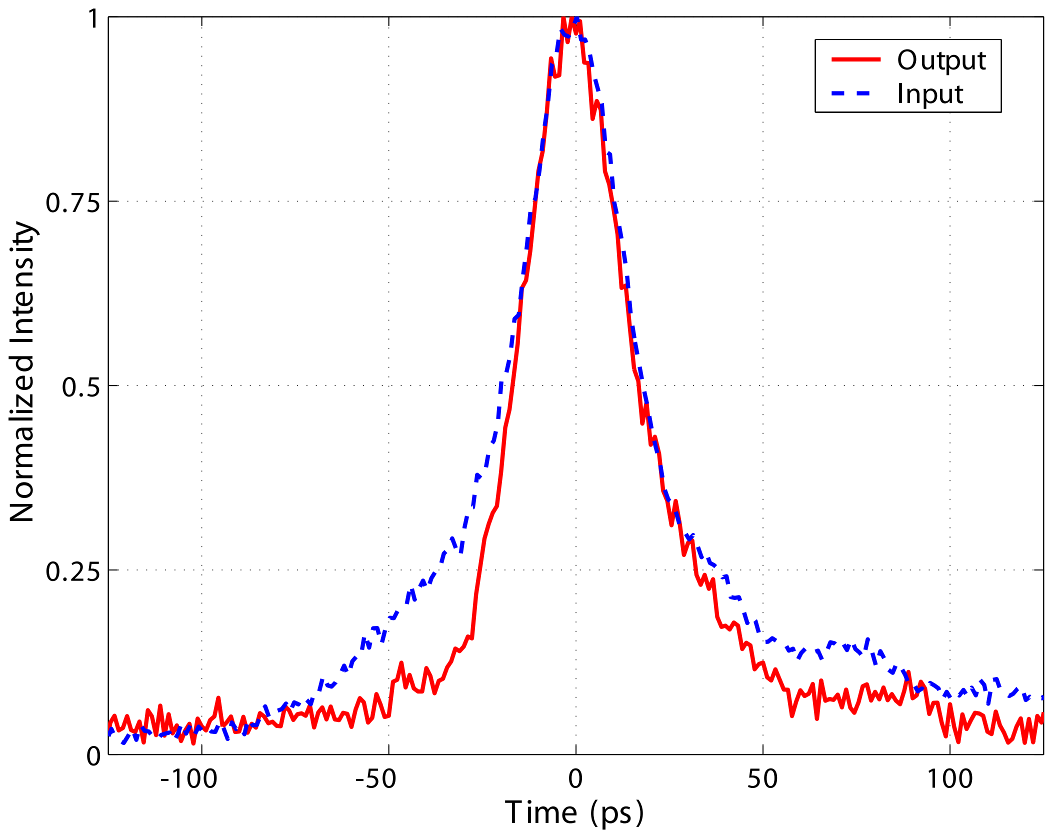

Figure 5.9: Time traces of the input and output pulses of a GaAs-AlGaAs microring resonator. Input and output intensities are normalized by their respective peak values. The output pulse has been shifted by 25 ps to overlap the input pulse to demonstrate the pulse reshaping.

to the charging time of the resonator. We have plotted both pulses on each others to show the reshaping feature attained by the resonator.

5.3 Simultaneous Time Division Demultiplexing and Spatial Pulse Routing

A routing switch connects the input port to one of several output ports and physically moves photons from one port to another. Routing can be based on either the intensity of the input signals or an external control beam. Typically, the control beam is in different physical format than the data. For example, the pump beam might have a different wavelength or polarization than the data beam. Nonlinear directional couplers [51], and distributed-feedback waveguides [52] are two examples of passive all-optical routing and demultiplexing switches.

When a microring resonator is used in the add-drop configuration (Fig. 5.10), a pump beam tuned to one of the resonator resonances can be used to spatially route an incoming signal, tuned to another resonance, to the through port or the drop port of the device depending on the presence or absence of the control beam [53]. If the incoming signal consists of a train of time multiplexed data channels, then the pump pulse can be applied at the appropriate time slot to pick out or demultiplex an individual data channel and route it to the drop port, while the remaining data channels are passed on via the through port for further demultiplexing using other microrings. The microring device in this case functions as an optical time-division demultiplexer. In a similar manner,

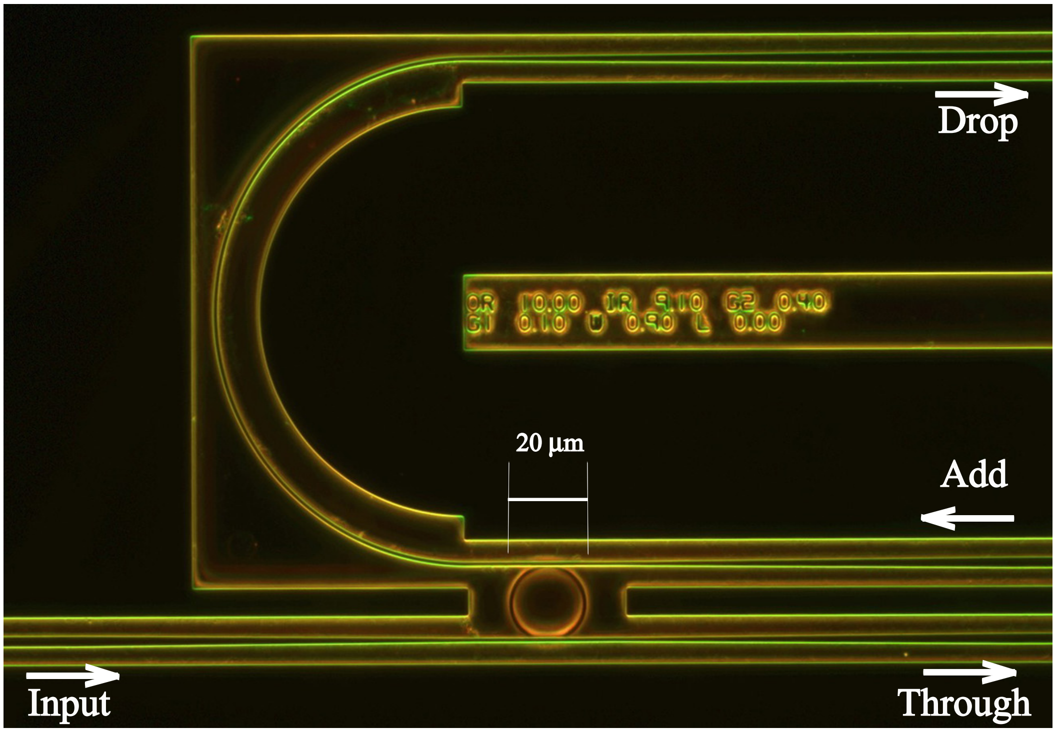

Figure 5.10: A dark field optical microscope picture of a vertically coupled GaAs OCDF microring resonator.

data pulses can also be multiplexed onto the incoming signal through the add port of the device.

5.3.1 Device Characteristics

The micro-resonator used in the experiment consists of a single 10 μm radius GaAs/AlGaAs microring vertically coupled to two straight waveguide buses as shown in Fig. 5.10. The wavelength spectrum of the throughput and drop ports are shown in Fig. 5.11. The resonator has a bandwidth of 0.22 nm, a finesse of 45, and a quality factor of 7000.

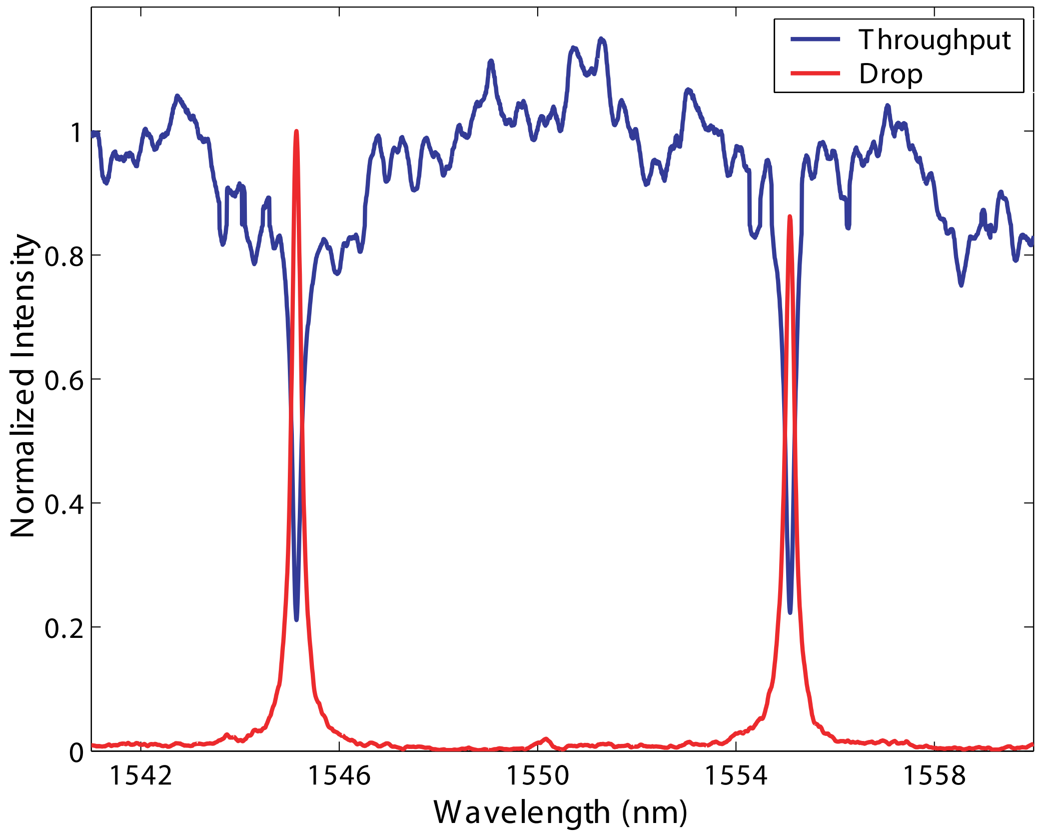

Figure 5.11: Normalized measured spectral response for the throughput and drop ports of the OCDF microring resonator.

5.3.2 Experiment

We first measured the response time of the microring as follows. A semiconductor CW source, tunable in the $1.5 - 1.6$ μm range, is used to provide a low-power (signal) beam with a typical coupled power of 1 mW at the device input. Another semiconductor laser diode is gain-switched at 8.5 GHz to produce 25 ps pulses and is fed to an external modulator to reduce the repetition rate to 125 MHz. It is then amplified by an EDFA to 10 mW average power. The CW signal (probe) beam is blue tuned to the microring resonance at 1555 nm while the control beam is tuned to the next higher microring resonance at 1544 nm. Wavelength tuning is achieved by both tuning the input laser sources wavelengths and by thermally tuning the microring resonator using a thermoelectric cooler. As we mentioned in chapter 2, the temperature sensitivity of the GaAs microring is measured to be 0.11 nm/^{o}C. The probe and pump beams are coupled together using a 10:90 fiber coupler and are fed to the device input waveguide using a conically tipped single mode fiber. The dropped and throughput beams are collected using conically tipped fibers, spectrally filtered from the pump beam using a band pass filter centered at the probe beam wavelength, and analyzed as functions of time using a 45 GHz detector and a 50 GHz digitizing oscilloscope. Therefore, our measurements are instrument limited.

Fig. 5.12 shows both the input pump pulse at 1545 nm and the output probe signal at the drop port when it is slightly blue tuned out of resonance at 1555 nm, thus initially not dropped. When the 25 ps pump beam comes in, it is partially absorbed by the ring material via TPA, and free carriers are generated causing a change in ring waveguide refractive index. This results in a shift in the microring resonances towards shorter wavelengths and thus the CW signal beam temporary becomes in resonance and becomes highly transmitted at the drop port. As can be seen in Fig. 5.12(b), the dropped signal exhibits a switching window of 30 ps demonstrating that the device is capable of switching data up to 33 Gb/s.

In the second part of our experiment we demonstrate the use of the OCDF micror-

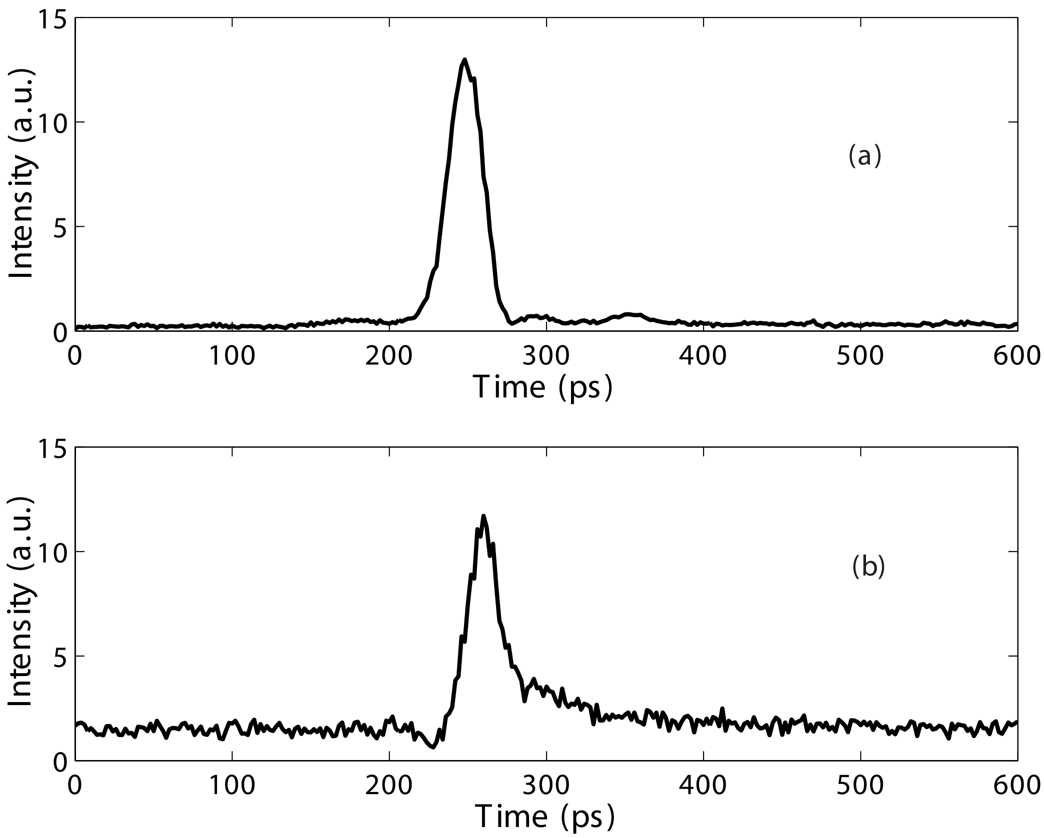

Figure 5.12: Time traces for: (a) the input pump pulse at 1545 nm, and (b) the output dropped signal when the input probe is initially blue tuned to the 1555 nm resonance.

ing resonator as a spatial pulse router to switch incoming data to either the drop port or the through port, depending on the presence or absence of a control pulse. The signal (probe) beam is a 5 GHz, 40 ps, RZ data stream, and blue tuned to the microring resonance at 1555 nm. For the control beam, an external modulator is used to chop a CW beam, which is tuned to the next microring resonance at 1544 nm. The pump pulse is a train of 150 ps at 80 MHz repetition rate. The data signals detected at the drop and through ports are shown in Fig. 5.13. It can be seen from the figure that the drop port signal is the demultiplexed data from the input data stream, while the remaining unswitched data are passed on to the through port where further demultiplexing can be performed using a series of microring resonators. The cross talk at the drop port was measured to be approximately 8 dB. This cross talk error is primarily due to the asymmetry between the input and output coupling coefficients, which arose from fabrication errors. The asymmetry in the coupling coefficients together with the loss inside the resonator are the reason for incomplete extinction at resonance for the throughput spectrum shown in Fig 5.11. Higher contrast and therefore less cross talk can be obtained by better matching of the input and output coupling coefficients and reducing the round trip loss as well, which will result in a critically coupled OCDF resonator. The pulse energy required for switching is approximately 50 pJ/pulse at the input of the waveguide. The actual energy coupled to the resonator is much less due to scattering and waveguide tapering losses. Engineering the material bandgap and increasing the resonator field enhancement will lower the switching power. The device can be also used in a similar manner to multiplex data onto the incoming data stream via the add port of the device.

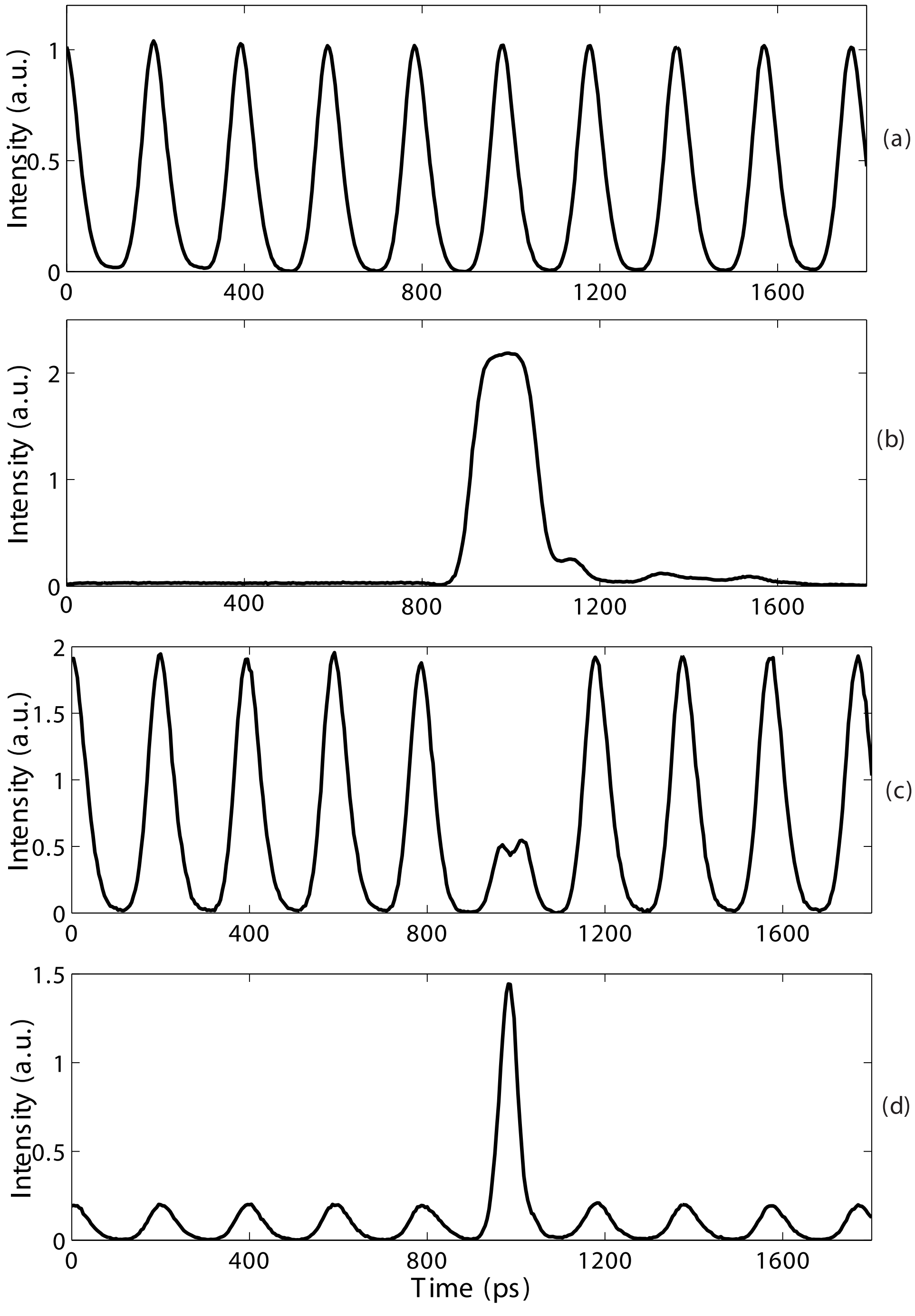

Figure 5.13: Time traces for: (a) the input 5 GHz RZ data stream slightly detuned to the resonance at 1555 nm, (b) the control signal at the 1545 nm resonance, (c) unswitched data at the throughput port, and (d) demultiplexed data at the drop port.

5.4 Conclusion

In this chapter, we demonstrated all-optical switching in a GaAs-AlGaAs microring resonator coupled to a single bus waveguide by TPA using the pump-and-probe method. The dominant nonlinear effect observed experimentally is the carrier-induced change in the refractive index by TPA. The dynamic performance of the device is confirmed by our simulation model to match with measured data. Also, we demonstrated the use of such device in pulse reshaping. Moreover, using a microring resonator in the OCDF configuration, we demonstrated demultiplexing and spatial pulse routing. The switching speed of these devices is currently limited by the carrier life time, and the performance may be further improved by DC biasing the ring waveguide to sweep out free carriers more rapidly. The pump energy required for switching can be drastically reduced by designing the resonator to have a higher FE, or by more efficient absorption mechanism such as single-photon absorption. While employing a gain section inside the resonator as well as between cascaded devices is challenging, it can reduce the input switching energy and compensate for the propagation losses suffered by the device.

CHAPTER 6

PHOTONIC LOGIC GATES USING SEMICONDUCTOR MICRORING RESONATORS

Photonic logic gates are key elements for realizing optical signal processing and computing systems. Intensity-dependent all-optical logic gates have been proposed using nonlinear planar waveguide devices such as Mach-Zehnder interferometers and Distributed-Bragg gratings [54, 55]. Microring resonators are good candidates for building logic gates because: (i) they are ultra compact [13, 19], (ii) they offer reduced switching threshold [18,56], (iii) and they have been fabricated on semiconductor platforms which can be highly nonlinear while transparent at the 1550 nm communication window [57]. As we discussed earlier in chapter 1, the intensity circulating inside a ring waveguide can be much higher than that in the bus waveguide due to the resonance effect. This results in enhanced nonlinear effects and lowers the required switching power by up to the fourth order of the cavity finesse [57]. Moreover, the use of a critically-coupled resonator allows higher switching contrast and therefore better device performance [9].

In chapter 5, we have demonstrated all-optical switching in GaAs-AlGaAs based microring devices. The nonlinear effects observed in those devices when operated at the

1.55 μm wavelength are caused by free carriers generated through two-photon absorption (TPA). TPA can be enhanced if the energy of the pumping photons is closer to the band-gap energy of the material. Therefore, quaternary GaInAsP materials are attractive because they can be designed to have energy band-gaps close to 1550 nm, which boosts nonlinear optical phenomena at the communication window. In this chapter, we demonstrate and characterize the performance of InP and GaAs based microring resonators as all-optical logic gates. We characterize both materials in terms of switching energy and speed [58, 59].

6.1 Theory

For a pump pulse which is much longer than the cavity or photon lifetime, a quasi-steady state analysis can be used to solve for the interaction between the pump and probe electric fields circulating inside the micro-racetrack. When the pump beam circulating inside the resonator is partially absorbed, free carriers are generated by TPA according to

$$\frac{dN_{\mathrm{c}}(t)}{dt} = \frac{\alpha_2}{2\hbar\omega} I_{\mathrm{p}}^2 - \frac{N_{\mathrm{c}}}{\tau_{\mathrm{c}}}, \tag{6.1}$$

where N_{c} is the free carrier density, α_2 is the TPA coefficient, ω is the pump beam frequency, I_{p} is the pump beam intensity, and τ_{c} is the free carrier life time. The amount of free carriers generated inside the resonator is quadratically proportional to the pump intensity inside the ring, which is proportional to the resonator field enhancement (FE) squared. In addition, the phase change needed for switching is reduced by the resonator finesse which is proportional to FE^2. The input optical energy needed for switching is thus reduced by the sixth power of the resonator field enhancement factor or FE^6. On the other hand, thermal nonlinearity is only proportional to the intensity inside the resonator. Moreover, the resonator bandwidth is inversely proportional to FE^2. Therefore, one can design the device to operate with a dramatically low switching power while at high speed data streams.

Since the guiding layer of the InP and GaAs devices are designed to have bandgap energies at 1380 nm and 800 nm respectively, the 1550 nm pump pulses are partially absorbed through TPA inside the resonator and free carriers are generated. This results in a temporal decrease in the refractive index of the resonator waveguide and thus a blue shift in its resonance wavelengths. When a probe beam is initially tuned to resonance, it is highly attenuated at the output or '0'. If 'A' and 'B' are the input data streams, then when either 'A' or 'B' is '1', the amount of phase shift acquired by the resonator is not enough to switch the probe out of resonance. However when both signals are '1's, the amount of generated carriers is 4 times higher because of the quadratic dependence of the TPA. Moreover, the nonlinear transmission of the resonator enhances the switching and brings the probe beam out of resonance to '1' or high transmission. This in return functions as an AND logic gate. If the probe beam is initially out of resonance, then the device can be operated as a NAND logic gate.

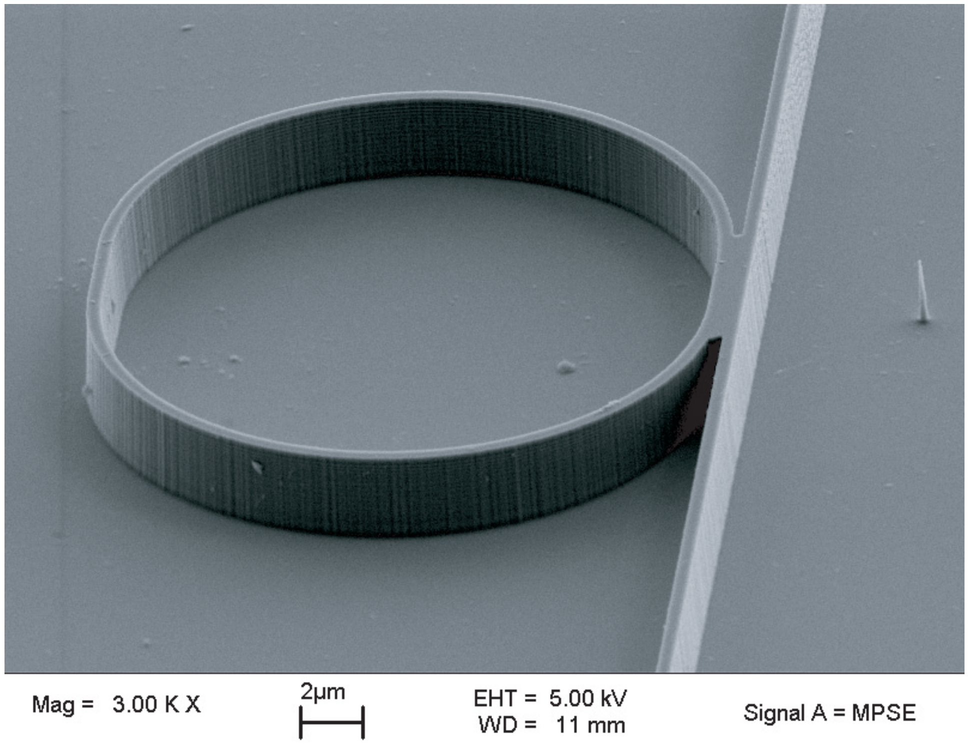

Figure 6.1: Scanning Electron Microscope (SEM) picture of the InP racetrack resonator.

6.2 Experiment and Results

6.2.1 InP Devices

6.2.1.1 Device Description

We first tested the InP devices. The device used in the experiment, a laterally coupled ring, is shown in Fig. 6.1. It consists of a racetrack resonator that has a 10 μm radius and a 3 μm straight coupling section. The waveguide core is made of GaInAsP and has a cross section area of $0.5 \times 0.5 \mu\text{m}^2$. Fig 6.2 shows the measured spectral response at the throughput port of the race-track resonator for S-polarized input light. The linear

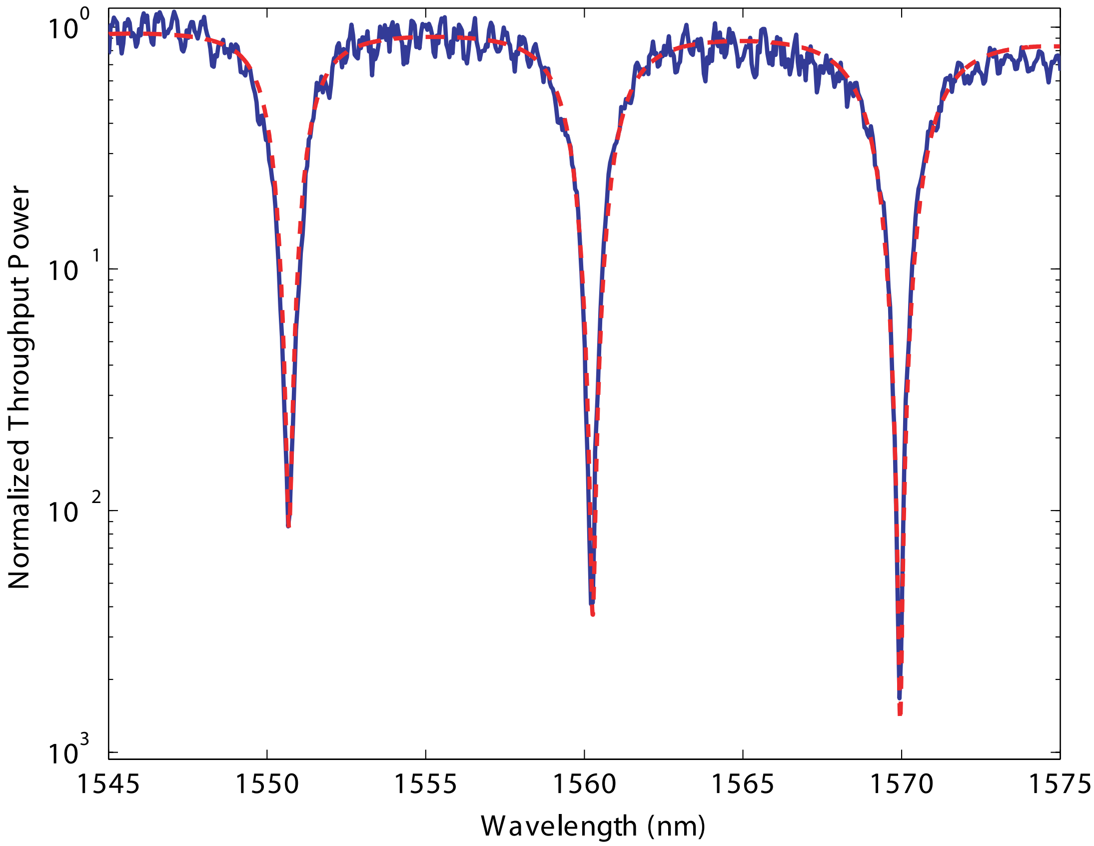

Figure 6.2: Measured (solid line) and fitted (dashed line) spectral response at the throughput port of the racetrack resonator.

parameters of the resonator are extracted by fitting the throughput spectral response. A unique solution for the round trip loss and the coupling coefficient can be found if both the resonance band width and its extinction can be measured precisely. As can be seen in Fig. 6.2, the long wavelength resonance has a deeper extinction as it is closer to the critical coupling point. The extinction depth varies from one resonance to another because the coupling coefficient is wavelength dependent. For the resonance at 1550 nm,

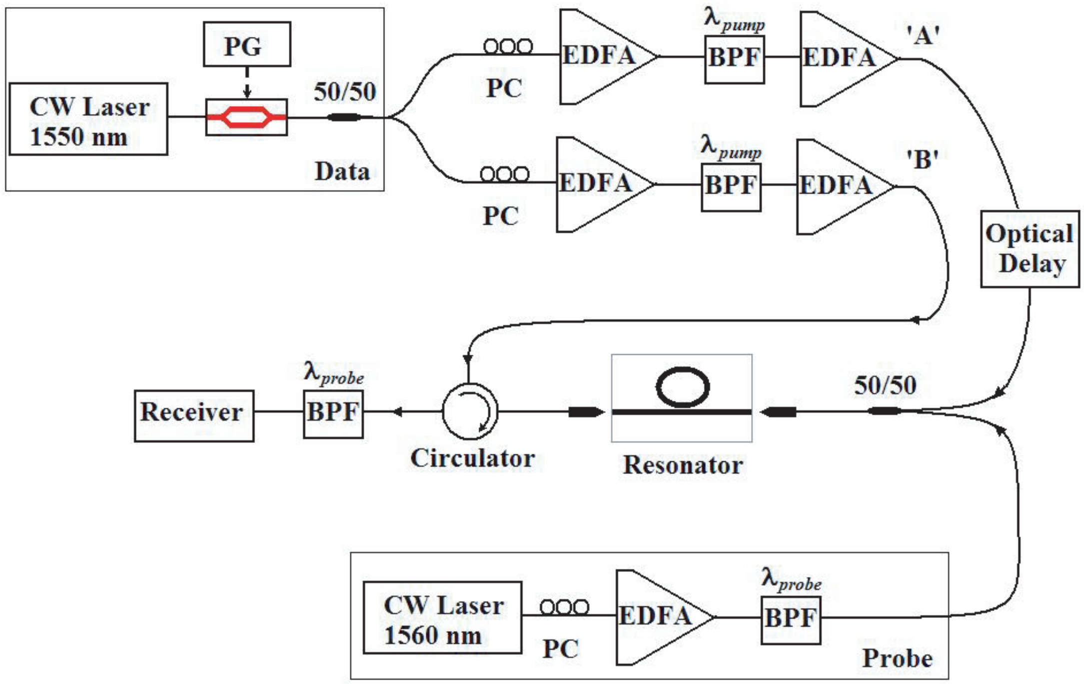

Figure 6.3: Experimental setup for the photonic logic AND gate using the micro-racetrack resonator. PG: Pattern generator, PC: Polarization controller, BPF: Band-pass filter.

the extinction is 20 dB, the round-trip power loss is 40%, and the coupling coefficient is 46%. The ring resonator has a 3-dB bandwidth of 1.8 nm, a free spectral range of 10 nm, a finesse of 6, and an estimated FE of 1.5.

6.2.1.2 Experimental Setup

In Fig 6.3, we plot a schematic diagram for the experimental setup used to demonstrate the logic gate operation. The device is pumped by two counter-propagating data streams in analogy with [60]. A pump beam source, consisting of a continuous-wave (CW) external-cavity laser diode tuned to the resonator resonant wavelengths at 1550 nm, is externally modulated by a pattern generator. The pump pulses are RZ data generated at 0.5 GHz with 500 ps pulse duration. They are split by a 50/50 coupler into two counter-propagating data streams channels, ‘A’ and ‘B’. Each channel is separately amplified by two EDFAs, filtered with a band-pass filter, and injected into one port of the device using a conically-tipped fiber. The pump pulse energy is 18 pJ at the input of the device. A variable optical delay line is used to adjust the arrival of one data channel with respect to the other at the resonator. The probe beam, a CW signal tuned to the resonator resonance at 1560 nm, is amplified separately and coupled with one of the data channel using a 50/50 coupler. The probe power is 10 mW at the device input. The output probe is collected using a fiber circulator, band-pass filtered at the probe beam wavelength, optically-amplified, and fed to a 40 GHz detector and a 50 GHz oscilloscope. The circulator is used to pass the input pump data to the device while passing the output probe signal to the receiver.

6.2.1.3 Results

In Fig 6.4, we plot the time traces of the inputs and output data patterns illustrating AND gate operation. The probe beam is initially tuned to resonance and hence suffers low transmission or ‘0’. We have adjusted the intensity and wavelength of the pump beams, ‘A’ and ‘B’, such that each one can not switch the probe beam out of resonance by itself. When both ‘A’ and ‘B’ are ‘1’s, the intensity is 4 times higher and is enough

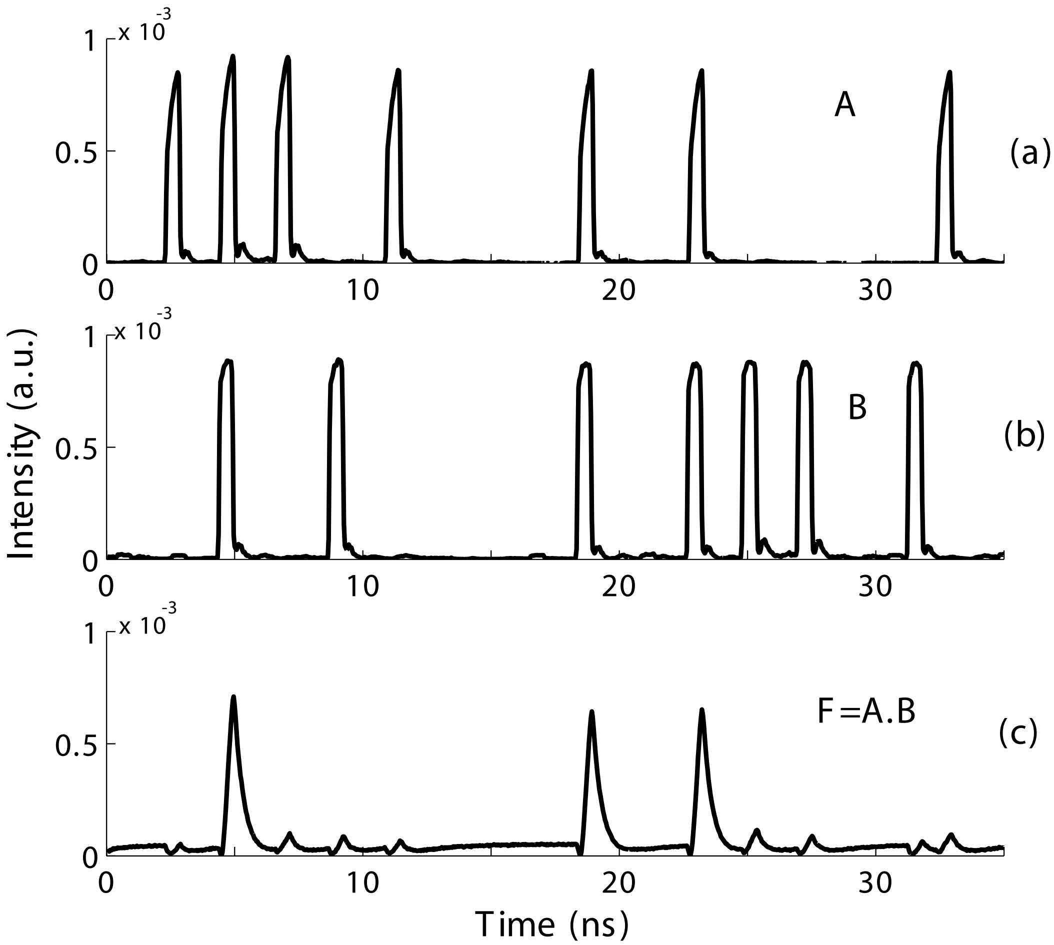

Figure 6.4: Time traces showing the AND logic gate operation using the InP microresonator. (a)'A' and (b)'B' are the two input pumps tuned to the resonance at 1550 nm and (c)'F=A.B' is the output probe signal tuned to the next higher resonance at 1560 nm.

to switch the probe out of resonance to the ON or ‘1’ logic state. The estimated pump intensity required to switch the probe beam out of resonance is 0.2 GW/cm^2, when the pump beam is tuned to the max slope of the resonator where the switching sensitivity is maximum [56].

6.2.1.4 Device Speed

We investigated the speed of the device using a mode-locked laser at 5.6 GHz and externally modulated at 140 MHz. The pump pulse had a pulse width of 35 ps and energy of 20 pJ. The actual input energy at the device was considerably less, as discussed later. In Fig. 6.5, we show the device on-off and off-on switching windows, when the probe beam was initially blue tuned out and to the 1550 nm device resonance, respectively. We measured a switching window of 100 ps, limited by the carrier life-time, and a 13 dB switching contrast, limited by the noise floor of the receiver. From measured data and simulation model, we estimate a 0.9 nm temporal tuning of the microring resonator for that amount of pulse energy.

6.2.2 GaAs Devices

6.2.2.1 Device Description

We also investigated the performance of similar GaAs devices [9]. The device we tested has the same configuration as the one shown in Fig. 6.1. It has a resonance at 1548 nm with an extinction of 19.5 dB, a round-trip power loss of 20%, a coupling coefficient of 25%, a 3-dB bandwidth of 0.78 nm, a free spectral range of 11 nm, a finesse of 14, and

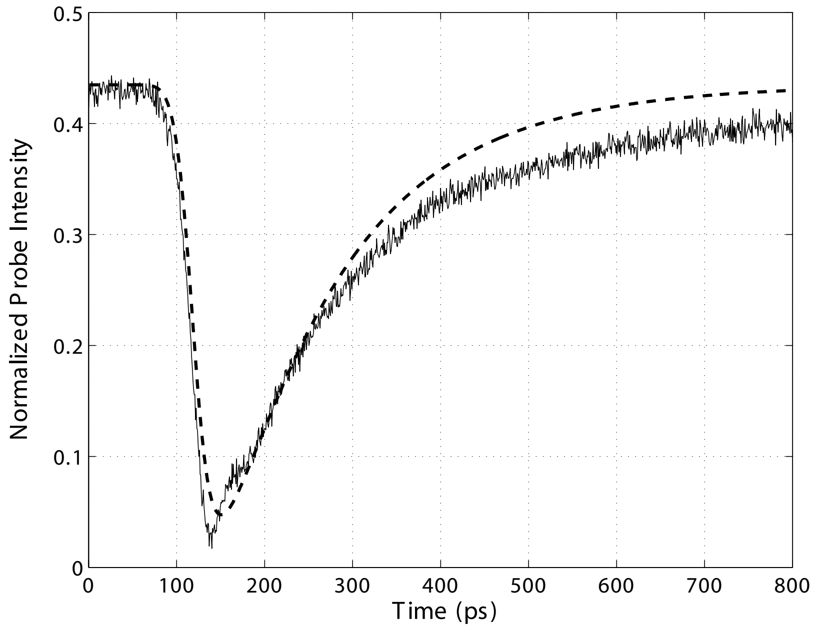

(a)

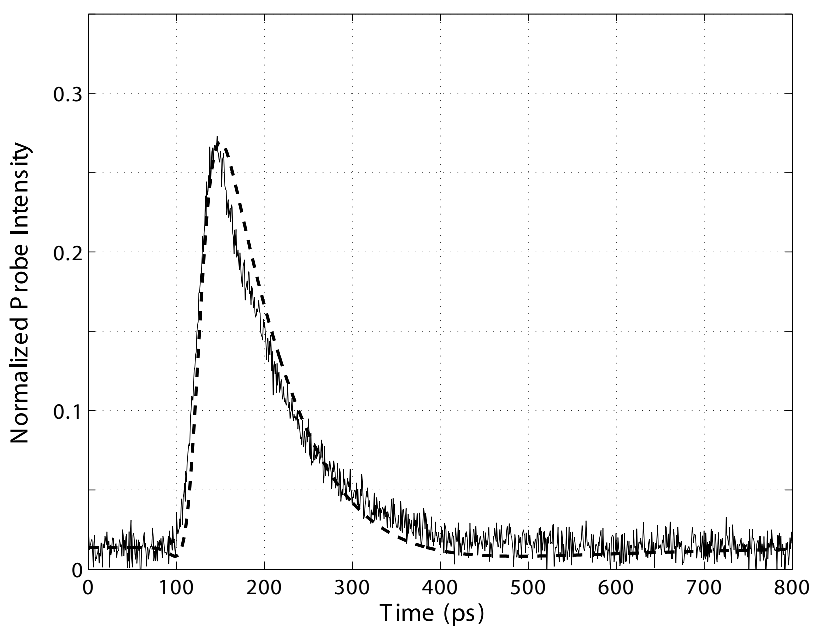

(b)

Figure 6.5: Transient response of the InP micro-racetrack resonator when (a) the probe beam is initially blue tuned to the 1550 nm resonance, and (b) the probe beam is initially tuned to resonance.

an estimated FE of 2.2.

6.2.2.2 Setup and Results

We used an experimental setup similar to the one shown in Fig. 6.3. To obtain high speed data, a gain-switched laser diode at 8.4 GHz and externally modulated at 140 MHz, is used for the data source. The pump pulses have energy of 80 pJ per pulse at the input waveguide of the device. Again, the actual pulse energy coupled to the device is hard to measure. The pump data are tuned to the device resonance at 1548 nm while the probe beam is tuned to the resonance at 1559 nm. The probe beam has a power of 10 mW at the input waveguide. In Fig. 6.6(a) and (b), we plot the time traces for the inputs ‘A’ and ‘B’ and in Fig. 6.6(c) we plot the output probe ‘F’ when the probe beam was initially tuned to resonance. It shows that the output is only ‘1’ when both ‘A’ and ‘B’ are ‘1’s, demonstrating AND gate operation. In Fig. 6.6(d), we plot the output ‘F’ when the probe beam was initially 0.4 nm blue tuned to resonance. Initially, the probe beam is highly transmitted or ‘1’. When both ‘A’ and ‘B’ are ‘1’s, the generated carriers shift the resonance wavelength enough to bring the probe beam in resonance and thus suffers low transmission or ‘0’. This shows a NAND gate operation. In both cases, the output ‘F’ can be seen to follow the inputs instantaneously. The switching window of the device is 35 ps limited by the carrier lifetime and the detection system bandwidth. This implies that all-optical logic operation using our GaAs microring resonator is feasible up to 30 Gb/s.

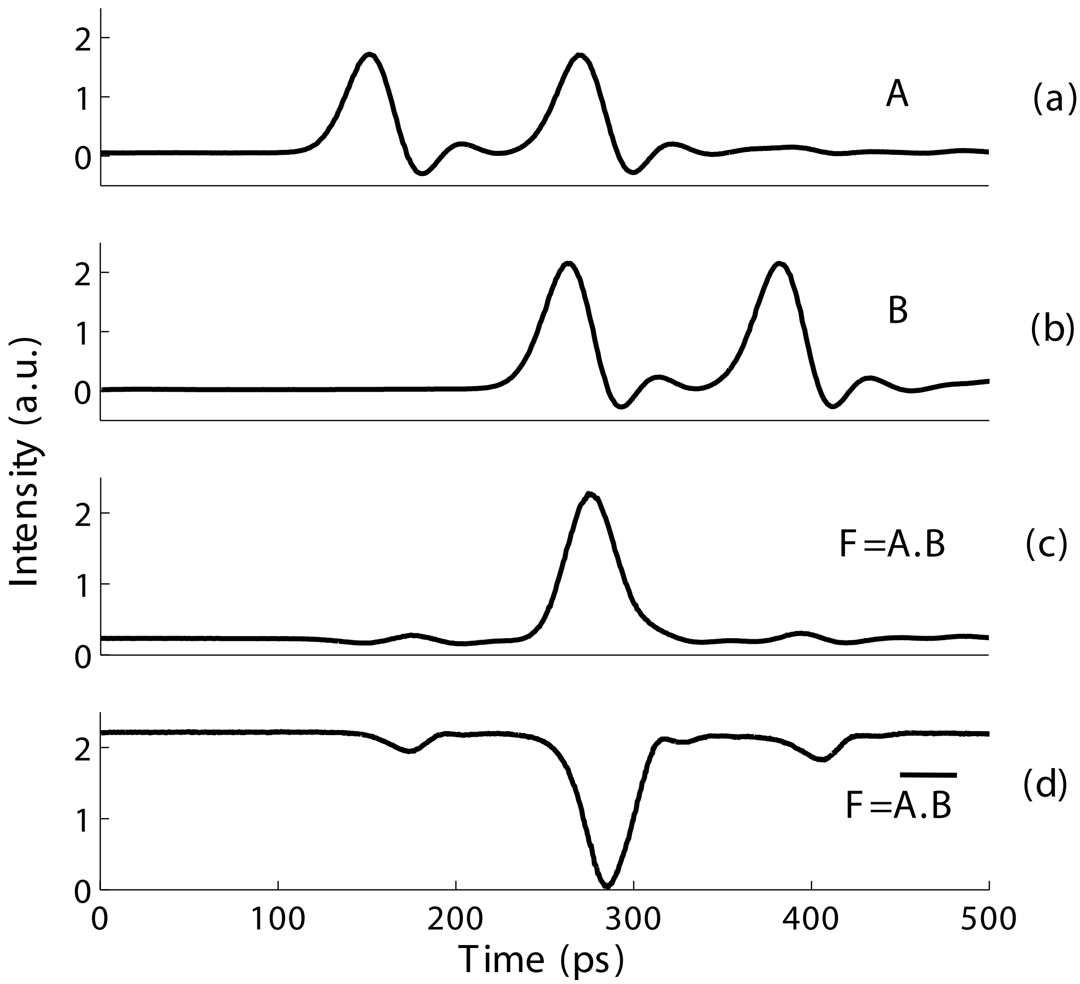

Figure 6.6: Time traces showing logic operation using the GaAs microresonator: (a) and (b) are the inputs 'A' and 'B' tuned to the resonance at 1548 nm; (c) output 'F' when the probe is initially in resonance at 1559 nm; and (d) output 'F' when the probe is initially blue tuned out of resonance at 1558.6 nm.

6.3 Discussion

6.3.1 Nonlinear Loss

The total propagation loss inside the microring resonator is given by

$$\alpha = \alpha_0 + \alpha_2 I_\mathrm{r}. \tag{6.2}$$

We have previously measured the TPA coefficient, α_2, for both GaAs and InP straight waveguides using the single-beam transmittance technique. We estimate a value of α_2 to be 18 and 43 cm/GW for GaAs and InP, respectively. Based on these values, the contribution of the nonlinear loss term given by $\alpha_2 I_\mathrm{r}$ can be neglected and the assumption of constant round trip loss inside the resonator is valid for the amount of pump intensity that we used for the logic gate experiment.

6.3.2 Device Speed

When free carriers are injected into an intrinsic waveguide, both electrons and holes start to diffuse with different thermal velocities. The motion of electrons creates a charge imbalance and results in an internal electric field, E, that drags the holes along with it. The total flux of the charged electrons and holes is thus composed of a drift component and a diffusion component. This can be expressed as

$$\begin{aligned} J_\mathrm{e} &= -\mu_\mathrm{e} n_\mathrm{e} E - D_\mathrm{e}\frac{\delta n_\mathrm{e}}{\delta x}, \\ J_\mathrm{h} &= -\mu_\mathrm{h} n_\mathrm{h} E - D_\mathrm{h}\frac{\delta n_\mathrm{h}}{\delta x}, \end{aligned} \tag{6.3}$$

where μ_e and μ_h are the electron and hole mobilities, n_e and n_h are the electron and holes densities in cm^{-3}, and x is the direction of motion. The electron and hole diffusion constants, D_e and D_h, are given by the Einstein relationship, $D = (\mathrm{KT}/q)\mu$, where $\mathrm{KT} =$ 25 meV at room temperature, and q is the electron charge. The charge neutrality holds, so that $n_e = n_h = n$. Now with the assumption that the imbalances in the fluxes are very small, we can extract the internal electric field to be

$$E = \frac{D_h - D_e}{n(\mu_e + \mu_h)} \frac{\delta n}{\delta x}. \tag{6.4}$$

By substituting from Eq. 6.4 into Eq. 6.3, we obtain

$$J = J_e = J_h = -\frac{\mu_e D_h + \mu_h D_e}{\mu_e + \mu_h} \frac{\delta n}{\delta x}. \tag{6.5}$$

We thus end up with an expression in which the flux of the charged carriers is simply proportional to the negative gradient of the carrier concentration. Eq. 6.5 is a simple diffusion equation with a new ambipolar diffusion constant given by

$$\begin{aligned} D_a &= \frac{\mu_e D_h + \mu_h D_e}{\mu_e + \mu_h} \\ &= \frac{2 D_e D_h}{D_e + D_h}. \end{aligned} \tag{6.6}$$

The ambipolar mobility is thus given by

$$\mu_a = \frac{q}{\mathrm{KT}} D_a. \tag{6.7}$$

Assuming diffusion to the waveguide side walls is the dominant recombination process, the ambipolar carrier lifetime is approximately given by

$$\tau_a = \frac{L^2}{D_a}, \tag{6.8}$$

where L is the diffusion length and approximately equals to half the waveguide width.

We measured the carrier lifetime of the materials by pumping a straight waveguide section and probed the induced absorption at a different wavelength. The carrier lifetime is 50 ps and 120 ps for GaAs and InP 0.5 μm wide waveguides, respectively. Since the waveguides guiding layers are intrinsic, ambipolar diffusion is expected. From Eqs. 6.8 and 6.7, we estimate the ambipolar mobility of GaAs as 500 cm^2/Vs and of InP as 210 cm^2/Vs. Using published hole and electron diffusion constants and mobilities [61], we calculated the ambipolar mobility for GaAs and InP to be 738 and 290 cm^2/Vs, respectively, not far from measured values. Faster response can be achieved by shortening the carrier lifetime through one of several methods. By DC biasing the microresonator waveguide, a static electric field normal to the epitaxial layer is induced which rapidly sweeps the free carriers out of the waveguide core [62]. In a second method, doping the guiding layer with p-type carriers will result in a reduced n-type minority carrier lifetime, which is much shorter than the ambipolar lifetime [63]. Engineering the bandgap through tensile strain can also enhance the hole mobility and thus shorten the carrier lifetime.

In Table 6.1, we summarized the published GaAs and InP holes and electrons mobilities, diffusion constants, and the measured ambipolar mobility. It is worth mentioning that in general the device speed is limited by the cavity or photon lifetime, τ_{ph}, as well as the carrier lifetime, τ_c, according to

$$\frac{1}{\tau} = \frac{1}{\tau_{ph}} + \frac{1}{\tau_c}. \tag{6.9}$$

Table 6.1: Electrons, holes, and ambipolar properties of GaAs and InP intrinsic materials.

	GaAs	InP	(Unit)
Electron mobility, μ_e	8500	4600	cm^2/Vs
Hole mobility, μ_h	400	150	cm^2/Vs
Electron diffusion constant, D_e	220	120	cm^2/s
Hole diffusion constant, D_h	10	3.9	cm^2/s
Ambipolar diffusion constant, D_a	19.1	7.5	cm^2/s
Ambipolar mobility, μ_a	738	290	cm^2/Vs
Measured Ambipolar mobility, μ_a	500	210	cm^2/Vs

If the nonlinear process involved is instantaneous, as it is the case for the nonlinear Kerr effect, the speed of the device is ultimately limited by the photon lifetime of the cavity. On the other hand, when a slow nonlinear process is involved, such as carriers generated with a lifetime much longer than the photon lifetime, then the speed of the device is limited by the carrier lifetime.

6.3.3 Nonlinear Refraction

We now calculate the numer of free carriers generated according to Eq. 6.1 and compare it with the estimated value from

$$\Delta n = -\sigma_r \Delta N, \tag{6.10}$$

where σ_r is the refractive volume of the material and is around 10^{-20} cm^3 for both GaAs and InP [64, 65]. The refractive index change is estimated by measuring the shift in the microresonator resonance wavelength and is estimated to be approximately $\Delta n = -10^{-3}$. The free carrier density calculated by Eq. 6.1 is one order of magnitude higher than the estimated value using Eq. 6.10. We believe this discrepancy is due to the difficulty in estimating the actual input power at the coupling section of the microring because of coupling losses and tapering waveguide losses. For the pump intensity used in the experiment, the TPA refractive index change is at least one order of magnitude higher than the Kerr index change because of the quadratic dependence of TPA refraction versus the linear dependence of the Kerr effect refraction. Therefore, the nonlinear Kerr refractive index change has been neglected.

6.3.4 Switching Energy

Finally, based on Eq. 6.10 and the fact that the switching energy of the device scales down by $(\mathrm{FE})^6$, we predict sub-pico joule switching energy is required to operate the logic gate at 100 GHz assuming a carrier lifetime of 10 ps and a microring resonator that has a moderate FE of 4.

6.4 Multiple-Microring based Photonic Logic Functions: NOR Gate

For a complete set of functionally complete logic gates, at least two different logic gate functions are required. So far we have only employed one microring resonator to demonstrate either AND or NAND logic gates. In this section, we will employ two cascaded symmetric microring resonators to demonstrate a NOR logic gate.

6.4.1 Device Description

An optical micrograph of the device is shown in Fig. 6.7. It consists of two 9 μm-radius microring resonators vertically coupled to a throughput straight bus waveguide. Each ring has a drop port separated by 250 μm from the throughput port. These extra input and output ports eliminate the need for any external fiber splitter or circulator as was the case for the single microring logic gate. The 250 μm separation between the drop port and the throughput port is chosen to match the pitch distance of a conically tipped fiber array used to couple light in and out of the device. The throughput and drop waveguides are tapered from 2.5 μm at the cleaved facets to 0.8 μm at the coupling section to the resonators. The 2.5 μm wide facets help to tolerate any possible submicron errors in the 250 μm fiber-to-fiber fixed pitch distance of the fiber array and therefore a reasonable coupling efficiency is obtained. The 0.8 μm width at the coupling sections of the microrings maintains a single mode behavior of the bus waveguide. The device was fabricated using the GaAs wafer shown earlier in Fig. 4.4. A SEM picture for the microring resonators level is shown in Fig. 6.8.

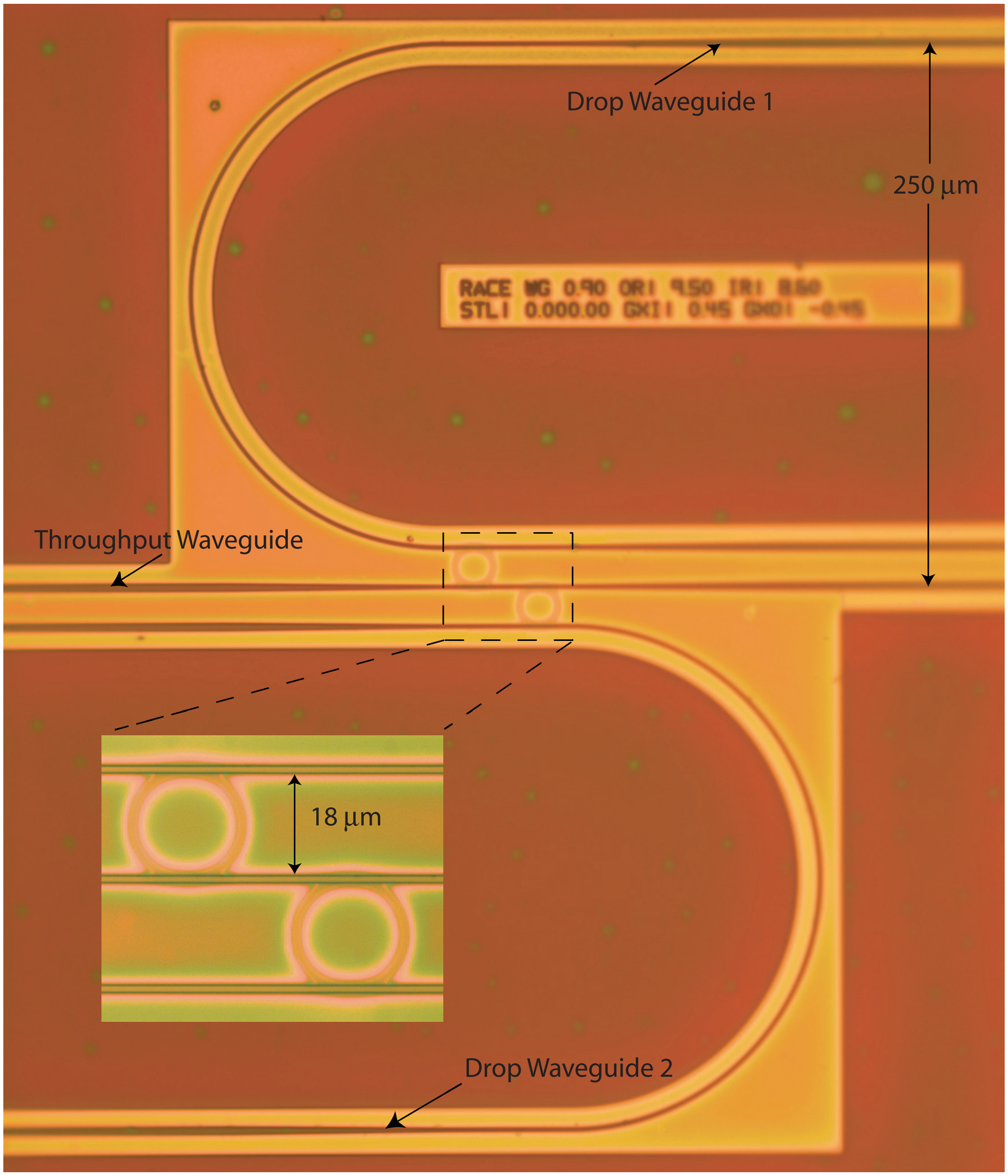

Figure 6.7: Optical micrograph picture of the NOR logic gate. The two microring resonators are symmetric and of radii 9 μm. The etched features appear in orange while the waveguides and the top of the trenches appear in cyan. The subset shows a magnified picture of the microring resonators underneath the bus waveguides.

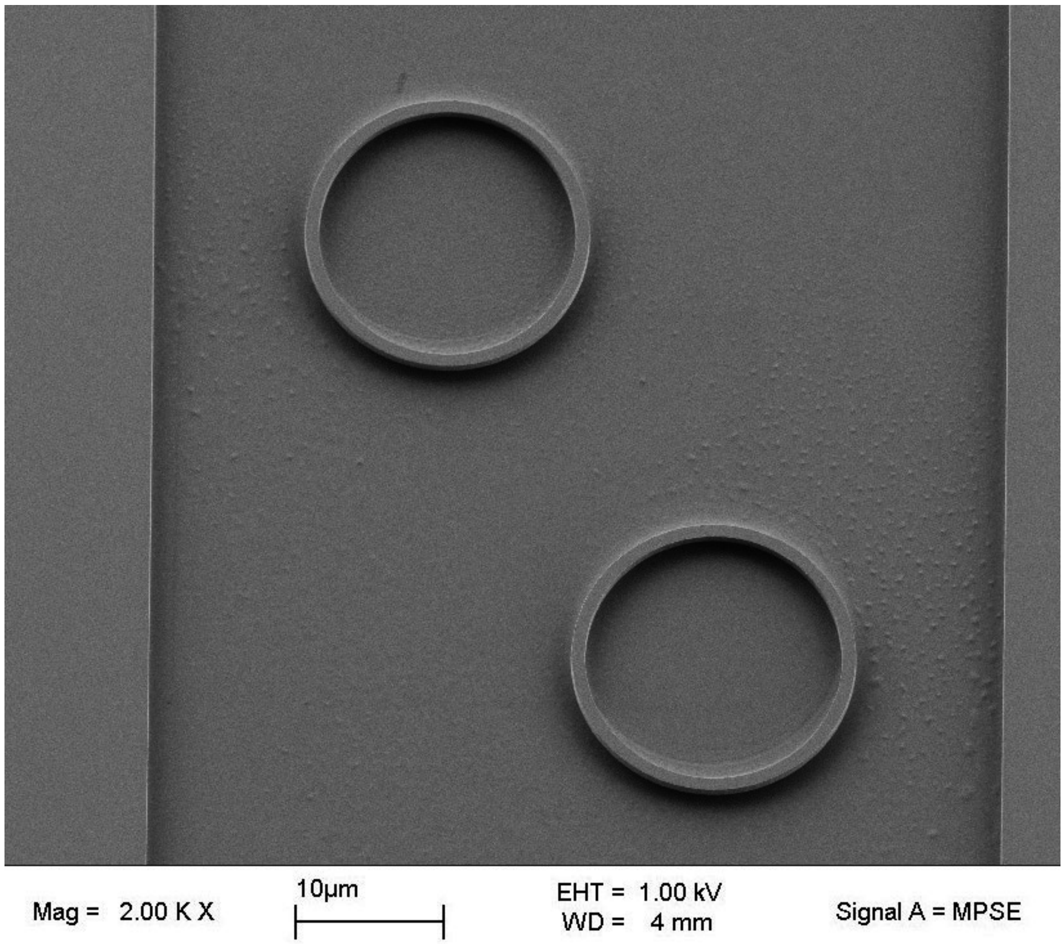

Figure 6.8: SEM picture of the microring level of the NOR logic gate showing the two microring resonators. The picture was taken after the microring level feature etch and before chip-flip bonding to the new carrier.

6.4.2 Linear Characteristics of the Device

The throughput and both drop ports spectrums are shown in Fig. 6.9. The resonance wavelengths of both microrings were designed to coincide with each other. Due to processing imperfections, there is a 0.2 nm shift around the 1557 nm resonance wavelength. In addition, the throughput extinctions do not exceed 10 dB. The resonators have a 3-dB bandwidth of 0.22 and 0.3 nm, a finesse of 47 and 35, a quality factor of 7077 and 5189, and a FSR of 10.42 nm. Assuming symmetric coupling for each resonator, we estimate a coupling coefficient of 5.3% and a round trip loss of 2.3% for the first microring resonator, and a coupling coefficient of 7.2% and a round trip loss of 2.9% for the second microring resonator. The estimated FE factor is 3.6 and 3.1, respectively. Since the pump data wavelengths are chosen to be the same for both microrings and there is a 0.2 nm wavelength mismatch between the two microring resonances due to fabrication errors, high switching energy requirement is expected to compensate for that mismatch.

6.4.3 Experimental Setup and Logic Operation

A schematic diagram for the experimental setup is shown in Fig. 6.10. A CW probe beam, ‘C’, is coupled to the input port of the throughput bus waveguide. Its wavelength is blue tuned to the resonance wavelength at 1557 nm and therefore initially highly transmitted, or ‘F=1’. The two input pump data, ‘A’ and ‘B’, are tuned to the microrings resonances at 1546 nm. When either ‘A’ or ‘B’ is ‘1’, the correspondent microring is blue detuned by the induced free carriers by TPA and therefore the probe beam becomes

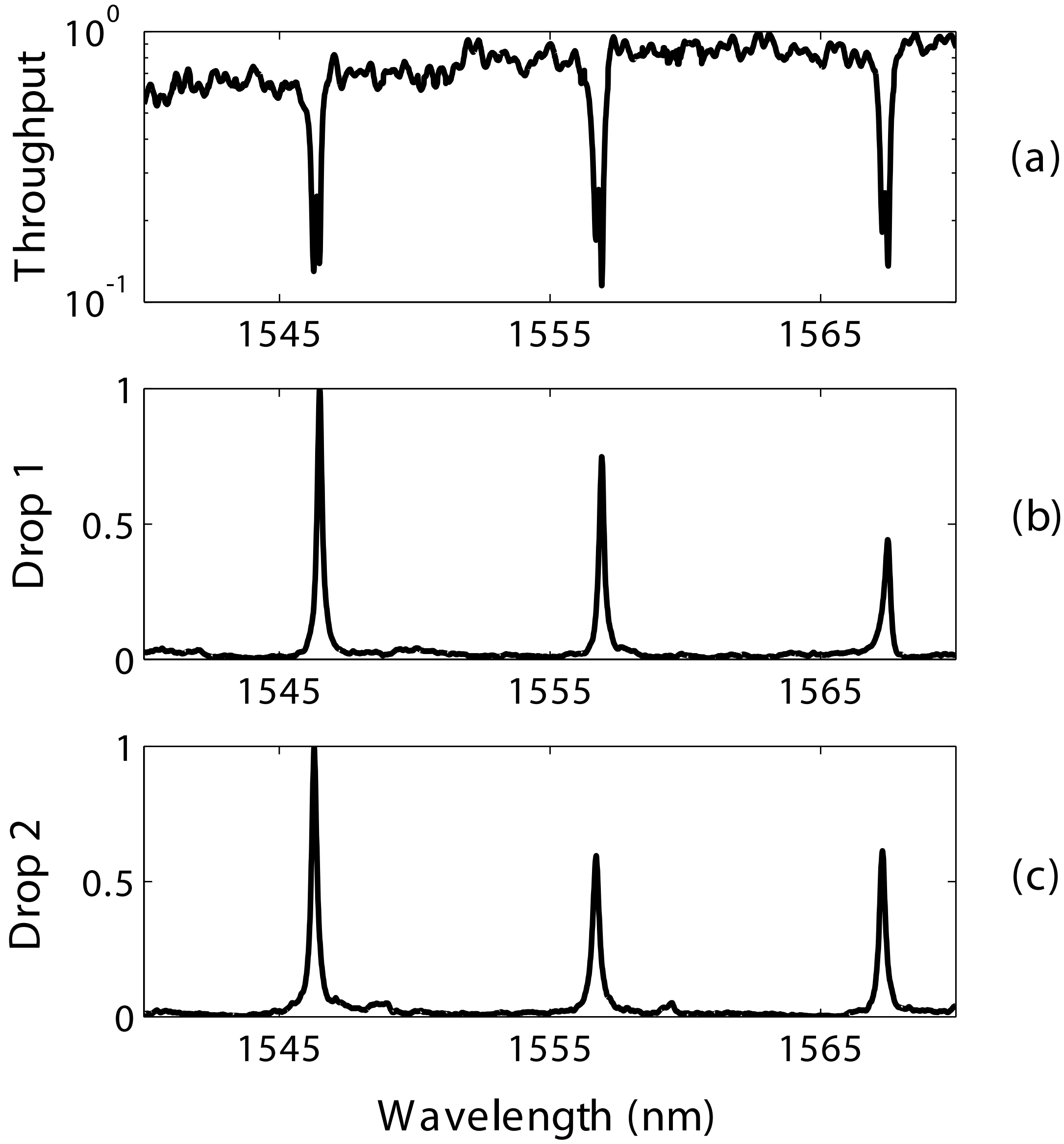

Figure 6.9: Normalized spectrum for the: (a) throughput port, (b) drop port of the first microring resonator, and (c) drop port of the second microring resonator.

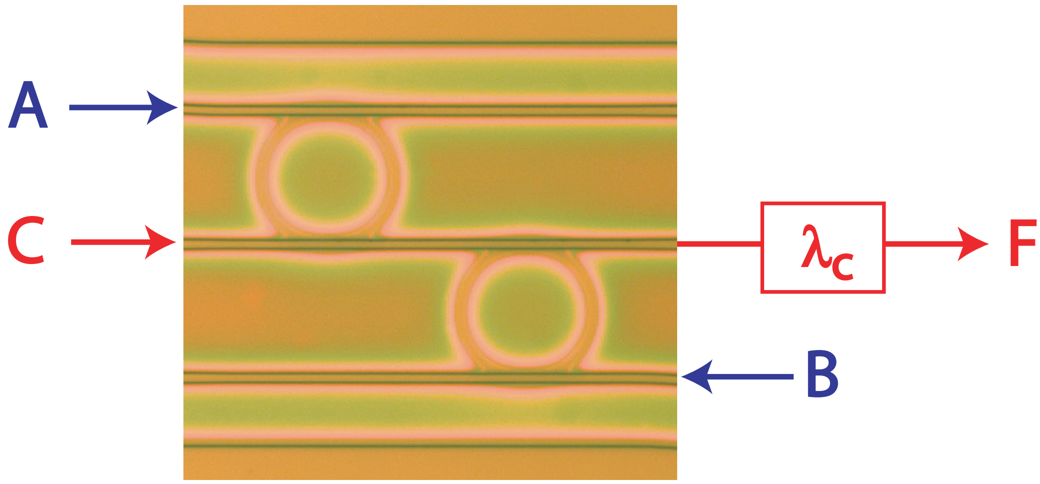

Figure 6.10: Schematic diagram for the experimental setup used to demonstrate a NOR logic function. ‘A’ and ‘B’ are the input data while ‘C’ is the CW probe beam. ‘F’ is the output probe spectrally filtered around λ_c.

temporarily in resonance, or ‘F=0’. When both ‘A’ and ‘B’ are ‘1’s, both microring are blue detuned and again the probe beam becomes in resonance and highly attenuated at the output of the throughput waveguide, or ‘F=0’. Writing the Boolean truth table for this function, we obtain ‘F=$\overline{A}\cdot\overline{B} = \overline{A+B}$’ which represents a NOR logic gate.

In Fig. 6.11 we plot the time traces for the input data streams, ‘A’ and ‘B’, and the output probe, ‘F’, after being spectrally filtered around λ_c. As can been seen, the output is ‘0’ whenever either ‘A’, ‘B’, or both is ‘1’. The output is ‘1’ only if both ‘A’ and ‘B’ is ‘0’. The switching contrast is only 6 dB due to the fact that the resonators are not critically coupled. The switching energy is estimated to be 20 pJ per pulse at the input of the waveguide. This switching energy is higher than expected from device and material

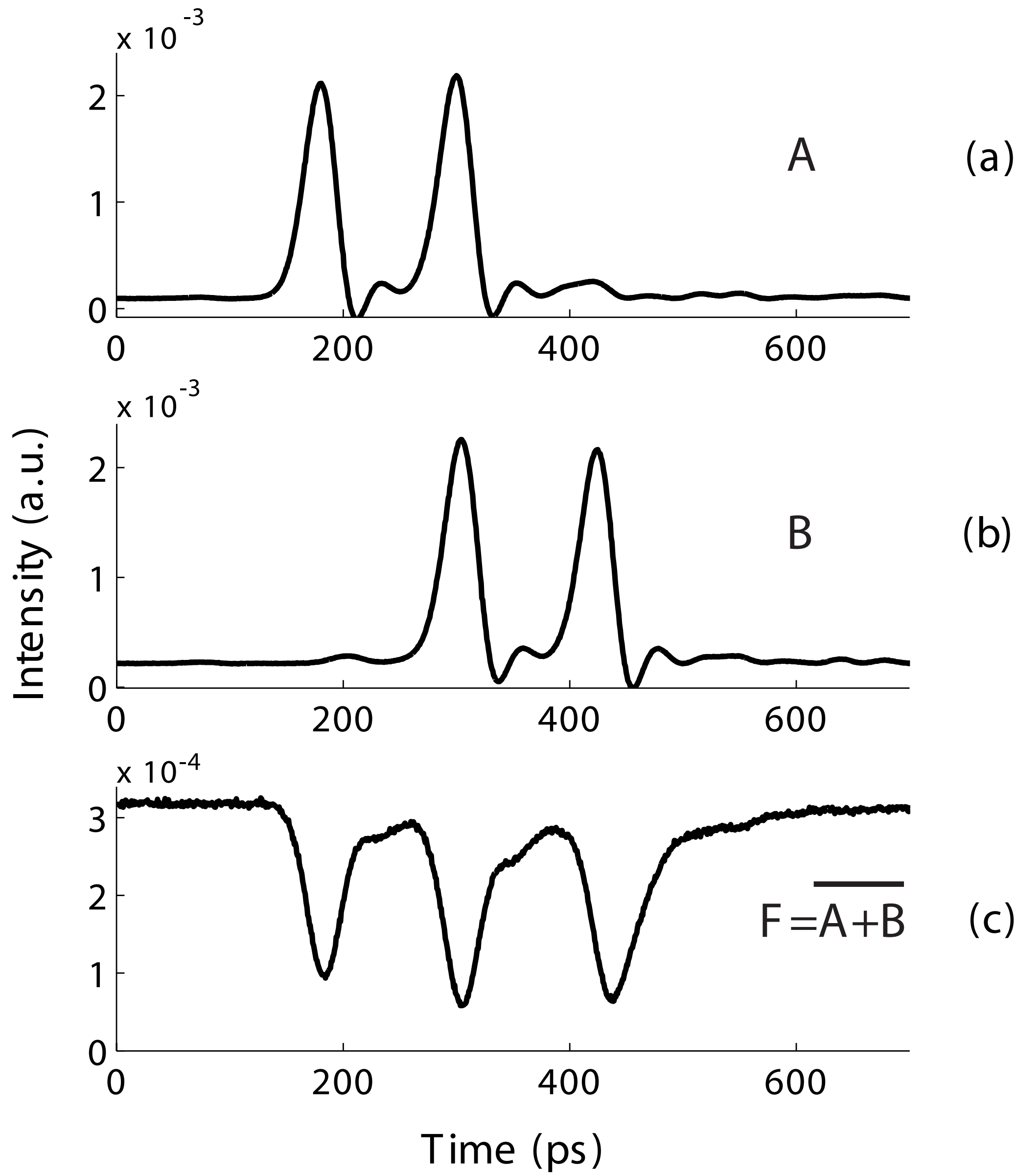

Figure 6.11: Time traces for the input pump data streams (a)'A', (b)'B' at 1546 nm, and (c) the output probe signal at 1557 nm.

parameters [58], and the actual energy at the rings maybe considerably lower. We also believe that the 0.2 nm mismatch between the two microring resonators contributed to that high amount of switching energy. This is mainly due to the fact that the input data wavelengths, ‘A’ and ‘B’, are the same while the two microrings have a slightly different resonance wavelengths and therefore a substantial amount of pump energy was not coupled to the resonators. The switching speed of the device is limited by the time carriers diffuse to the waveguide side walls [66]. The device speed can be enhanced by DC biasing the microresonators waveguides to sweep out the generated free carrier more rapidly.

6.5 Fabrication Limitations

We also designed another photonic NOR logic gate using two symmetric microrings but cascaded in a different configuration. An optical microscope picture of the fabricated device is shown in Fig. 6.12. The device works as follows. A probe beam, ‘C’, is coupled to the middle waveguide of the device. If the probe beam is tuned to the resonance wavelength of both symmetric microrings, then it is dropped by the first microring, then dropped by the second microring, and then directed to the middle output waveguide as the output ‘F’. The transmissions of both microrings are controlled by the pump data beams, ‘A’ and ‘B’, which are tuned to a different resonance of the microrings and fed to the device through the top and bottom waveguides. The pump beam ‘A’ controls the transmission of the upper microring while the pump beam ‘B’ controls the transmission

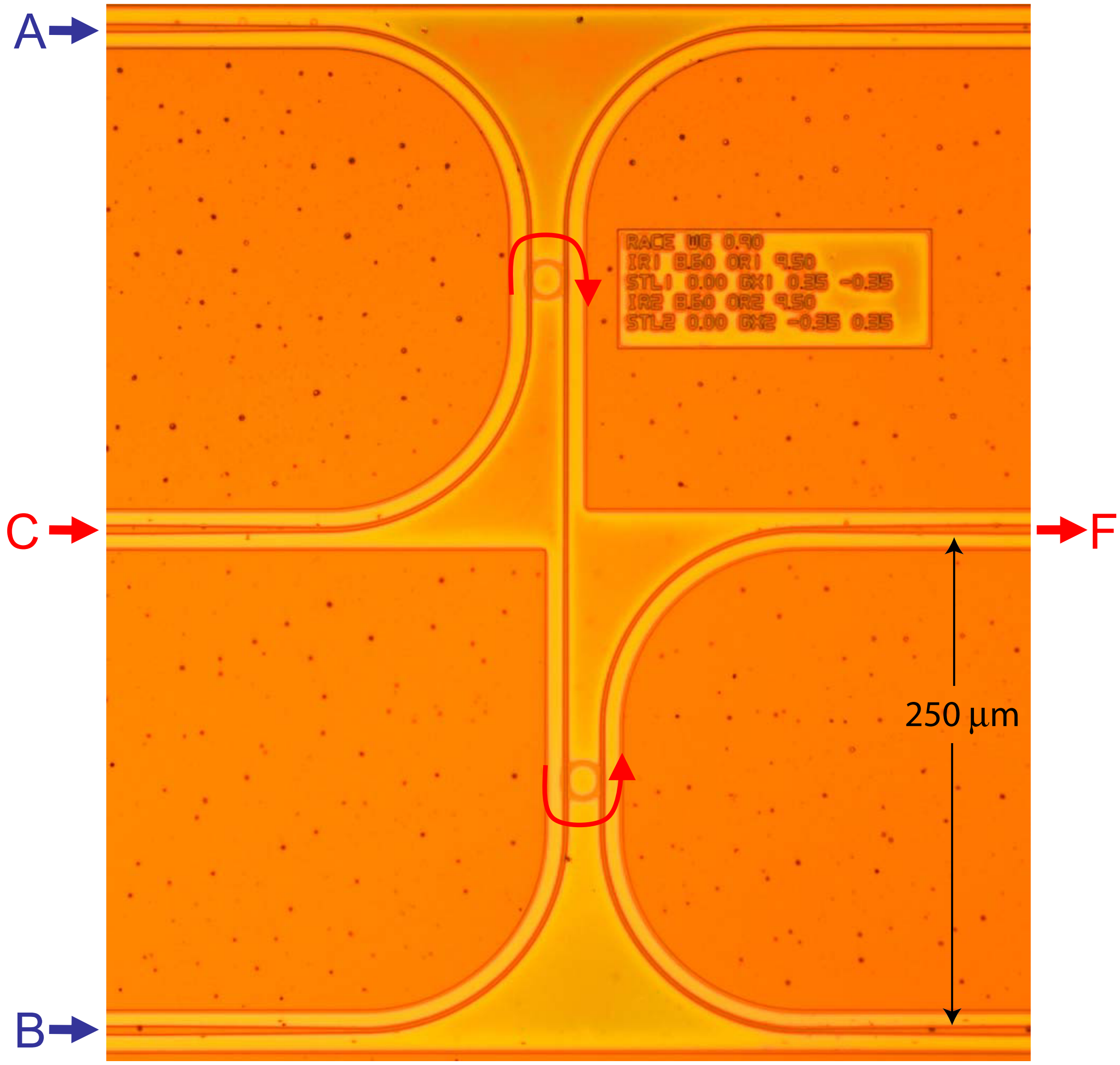

Figure 6.12: Optical microscope picture of two symmetric microrings NOR logic gate in the drop configuration. The red arrows show the path of the probe beam from input to output. The blue arrows show where the pump data, ‘A’ and ‘B’, are coupled to the device.

of the lower microring. Therefore, whenever ‘A’ and ‘B’ are ‘0’s, the probe beam is dropped at the output through both microrings and the output is high, or ‘F=1’. If either ‘A’, ‘B’, or both is ‘1’, either microring or both are detuned from the probe beam wavelength and does not drop it temporarily. At this point, the path of the probe beam to the output is cut and the output goes low, or ‘F=0’. This function as a NOR logic gate. The main advantage of this configuration is that the pump beams, ‘A’ and ‘B’, are circulated to different output waveguides away from the output ‘F’ and therefore there is no need to spectrally filter the output probe signal.

In Fig. 6.13, we plot the throughput spectrum of the device or the S-waveguide where the input light was fed at the lower left waveguide facet while the output is measured at the upper right waveguide facet. The S-waveguide is the throughput waveguide for both microrings (Fig. 6.12). As can be seen in Fig. 6.13, due to fabrication errors, a 0.5 nm resonance shift is obtained between the two microrings and therefore the device can not be used. This resonance wavelengths mismatch can be explained as a difference in the effective refractive indices of both microrings in the order of 10^{-3}, or a difference between their circumferences equal to 20 nm, or a combination of both. We believe that this mismatch is due to the non uniformity of the photo lithography. A promising way to overcome any mismatch due to fabrication errors is to actively tune the individual microrings either by integrated electrodes or embedded micro heaters.

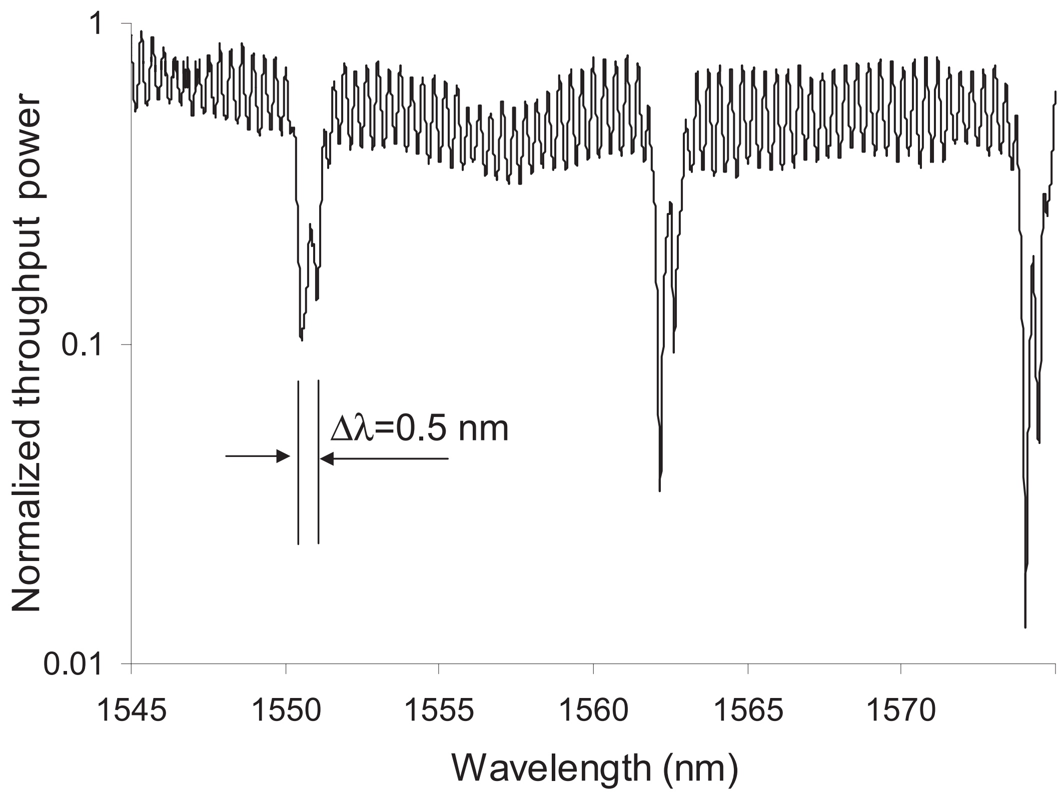

Figure 6.13: Normalized measured throughput power at the output of the S-waveguide of the device. The device is not anti-reflection (AR) coated.

6.6 Conclusion

In summary, we have demonstrated all-optical AND and NAND logic gates using InP and GaAs micro-racetrack resonators. The pump pulses were used to temporarily alter the refractive index of the resonator through free carriers generated by nonlinear absorption, which switches the probe beam out of, or into, resonance only when both inputs were '1's. Furthermore, we have proposed and demonstrated an all-optical NOR logic gate using two cascaded and symmetric GaAs-AlGaAs microring resonators. The performance of these devices can be enhanced by controlling the coupling coefficients of the individual microresonators. Moreover, micro-heaters can be used to control the individual microresonators resonance wavelengths and therefore tolerate any fabrication errors. The switching speed is limited by carrier lifetime and we expect much faster response with DC biasing the microresonator. We predict sub picojoule switching energy for a microresonator that has a moderate field enhancement factor of 4 and a switching window of 10 ps (100 Gb/s).

CHAPTER 7

FREE CARRIER INJECTION IN SEMICONDUCTOR MICRO-RING RESONATORS

When a semiconductor is exposed to light with photon energy above the absorption edge, each absorbed photon creates an electron-hole pair. A moderate density of these injected carriers or excess particles significantly alters the optical properties of the semiconductor. This mechanism is always referred to as a *Resonant* optical nonlinearity, because the photon radiation is close to the bandgap energy of the material. In the late 1970s, it was shown that this effect was large enough to induce optical bistability in semiconductor etalons [67, 68]. In this regard, direct-bandgap semiconductors, such as GaAs, are more attractive because they have an abrupt absorption edge that is easily modified with optical excitation [69].

One way to use the microring resonator as an all-optical switch was discussed and demonstrated in chapter 5 through TPA. The switching speed was limited by the photon lifetime as well as the carrier recombination lifetime. A more efficient technique is free carrier injection induced by Single-Photon Absorption (SPA). In other words, by optically pumping the microring semiconductor material with photon radiation above its bandgap, one can control the refractive index of the microring resonator. In this manner, millimeter-wave propagation in a semiconductor waveguide had been controlled by an optical signal [70, 71]. This technique offers some advantages in comparison with what has been previously demonstrated using TPA: (1) the pump beam does not need to be tuned to one of the microring resonance wavelengths; (2) the switching speed is no longer limited by the cavity charging time since the pump beam does not resonate in the microring, allowing ultrafast switching to take place; (3) the absorption mechanism is much more efficient and (4) with proper pump beam spot size and wavelength, switching power can be much smaller. In [72], tuning of a micro-disk resonator filter was demonstrated by carrier injection through an electrical current. However, such technique suffers from the parasitic capacitance effects associated with the contacts, therefore limiting the switching speed and the capability of the device.

In this chapter, we demonstrate lightwave switching in laterally coupled GaAs-AlGaAs microring resonators by free carrier injection. The ring waveguide is optically pumped just above its bandgap energy, which results in a temporal tuning of the microring resonant wavelengths by the refractive index change due to the induced free carriers [66]. Both the transmission and the phase functions of the resonator are investigated and used to demonstrate all-optical switching. Dr. W. Cao, Y. Kim and J. Li have helped me through this experiment and in the simulation model.

7.1 Transmission Switching

First we consider and examine the use of the transmission-transfer function of the Add/Drop Micro-Racetrack resonator for all-optical switching purposes.

7.1.1 Theory

The electric field circulating inside the micro-racetrack resonator shown in Fig. 7.1(a) can be written as:

$$E_{\mathrm{r}}(t) = -j\kappa_1 E_{\mathrm{i}} + r_1 r_2 a\, e^{j\phi} E_{\mathrm{r}}(t-\tau), \tag{7.1}$$

where E_{i} is the input Continues Wave (CW) probe beam, r_1 and r_2 are the field transmission coefficients at the input and output waveguides, respectively, a is the round trip field transmission, κ_1 is the field coupling coefficient between the input waveguide and the racetrack waveguide such that $\kappa_1^2 + r_1^2 = 1$, and τ and ϕ are the round trip time and phase of the resonator, respectively.

The round trip phase, ϕ, defined by Eq. 1.3 is proportional to n, the refractive index of the ring waveguide, which in return is a function of the carrier density injected in the ring waveguide. The dynamic behavior of the circulating electric field can be simulated by numerically solving Eq. 7.1 after substituting from Eq. 1.3.

7.1.2 Device Characteristics

The first device used in the experiment is shown in Fig. 7.1(b) [45].It consists of a 5 μm radius racetrack resonator laterally coupled to two straight waveguide buses with

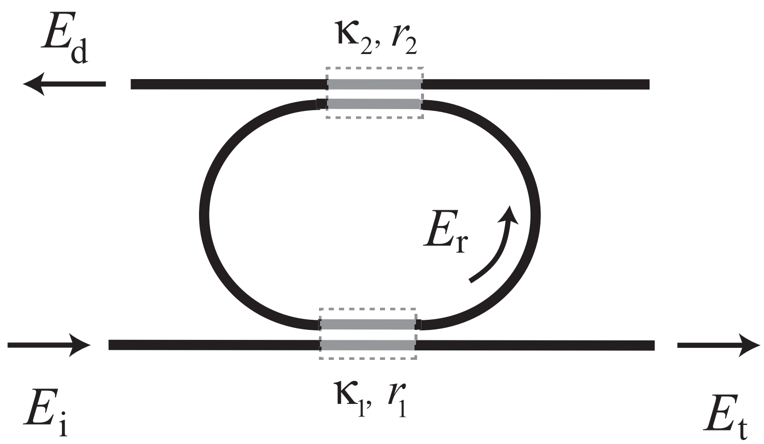

(a)

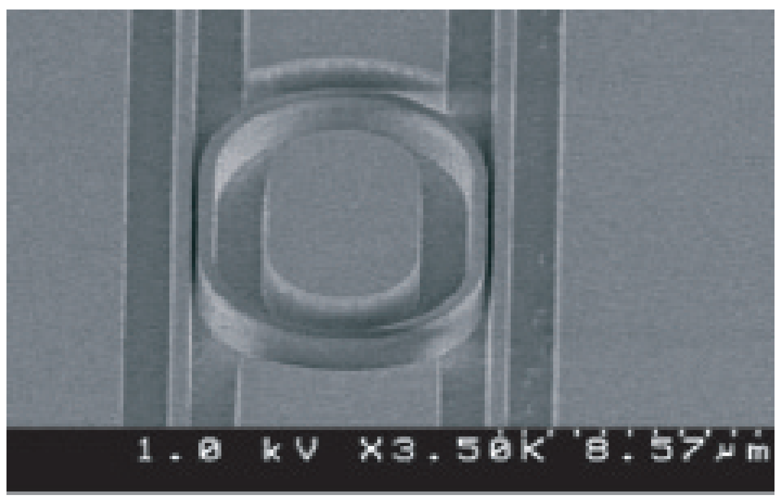

(b)

Figure 7.1: (a) Schematic diagram for a racetrack resonator coupled to two straight waveguides and (b) Scanning Electron Microscope picture of the device used in the experiment.

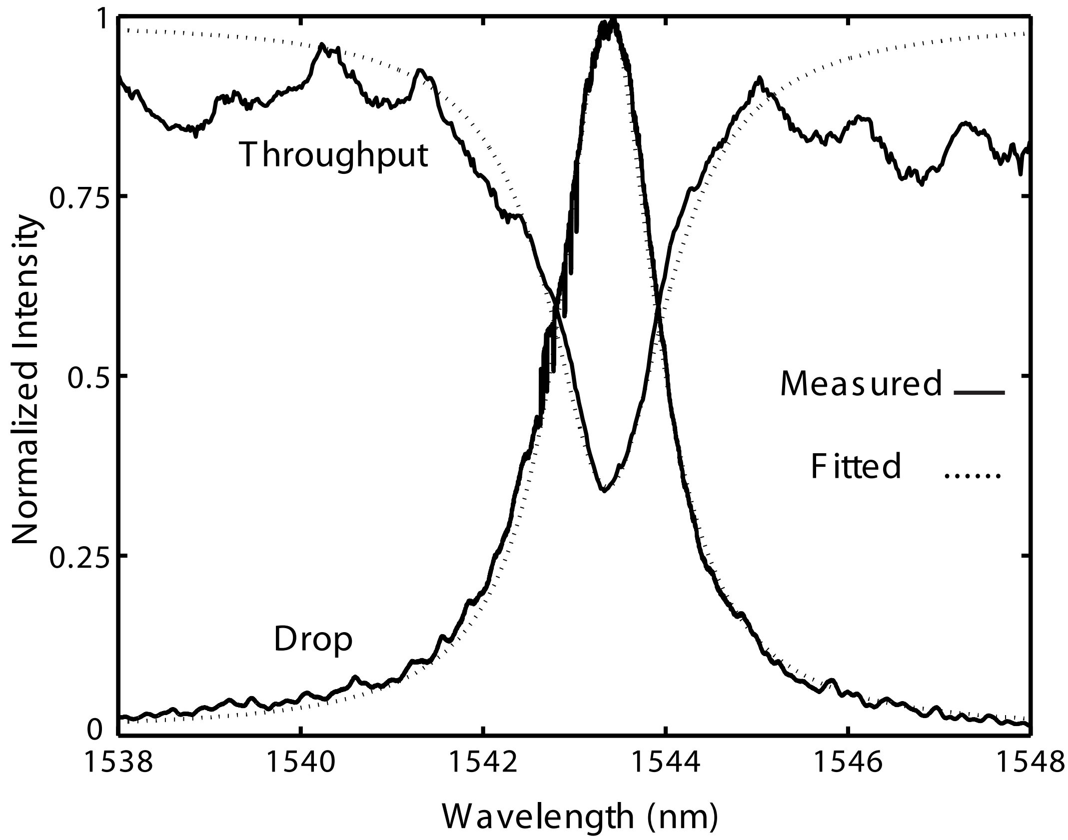

Figure 7.2: Measured (solid lines) and fitted (dotted lines) spectral response at the throughput and drop ports of the microring resonator around 1543.4 nm.

a straight coupling section of 10 μm.

Fig. 7.2 shows the measured spectral response of the micro-resonator at both the throughput and drop ports at resonance mode at 1543.4 nm with the input light S polarized. The resonator linear parameters are extracted by fitting both the throughput and drop port spectral responses with the assumption of symmetrical couplings at the input and output waveguides, i.e., $\kappa_1 = \kappa_2$. The round trip power loss is 24% and the coupling coefficient is 11%. The ring has a 3 dB bandwidth of 1.3 nm, an intrinsic quality factors of 1200, a free spectral range of 18 nm, and a finesse of 14.

7.1.3 Experiment

All-optical switching is accomplished using the pump-probe scheme, in which a high-intensity pump pulse is used to control the transmission of a CW probe beam tuned to one of the micro-racetrack resonances. By sweeping the probe beam wavelength across the microring resonance and detecting the time variation of the dropped signal, the resonance wavelength shift of the microring and hence its refractive index change can be measured. The experimental setup is as follows. The pump beam is a train of model-locked Ti:Sapphire pulses at 800 nm. The pulse width is typically 100 fs with 1 kHz repetition rate. The average power of the beam is attenuated to less than 1 μW at the device surface. A lens system is used to focus the beam to approximately a 25 μm spot size to pump the microring from top. The probe beam is provided by an external cavity semiconductor laser diode which is tunable around 1550 nm. The laser diode is tuned to the micro-racetrack resonance wavelength at 1543.4 nm with an average power of a few mW. The probe beam is fed into the input port of the resonator using a conically tipped fiber. The output of the drop port is also collected with another conically tipped fiber, optically amplified, fed to a 40 GHz detector and monitored by a 50 GHz scope.

Since the bandgap wavelength of GaAs is around 800 nm, the pump pulse is almost fully absorbed in the microring waveguide and high density of free carriers are generated. These carriers decrease the refractive index of the microring waveguide and cause a temporarily blue shift of the microring resonance wavelength. When the free carriers diffuse to the waveguide walls and recombine, the effect diminishes. If a probe beam is tuned to one of these microring resonant wavelengths, the output probe signal will be modulated. The depth of modulation depends on the magnitude of the resonance-wavelength shift. In addition, the steeper the resonator profile, or in other words, the higher the cavity finesse, the larger the modulation of the output signal for a given wavelength shift.

Fig. 7.3(a) shows a 3-dimensional plot of the measured time variation of the dropped probe signal versus its wavelength. When the probe beam is initially tuned to the shorter wavelength side of the microring resonant wavelength, the carrier-induced blue shift in the resonance brings the probe beam into resonance and is temporarily dropped at the output, thus it experiences a rapid increase in transmission. When the probe beam is initially tuned to the resonant wavelength, the carrier-induced index change shifts the resonance away from the probe beam, resulting in a rapid attenuation of the dropped signal. Simulation results shown in Fig. 7.3(b) are in good agreement with measured data. By measuring the switching contrast of the dropped beam at the different probe wavelengths, one can deduce the amount of resonance wavelength shift. Our simulation model yields a maximum refractive index change of 2.6×10^{-3} that leads to a resonance wavelength shift of 1.2 nm. The switching contrast is approximately 7 dB. Higher switching contrast can be obtained by injecting more carriers or by using a critically coupled resonator [9]. A rise time of 10 ps is measured for the dropped probe beam and is limited by the detection system. A switching window of 20 ps is obtained

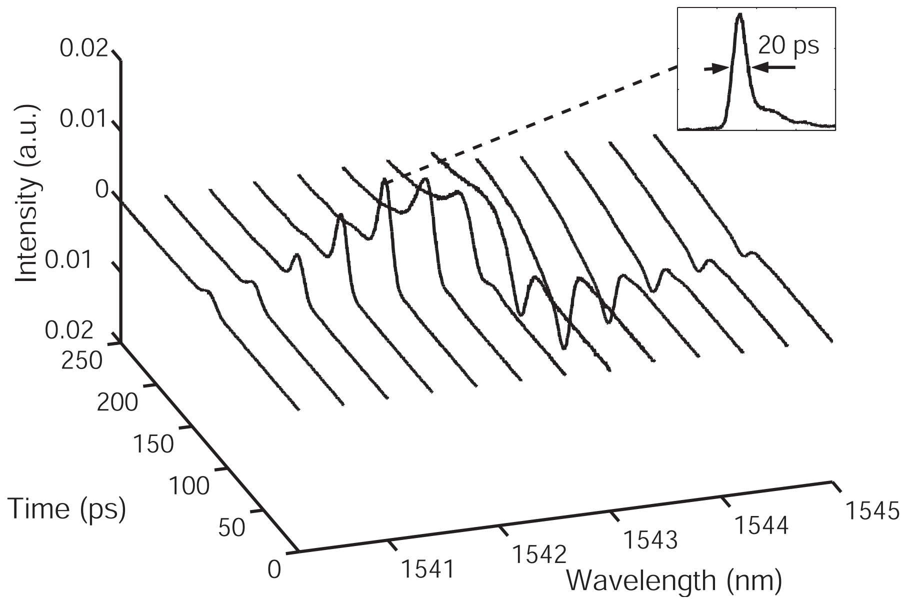

(a)

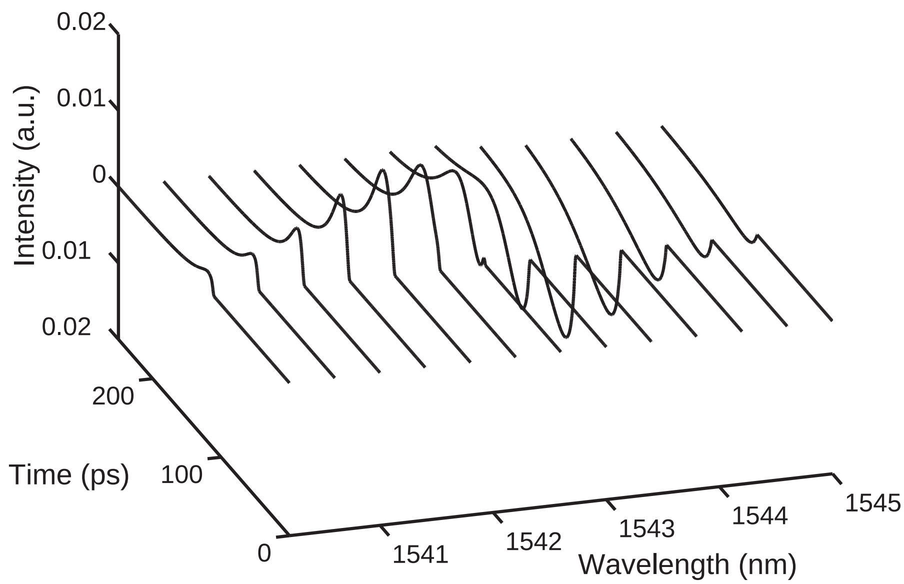

(b)

Figure 7.3: (a) Measured and (b) simulated modulation of the dropped signal for different input probe beam wavelength (The DC level has been removed in both (a) and (b) for clarity).

and shown in the inset of Fig. 7.3(a).

7.1.4 Discussion

When free carriers are injected into a semiconductor waveguide, its refractive index has the following expression [70]:

$$\begin{aligned}\eta, k &= \frac{1}{2}\left\{\pm\left(\varepsilon_L \frac{\omega_p^2}{\omega^2+\nu^2}\right)\right.\\ &\quad \left.+\left[\left(\varepsilon_L - \frac{\omega_p^2}{\omega^2+\nu^2}\right)^2 + \left(\frac{\nu}{\omega}\frac{\omega_p^2}{\omega^2+\nu^2}\right)^2\right]^{1/2}\right\}^{1/2}, \qquad (7.2)\end{aligned}$$

in which η and k, the real and imaginary parts of the complex refractive index, are obtained by selecting the '+' or '-' sign of the leading term of the right hand side of Eq. 7.2, respectively. Eq. 7.2 shows that the refractive index depends on the dielectric constant of the material ε_L, the plasma frequency ω_p, the collision frequency of the carriers ν, and the frequency of the propagating probe beam ω. The plasma frequency is given by:

$$\omega_p^2 = \frac{N_p e^2}{\varepsilon_0 m^*} \qquad (7.3)$$

where N_p is the free carrier density, e is the free electron charge, ε is the free space permittivity, and m^* is the effective mass of the carrier.

The effective pump energy that hits the microring is 20 pJ/pulse and this corresponds to 8×10^7 photons/pulse. Since the absorption coefficient of GaAs at 800 nm is 10^4 cm^{-1}, a carrier density of 2.5×10^{18} cm^{-3} is expected.

In Fig. 7.4(a) we plot Eq. 7.2 and in Fig. 7.4(b) we plot the real part of the refrac-

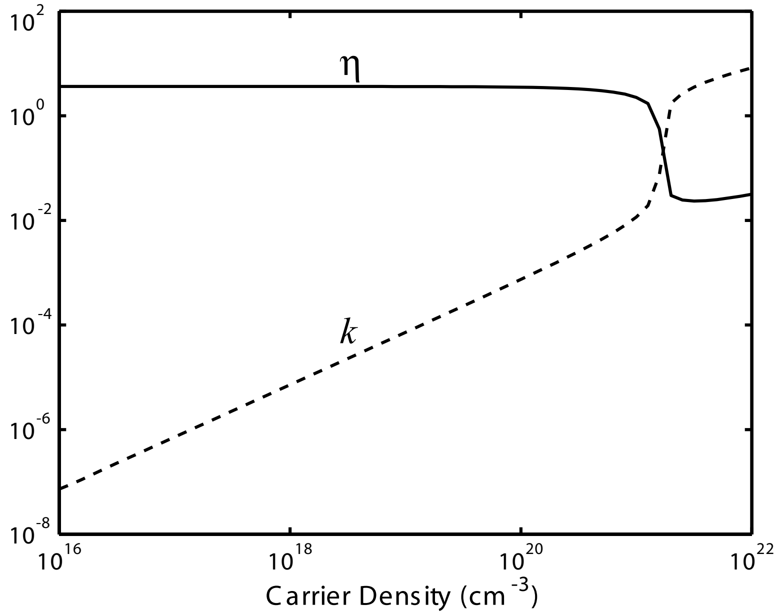

(a)

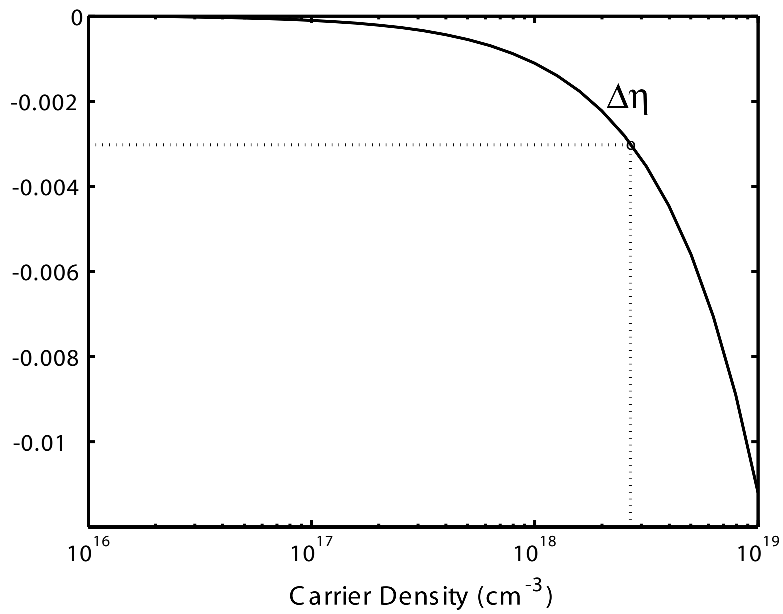

(b)

Figure 7.4: (a) Real (solid) and imaginary (dotted) parts of the refractive index and (b) real part of the refractive index change versus carrier density for the microring GaAs waveguide at the probe wavelength.

tive index change versus the injected free carrier density at a probe beam wavelength of 1543.4 nm. For a carrier density of $2.5 \times 10^{18}\text{cm}^{-3}$, a refractive index change of 3×10^{-3} is estimated which is consistent with the value obtained from the experiment. Fig. 7.4(a) shows that the change in the imaginary part of the refractive index at that value of carrier density is in the order of 10^{-5}. Thus, the additional loss due to the free carriers can be neglected and the assumption of a constant round trip loss inside the resonator is valid.

7.2 Phase Switching

So far we have only discussed the use of the transmission-transfer function of the microring resonator for switching. However, an examination of its phase-transfer function reveals a similar nonlinear enhancement, as we discussed earlier in Sec. 1.3. This phase enhancement can be observed by introducing the microring resonator into one arm of a Mach-Zehnder interferometer (MZI). Although, a MZI requires a π phase shift for switching, Fig. 1.4 showed that such amount of phase shift is drastically reduced by introducing the resonator on one arm of the MZI. It is worth mentioning here that the propagation loss of the microring has to be minimum for high interference visibility between the two arms of the MZI and hence efficient switching.

Fig. 7.5(a) shows a SEM picture of a MZI loaded with a microring resonator. The spectral response of the device is shown in Fig. 7.5(b). The asymmetry of the transmission around the resonance is due to the unintentional phase imbalance between the two

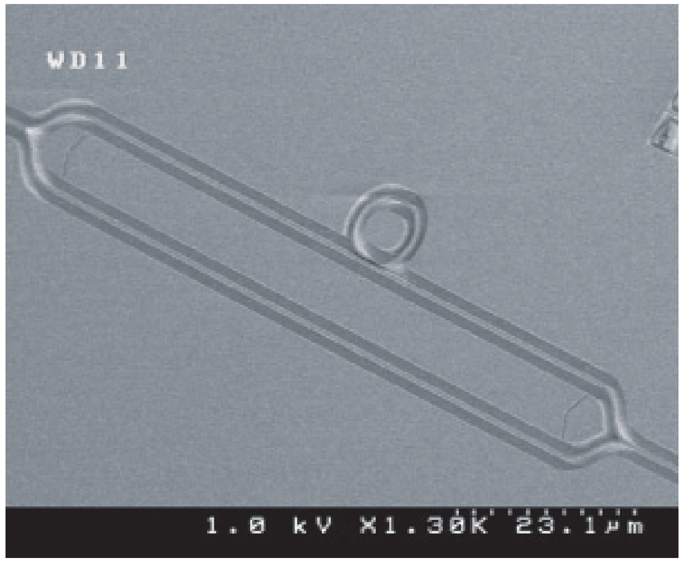

(a)

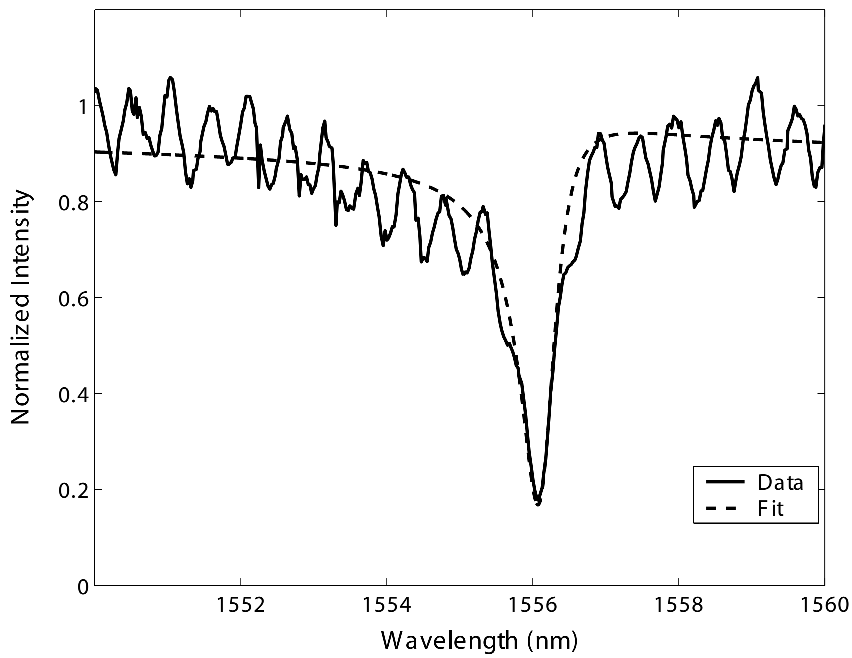

(b)

Figure 7.5: (a) A Scanning Electron Microscope picture of the MZI loaded with a microring resonator device and (b) measured (solid line) and fitted (dashed line) spectral response of the device around its resonance wavelength at 1556 nm.

arms of the MZI. The phase error is due to the electron beam lithography since each arm of the MZI is written separately. From the spectrum of the device, the resonator has an intrinsic quality factor of 2060 and an estimated finesse of 18.

We used the same experimental setup mentioned earlier to pump the device from the top. In Fig. 7.6, we plot the off-on switching behavior of the device, when the probe beam was initially tuned to the microring resonance at 1556 nm. A switching window of 24 ps is obtained, allowing 40 GHz data processing. An effective energy of 4 pJ/pulse is used to switch the device, which is approximately one order of magnitude lower than the energy required to switch the transmission-function of the microring resonator [73].

7.3 Carrier Lifetime

The speed of these devices is mainly limited by the carrier lifetime of the guiding material since the pump beam does not circulate inside the resonator. To measure the carrier lifetime independently, we optically pumped a tapered straight waveguide at different width sections. We ramped the pump beam energy so that enough carriers were injected into the waveguide and absorption was observed in a transmitted probe beam. By detecting the intensity variation of the probe beam, we could measure the recovery time of the transmitted signal and hence the carrier lifetime. In a tightly confined waveguide, diffusion to the waveguide walls dominates, where fast surface recombination occurs. In Fig. 7.7(a), we plot the normalized transmitted probe beam intensity when the waveguide was pumped at different cross sections. In Fig. 7.7(b), we plot the carrier lifetime

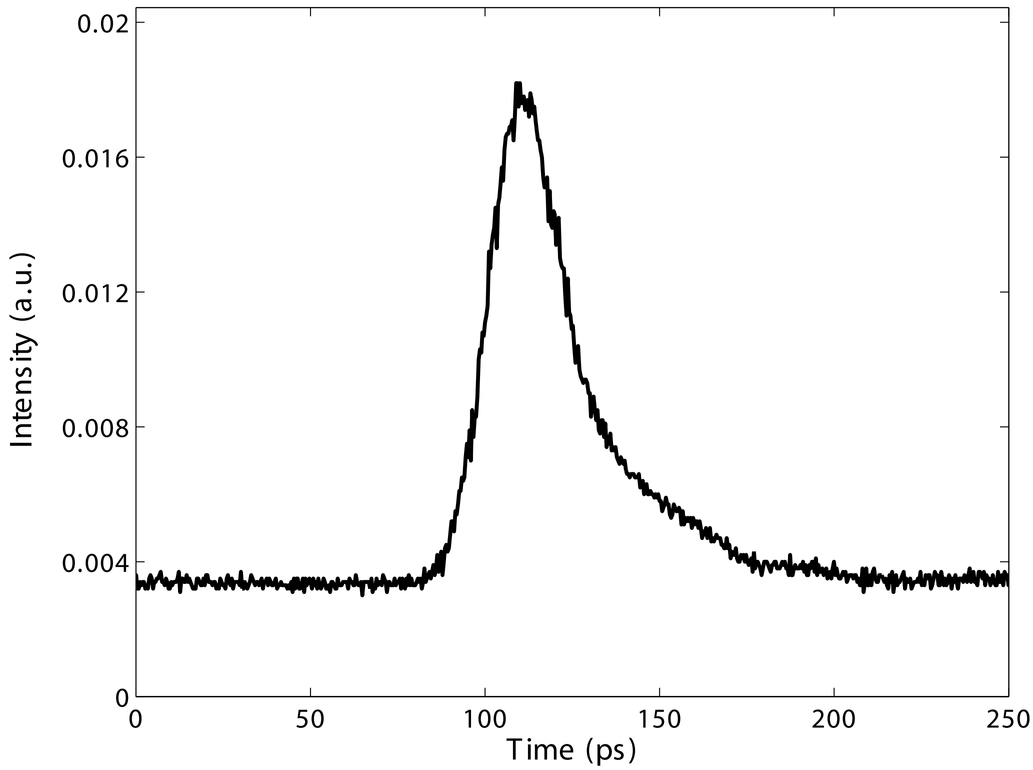

Figure 7.6: The Off-On switching behavior of the MZI loaded ring device when the probe beam is initially tuned to the microring resonance at 1556 nm.

versus its diffusion length which is approximately half the waveguide width. As can be seen, the carrier lifetime varies quadratically with the diffusion length as expected due to the diffusion processes. Since the guiding layer is made of intrinsic bulk material, ambipolar diffusion takes action where both electrons and holes contribute to the diffusion process. Using the Einstein relation, we fitted the carrier lifetime curve and extracted the ambipolar diffusion constant to be 19.2 cm^2/s. The ambipolar diffusion constant calculated from published values of electrons and holes mobilities and diffusion constants of

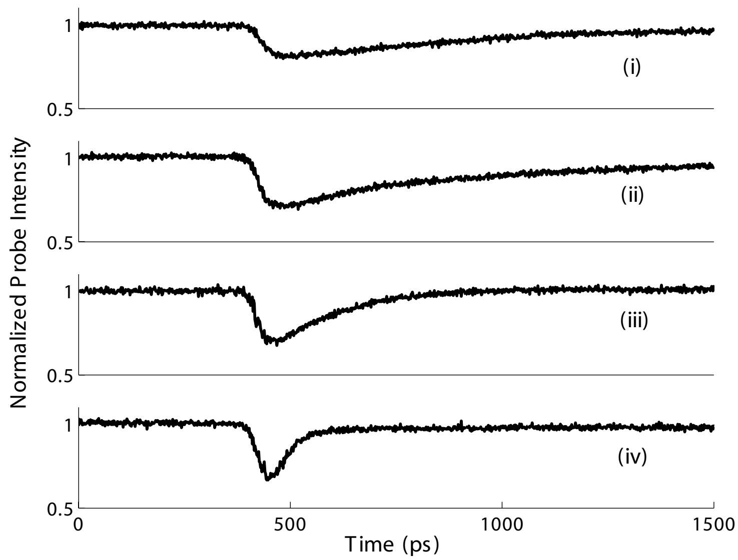

(a)

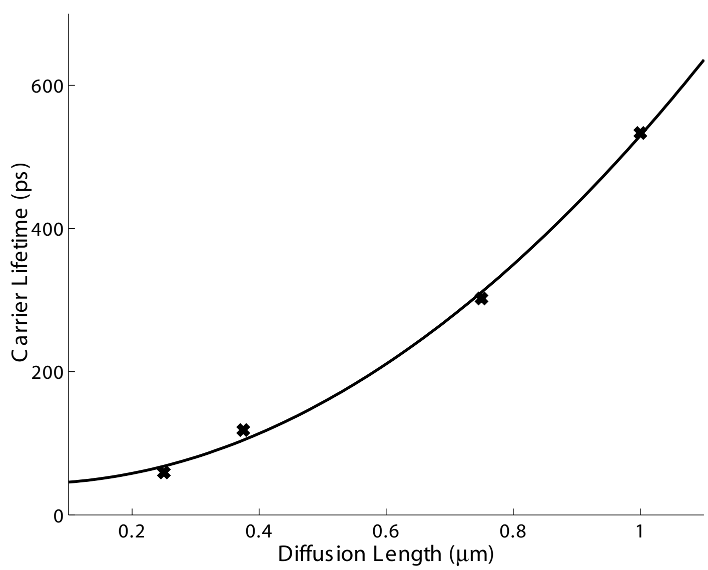

(b)

Figure 7.7: (a) Normalized transmitted probe intensity when the tapered straight waveguide was optically pumped at its width of (i) 2.0 μm, (ii) 1.5 μm, (iii) 0.8 μm, and (iv) 0.5 μm. (b) Measured and quadratic fit of the carrier lifetime of the GaAs waveguide versus the carrier diffusion length.

GaAs [61] is found to be 19.4 cm^2/s, which is very close to the measured value. Faster response time can be obtained by DC biasing the microresonator waveguide, where a static electric field normal to the epitaxial layer is induced and rapidly sweeps the free carriers out of the waveguide core [62].

7.4 Conclusion

In this chapter, we have demonstrated all-optical switching by free carrier injection induced by SPA in laterally coupled GaAs-AlGaAs microring resonators. Simulation results have been shown to be in good agreement with measured data. We investigated both the transmission and phase functions of the resonator using two different device configurations. These devices have great potential for switching, routing, multiplexing and demultiplexing, and reshaping. Optical pumping can be accomplished by integrated VCSELs underneath the microrings or by an array of laser diodes mounted on top of the microrings. The switching speed is limited by the carrier lifetime and can be enhanced by DC biasing the microring waveguide to sweep out carriers.

CHAPTER 8

CONCLUSIONS

In the preceding chapters of this dissertation, our studies of the nonlinear response and applications of semiconductor microring resonators were presented. In this work, we found that the carrier lifetime is the current limitation for the device speed. The best switching window obtained is 20 ps for the laterally coupled GaAs microring resonator when pumped from top. The InP devices have a switching window of 100 ps due to their low electron and hole mobilities compared to the GaAs mobilities. For pumping through the device, the ultimate switching limit is the cavity charging time or the photon lifetime. Switching energy varies around 20 pJ in most cases. Although the instantaneous Kerr effect is the nonlinear process we looked for, Two-Photon Absorption is the dominant nonlinear process involved in these devices when operating at the 1550 nm wavelength. The free carriers generated by TPA changes the refractive index of the microring waveguide and have been used to demonstrate switching, routing, demultiplexing and photonic logic gates. Furthermore, injection of free carrier by Single-Photon Absorption (SPA) was demonstrated and shown to be advantageous in some applications.

The performance of these devices can be enhanced by a better choice of the guiding material with higher nonlinearity and shorter carrier lifetime. Employing an active section inside the resonator is a promising solution to enhance the nonlinearity of the resonator and control its round trip loss and hence its bandwidth and resonance extinction. The gain provided by the active section can allow better switching contrast as well as higher signal to noise ratio at the output of the device. Once such gain is feasible, more microrings can be involved and cascaded to realize more complex functions and devices. Coupling losses are also to be considered. Moreover, the fabrication of local micro heaters imbedded with the resonator will give another degree of freedom in terms of thermal stability and tenability.

In conclusion, nonlinear optical microring resonators are good candidates for all-optical signal processing and computing. We showed that, while they are simple to process and design, they have shown great potential in optical switching, pulse reshaping, time division demultiplexing, spatial pulse routing, and photonic logic gates. On a planar integrated photonic circuit, passive and active microring resonators are soon to be the basic building blocks for the linear and nonlinear components.

Bibliography

[1] R. W. Eason and A. Miller, *Nonlinear optics in signal processing*. London, U.K.: Champan & Hall, 1993.

[2] M. N. Islam, *Fiber switching devices and systems*. New York, NY: Cambridge University Press, 1992.

[3] K. Honda, E. M. Garmire, and K. E. Wilson, "Characteristics of an integrated optics ring resonator fabricated in glass," *Journal of Lightwave Technology*, vol. 2, pp. 714–719, October 1984.

[4] B. E. Little, S. T. Chu, W. Pan, D. Ripin, T. Kaneko, Y. Kokubun, and E. P. Ippen, "Vertically coupled glass microring resonator channel dropping filters," *IEEE Photonics Technology Letters*, vol. 11, pp. 215–217, February 1999.

[5] B. E. Little, J. S. Foresi, G. Steinmeyer, E. R. Thoen, S. T. Chu, H. A. Haus, E. P. Ippen, L. C. Kimerling, and W. Greene, "Ultra-compact $\mathrm{Si}-\mathrm{SiO_2}$ microring resonator optical channel dropping filters," *IEEE Photonics Technology Letters*, vol. 10, pp. 549–551, April 1998.

[6] D. Y. Chu, M. K. Chin, N. J. Sauer, Z. Xu, T. Y. Chang, and S. T. Ho, "1.5 μmInGaAs/InAlGaAs quantum-well microdisk lasers," *IEEE Photonics Technology Letter*, vol. 5, pp. 1353–1355, December 1993.

[7] D. Rafizadeh, J. P. Zhang, S. C. Hagness, A. Taflove, K. A. Stair, S. T. Ho, and R. C. Tiberio, "Waveguide-coupled AlGaAs/GaAs microcavity ring and disk resonators with high finesse and 21.6 nm free spectral range," *Optics Letters*, vol. 22, pp. 1244–1246, August 1997.

[8] M. K. Chin, C. Youtsey, W. Zhao, T. Pierson, Z. Ren, S. L. Wu, L. Wang, Y. G. Zhao, and S. T. Ho, "GaAs microcavity channel-dropping filter based on a race-track resonator," *IEEE Photonics Technology Letters*, vol. 11, pp. 1620–1622, December 1999.

[9] P. P. Absil, J. V. Hryniewicz, B. E. Little, R. A. Wilson, L. G. Joneckis, and P.-T. Ho, "Compact microring notch filters," *IEEE Photonics Technology Letters*, vol. 12, pp. 398–400, April 2000.

[10] Y. Ma, G. Chang, S. Park, L. Wang, and S. T. Ho, "InGaAsP thin-film microdisk resonators fabricated by polymer wafer bonding for wavelength add-drop filters," *IEEE Photonics Technology Letters*, vol. 12, pp. 1495–1497, November 2000.

[11] R. Grover, P. P. Absil, V. Van, J. V. Hryniewicz, B. E. Little, O. S. King, L. C. Calhoun, F. G. Johnson, and P.-T. Ho, "Vertically coupled GaInAsP – InP microring resonators," *Optics Letters*, vol. 26, pp. 506–508, April 2001.

[12] K. Djordjev, S.-J. Choi, S.-J. Choi, and P. D. Dapkus, “High-Q vertically coupled InP microdisk resonators,” *IEEE Photonics Technology Letter*, vol. 14, pp. 331–333, March 2002.

[13] R. Grover, T. A. Ibrahim, T. N. Ding, Y. Leng, L.-C. Kuo, S. Kanakaraju, K. Amarnath, L. C. Calhoun, and P.-T. Ho, “Laterally coupled InP-based single-mode microracetrack notch filter,” *Photonics Technology Letters*, vol. 15, pp. 1082–1084, August 2003.

[14] F. C. Blom, H. Kelderman, H. J. W. M. Hoekstra, A. Driessen, T. J. A. Popma, S. T. Chu, and B. E. Little, “A single channel dropping filter based on a cylindrical microresonator,” *Optics Communications*, vol. 167, pp. 77–82, August 1999.

[15] P. Rabiei and W. H. Steier, “Micro-ring resonators using polymer materials,” in *Conference on Lasers and Electro Optics (CLEO 2001)*, Baltimore, MD, 2001.

[16] W. Y. Chen, R. Grover, T. A. Ibrahim, V. Van, and P.-T. Ho, “Compact single-mode benzocyclobutene microracetrack resonators,” in *Integrated Photonics Research (IPR)*, Washington, DC, 2003.

[17] B. E. Little, S. T. Chu, H. A. Haus, J. Foresi, and J. P. Laine, “Microring resonator channel dropping filters,” *Journal of Lightwave Technology*, vol. 15, pp. 998–1005, June 1997.

[18] J. E. Heebner and R. W. Boyd, “Enhanced all-optical switching by use of a nonlinear fiber ring resonator,” *Optics Letters*, vol. 24, pp. 847–849, June 1999.

[19] B. E. Little and S. T. Chu, "Toward very large-scale integrated photonics," *Optics & Photonics News*, vol. 11, pp. 24–29, November 2000.

[20] J. Singh, *Optoelectronics: An introduction to materials and devices*. New York, NY: McGraw-Hill, Inc., 1996.

[21] S. Adachi, Ed., *Properties of Aluminum Gallium Arsenide*, ser. EMIS Datareviews Series. London, UK: IEE, Inspec, 1993.

[22] S. Adaashi, Ed., *Properties of Indium Phosphide*, ser. EMIS Datareviews Series. London, UK: IEE, Inspec, 1991.

[23] D. Rafizadeh, J. P. Zhang, S. C. Hagness, A. Taflove, K. A. Stair, S. T. Ho, and R. C. Tiberio, "Temperature tuning of microcavity ring and disk resonators at 1.5 μm," in *IEEE Lasers and Electro-Optics Society, 10th Annual Meeting (LEOS '97)*, San Francisco, CA, 1997.

[24] P. Mandel, S. Smith, and B. Wherrett, *From Optical Bistability Towards Optical Computing*. North-Holland, 1987.

[25] H. M. Gibbs, *Controlling Light with Light*. Academic Press Inc., 1985.

[26] T. A. Ibrahim, K. Ritter, V. Van, P. P. Absil, R. Grover, P.-T. Ho, and J. Goldhar, "Experimental observation of optical bistability in semiconductor microring resonators," in *Integrated Photonics Research (IPR)*, Monteray, CA, 2001.

[27] R. W. Boyd, *Nonlinear optics*. San Diego, CA: Academic Press, 1992.

[28] J. H. Bechtel and W. L. Smith, "Two-photon absorption in semiconductors with picosecond laser pulses," *Physics Review B*, vol. 13, pp. 3515–3522, April 1976.

[29] E. W. Van Stryland, M. A. Woodall, H. Vanherzeele, and M. J. Soileau, "Energy bandgap-dependence of two-photon absorption," *Optics Letters*, vol. 10, pp. 490–492, October 1985.

[30] A. Villeneuve, M. Sundheimer, N. Finlayson, G. I. Stegeman, S. Morasca, C. Rigo, R. Calvani, and C. De Bernardi, "Two-photon absorption in $In_{1-x-y}Ga_xAl_yAs/InP$ waveguides at communication wavelengths," *Applied Physics Letters*, vol. 56, pp. 1865–1867, May 1990.

[31] H. K. Tsang, R. V. Penty, I. H. White, R. S. Grant, W. Sibbett, J. B. D. Soole, H. P. LeBlanc, N. C. Andreadakis, R. Bhat, and M. A. Koza, "Two-photon absorption and self-phase modulation in ingaasp/inp multi-quantum-well waveguides," *Journal of Applied Physics*, vol. 70, pp. 3992–3994, October 1991.

[32] H. K. Tsang, R. V. Penty, I. H. White, R. S. Grant, W. Sibbett, J. B. D. Soole, H. P. LeBlanc, N. C. Andreadakis, E. Colas, and M. S. Kim, "Polarization and field dependent two-photon absorption in gaas/algaas multiquantum well waveguides in the half-band gap spectral region," *Applied Physics Letters*, vol. 59, pp. 3440–3442, December 1991.

[33] H. K. Tsang, L. Y. Chan, J. B. D. Soole, H. P. LeBlanc, M. A. Koza, and R. Bhat, "High sensitivity autocorrelation using two-photon absorption in ingaasp waveg-

uides," *Electronics Letters*, vol. 31, pp. 1173–1175, September 1995.

[34] Z. Zheng, A. M. Weiner, J. H. Marsh, and M. M. Karkhanehchi, "Ultrafast optical thresholding based on two-photon absorption gaas waveguide photodetectors," *IEEE Photonics Technology Letters*, vol. 9, pp. 493–495, April 1997.

[35] V. Van, T. A. Ibrahim, K. Ritter, P. P. Absil, F. G. Johnson, R. Grover, J. Goldhar, and P.-T. Ho, "All-optical nonlinear switching in GaAs – AlGaAs microring resonators," *IEEE Photonics Technology Letters*, vol. 14, pp. 74–76, January 2002.

[36] R. J. Deri and E. Kapon, "Low-loss iii-v semiconductor optical waveguides," *IEEE Journal of Quantum Electronics*, vol. 27, pp. 626–640, March 1991.

[37] T. Bischofberger and Y. R. Shen, "Theoretical and experimental study of the dynamic behavior of a nonlinear fabry-perot interferometer," *Physics Review A*, vol. 19, pp. 1169–1176, March 1979.

[38] K. Ikeda, "Multiple-valued stationary state and its instability of the transmitted light by a ring cavity system," *Optics Communications*, vol. 30, pp. 257–261, August 1979.

[39] K. Ogusu, H. Shigekuni, and Y. Yokota, "Dynamic transmission properties of a nonlinear fiber ring resonator," *Optics Letters*, vol. 20, pp. 2288–2290, November 1995.

[40] K. Ogusu, “Dynamic behavior of reflection optical bistability in a nonlinear fiber ring resonator,” *IEEE Journal of Quantum Electronics*, vol. 32, pp. 1537–1543, September 1996.

[41] B. E. Little, “Filter synthesis for coupled waveguides,” *Journal of Lightwave Technology*, vol. 15, pp. 1149–1155, July 1997.

[42] B. E. Little, S. T. Chu, J. V. Hryniewicz, and P. P. Absil, “Filter synthesis for periodically coupled microring resonators,” *Optics Letters*, vol. 25, pp. 344–346, March 2000.

[43] S. T. Chu, B. E. Little, P. Wugen, T. Kaneko, and Y. Kokubun, “Cascaded microring resonators for crosstalk reduction and spectrum cleanup in add-drop filters,” *IEEE Photonics Technology Letters*, vol. 11, pp. 1423–1425, November 1999.

[44] S. T. Chu, B. E. Little, W. Pan, T. Kaneko, and Y. Kokubun, “Second order filter response from parallel coupled glass microring resonators,” *IEEE Photonics Technology Letters*, vol. 11, pp. 1426–1428, November 1999.

[45] J. V. Hryniewicz, P. P. Absil, B. E. Little, and P.-T. Ho, “Higher order filter response in coupled microring resonators,” *IEEE Photonics Technology Letters*, vol. 12, pp. 320–322, March 2000.

[46] B. Little, “A VLSI photonics platform,” in *Optical Fiber Communication Conference*, Atlanta, GA, 2003.

[47] B. E. Little, S. T. Chu, and H. A. Haus, “Second-order filtering and sensing with partially coupled traveling waves in a single resonator,” *Optics Letters*, vol. 23, pp. 1570–1572, October 1998.

[48] P. P. Absil, J. V. Hryniewicz, B. E. Little, F. G. Johnson, and P.-T. Ho, “Vertically coupled microring resonators using polymer wafer bonding,” *IEEE Photonics Technology Letters*, vol. 13, pp. 49–51, January 2001.

[49] P. P. Absil, “Microring resonators for wavelength division multiplexing and integrated photonics applications,” Ph. D. thesis, University of Maryland, College Park, 2000.

[50] S. Ramo, J. R. Whinnery, and T. Van Duzer, *Fields and Waves in Coomunication Electronics*, 3rd ed. New York: John Wiley & Sons, Inc., 1994.

[51] A. Villeneuve, K. Al-Hemyari, J. U. Kang, C. N. Ironside, J. S. Aitchison, and G. I. Stegeman, “Demonstration of all-optical demultiplexing at 1550 nm with an AlGaAs directional coupler,” *Electronics Letters*, vol. 29, pp. 721–722, April 1993.

[52] C. Coriasso, D. Campi, C. Carcciatore, L. Faustini, L. Rigo, and A. Stano, “All-optical switching and pulse routing in a distributed-feedback waveguide device,” *Optics Letters*, vol. 23, pp. 183–185, February 1998.

[53] T. A. Ibrahim, V. Van, and P.-T. Ho, “All-optical time division demultiplexing and spatial pulse routing using a GaAsAlGaAs microring resonator,” *Optics Letters*, vol. 27, pp. 803–805, May 2002.

[54] G. I. Stegeman and C. T. Seaton, “Nonlinear integrated optics,” *Journal of Applied Physics*, vol. 58, pp. R57–R78, December 1985.

[55] S. D. Smith, “Optical bistability, photonic logic, and optical computation,” *Applied Optics*, vol. 25, pp. 1550–1564, May 1986.

[56] V. Van, T. A. Ibrahim, P. P. Absil, F. G. Johnson, R. Grover, and P.-T. Ho, “Optical signal processing using nonlinear semiconductor microring resonators,” *IEEE Journal of Selected Topics in Quantum Electronics*, vol. 8, pp. 705–713, May/June 2002.

[57] P. P. Absil, J. V. Hryniewicz, B. E. Little, P. S. Cho, R. A. Wilson, L. G. Joneckis, and P.-T. Ho, “Wavelength conversion in gaas micro-ring resonators,” *Optics Letters*, vol. 25, pp. 554–556, April 2000.

[58] T. A. Ibrahim, R. Grover, L.-C. Kuo, S. Kanakaraju, L. C. Calhoun, and P.-T. Ho, “All-optical and/nand logic gates using semiconductor microresonators,” *Photonics Technology Letters*, vol. 15, pp. 1422–1424, October 2003.

[59] ——, “All-optical switching using a critically coupled InP micro-racetrack resonator,” in *Integrated Photonics Research (IPR)*, Washington, DC, 2003.

[60] E. S. Awad, P. Cho, and J. Goldhar, “High-speed all-optical and gate using nonlinear transmission of electroabsorption modulator,” *Photonics Technology Letters*, vol. 13, pp. 472–474, May 2001.

[61] S. M. Sze, *Physics of semiconductor devices*, 2nd ed. John Wiley & Sons, Inc., 1981.

[62] M. B. Yairi and D. A. B. Miller, "Equivalence of diffusive conduction and giant ambipolar diffusion," *Journal of Applied Physics*, vol. 91, pp. 4374–4381, April 2002.

[63] M. Guezo, S. Loualiche, J. Even, A. Le Corre, H. Folliot, C. Labbe, O. Dehaese, and G. Dousselin, "Ultrashort, nonlinear, optical time response of Fe-doped InGaAs/InP multiple quantum wells in 1.55-μm range," *Applied Physics Letters*, vol. 82, no. 9, pp. 1670–1672, March 2003.

[64] M. Sheik-Bahae and E. Stryland, *Optical nonlinearities in the transparency region of bulk semiconductors*, ser. Nonlinear Optics in Semiconductors I, Semiconductors and Semimetals. San Diego, CA: Academic Press, 1999, vol. 58.

[65] B. R. Bennett, R. A. Soref, and J. A. del Alamo, "Carrier-induced change in refractive index of InP, GaAs, and InGaAsP," *IEEE Journal of Quantum Electronics*, vol. 26, pp. 113–122, January 1990.

[66] T. A. Ibrahim, W. Cao, Y. Kim, J. Li, J. Goldhar, P.-T. Ho, and C. H. Lee, "All-optical switching in a laterally coupled microring resonator by carrier injection," *IEEE Photonics Technology Letters*, vol. 15, no. 1, pp. 36–38, January 2003.

[67] H. M. Gibbs, S. L. McCall, A. C. Venkatesan, T. N. C.and Gossard, A. Passner, and W. Wiegmann, "Optical bistability in semiconductors," *Applied Physics Letters*, vol. 35, no. 6, pp. 451–453, September 1979.

[68] D. A. B. Miller, S. D. Smith, and A. Johnson, "Optical bistability and signal amplification in semiconductor crystals: applications of new low-power nonlinear effects in insb," *Applied Physics Letters*, vol. 35, no. 9, p. 658, November 1979.

[69] C. H. Lee, *Picosecond Optoelectronic Devices*. London, U.K.: Academic Press, 1984.

[70] C. H. Lee, P. S. Mak, and A. P. DeFonzo, "Optical control of millimeter-wave propagation in dielectric waveguides," *IEEE Journal of Quantum Electronics*, vol. 16, pp. 277–288, March 1980.

[71] A. M. Yurek, C. D. Striffler, and C. H. Lee, *Optoelectronic devices for millimeter waves*. London, U.K.: Academic Press, 1985, vol. 14, ch. 4, pp. 249–290.

[72] K. Djordjev, S.-J. Choi, S.-J. Choi, and P. D. Dapkus, "Microdisk tunable resonant filters and switches," *IEEE Photonics Technology Letter*, vol. 14, pp. 828–830, June 2002.

[73] T. A. Ibrahim, W. Cao, Y. Kim, J. Goldhar, P.-T. Ho, and C. H. Lee, "All-optical switching in microring devices by carrier injection," in *Optical Fiber Communication Conference and Exhibit (OFC)*, Atlanta, GA, 2003.